TKK Dissertations 199
Espoo 2009

SONICATION METHODS AND MOTION COMPENSATION FOR MAGNETIC RESONANCE GUIDED HIGH-INTENSITY FOCUSED ULTRASOUND

Doctoral Dissertation

Max Köhler

Helsinki University of Technology
Faculty of Information and Natural Sciences
Department of Biomedical Engineering and Computational Science

TKK Dissertations 199
Espoo 2009

SONICATION METHODS AND MOTION COMPENSATION FOR MAGNETIC RESONANCE GUIDED HIGH-INTENSITY FOCUSED ULTRASOUND

Doctoral Dissertation

Max Köhler

Dissertation for the degree of Doctor of Science in Technology to be presented with due permission of the Faculty of Information and Natural Sciences for public examination and debate in Auditorium F239a at Helsinki University of Technology (Espoo, Finland) on the 4th of December, 2009, at 12 noon.

Helsinki University of Technology
Faculty of Information and Natural Sciences
Department of Biomedical Engineering and Computational Science

Teknillinen korkeakoulu
Informaatio- ja luonnontieteiden tiedekunta
Lääketieteellisen tekniikan ja laskennallisen tieteen laitos

Distribution:
Helsinki University of Technology
Faculty of Information and Natural Sciences
Department of Biomedical Engineering and Computational Science
P.O. Box 2200 (Rakentajanaukio 2)
FI - 02015 TKK
FINLAND
URL: http://www.becs.tkk.fi/
Tel. +358-9-470 23172
Fax +358-9-470 23182
E-mail: max.kohler@philips.com

ISBN 978-952-248-198-6
ISBN 978-952-248-199-3 (PDF)
ISSN 1795-2239
ISSN 1795-4584 (PDF)
URL: http://lib.tkk.fi/Diss/2009/isbn9789522481993/

TKK-DISS-2680

Yliopistopaino
Helsinki 2009

ABSTRACT OF DOCTORAL DISSERTATION	HELSINKI UNIVERSITY OF TECHNOLOGY P.O. BOX 1000, FI-02015 TKK http://www.tkk.fi

Author Max Köhler

Name of the dissertation
Sonication methods and motion compensation for magnetic resonance guided high-intensity focused ultrasound

Manuscript submitted 9.6.2009	Manuscript revised 30.10.2009
Date of the defence 4.12.2009	
☐ Monograph	☒ Article dissertation (summary + original articles)

Faculty	Faculty of Information and Natural Sciences
Department	Department of Biomedical Engineering and Computational Science
Field of research	Biomedical Engineering
Opponent(s)	Professor Kullervo Hynynen, University of Toronto
Supervisor	Professor Pekka Meriläinen
Instructor	Gösta Ehnholm, D.Sc. (Tech.)

Abstract

High-intensity focused ultrasound (HIFU) is an efficient noninvasive therapeutic technique for localized heating of tissues deep within the human body through intact skin. Magnetic resonance imaging (MRI) can provide excellent soft-tissue contrast and can be used for both treatment planning and post-treatment assessment of the induced tissue damage. MRI can also provide temperature sensitive *in vivo* images via proton resonance frequency shift thermometry. Combined, the use of MRI and HIFU (MR-HIFU) ablation make for a promising therapeutic modality for controlled and noninvasive selective tissue destruction. Sonication strategies, MR thermometry methods, feedback control, and motion compensation for MR-HIFU were developed and evaluated in this thesis.

The primary aim of the thesis was to develop a safe and efficient strategy for clinical MR-HIFU ablation. An efficient volumetric method of ablation was achieved by utilizing the phased-array capabilities of the transducer and the inherent heat diffusion of already deposited heat. The induced temperature rise was monitored with rapid multiplane MR thermometry with a volumetric coverage of the heated region. Acquisition and display of temperature images during sonication improved the safety of the therapy. The therapeutic procedure was evaluated in a large animal model and proved to provide a substantial improvement in efficiency as compared to existing methods without compromising safety.

The second aim was to improve the reliability of the proposed volumetric sonication strategy. This was achieved with a simple and robust binary feedback algorithm that adjusted the sonication duration of each part of the sonication trajectory based on the temperature rise as obtained by volumetric MR thermometry. The feedback algorithm was evaluated in a large animal model, and was found to reduce the variability in thermal lesion size by approximately 70%.

The third aim was to develop a through-plane motion correction method for real-time MR thermometry without disturbing thermometry. This was achieved with a fat-selective navigator. This navigator outperformed the conventional navigator for direct tracking of the kidney under free breathing. The navigator also provided accurate indexing of the look-up-table used to correct the reference phase for MR thermometry of mobile organs. Finally, the combination of through-plane motion correction provided by the fat-selective navigator with existing methods of in-plane motion correction and reference phase correction, allowed for an accurate 3D motion compensation of both MR thermometry and MR-HIFU sonication.

Keywords HIFU, MR thermometry, MR-HIFU, sonication, ablation, feedback control, motion compensation

ISBN (printed)	978-952-248-198-6	ISSN (printed)	1795-2239
ISBN (pdf)	978-952-248-199-3	ISSN (pdf)	1795-4584
Language	English	Number of pages	118 p. + app. 70 p.
Publisher	Department of Biomedical Engineering and Computational Science, Helsinki University of Technology		
Print distribution	Department of Biomedical Engineering and Computational Science		

☒ The dissertation can be read at http://lib.tkk.fi/Diss/2009/isbn9789522481993/

SAMMANFATTNING (ABSTRAKT) AV DOKTORSAVHANDLING	TEKNISKA HÖGSKOLAN PB 1000, FI-02015 TKK http://www.tkk.fi

Författare Max Köhler

Titel
Sonikerings metoder och rörelsekompensering för magnetresonanstomografi styrd högintensivt fokuserat ultraljud

Inlämningsdatum för manuskript 9.6.2009	Datum för det korrigerade manuskriptet 30.10.2009

Datum för disputation 4.12.2009

☐ Monografi ☒ Sammanläggningsavhandling (sammandrag + separata publikationer)

Fakultet	Fakulteten för informations- och naturvetenskaper
Institution	Institutionen för medicinsk teknik och beräkningsvetenskap
Forskningsområde	Medicinsk teknik
Opponent(er)	Professor Kullervo Hynynen, University of Toronto
Övervakare	Professor Pekka Meriläinen
Handledare	Gösta Ehnholm, D.Sc. (Tech.)

Sammanfattning (Abstrakt)

Högintensivt fokuserat ultraljud (HIFU) är en effektiv ickeinvasiv teknik för terapeutisk lokal uppvärmning och behandling av djupt liggande vävnad utan behov av kirurgiska ingrepp. Magnetresonanstomografi (MRT) kan ge bilder av utmärkt kontrast i mjukvävnad och kan användas både för att göra en vårdplan och för att analysera de framkallade vävnadsskadorna efter behandling. MRT kan också noggrant visa temperaturskillnader *in vivo* via protonernas temperaturberoende resonansfrekvens. Genom att kombinera MRT och HIFU (MR-HIFU) ablation, erhålls en lovande terapeutisk metod för välkontrollerad icke-invasiv selektiv nedbrytning av vävnad. Metoder för sonikering, MR termometri, återkopplad reglering och rörelsekompensation för MR-HIFU har utvecklats och evaluerats i avhandlingen.

Huvudändamålet för avhandlingen var att utveckla en säker och effektiv strategi för klinisk MR-HIFU ablation. En effektiv volymetrisk ablationsmetod erhölls genom att elektroniskt styra fokuspunkten och utnyttja den naturliga värmediffusionen från tidigare uppbyggd värme. Temperaturökningen mättes med snabb multi-plan MR termometri, som täckte hela det uppvärmda området. Möjligheten att följa med temperaturutvecklingen samtidigt med sonikeringen förbättrade terapins säkerhet. Den terapeutiska proceduren evaluerades *in vivo* i grisar och resultaten påvisade en betydligt effektivare behandling jämfört med nuvarande metoder utan att ge avkall på säkerheten.

Det andra målet var att förbättra den föreslagna volymetriska sonikeringsmetodens pålitlighet. Detta uppnåddes genom en enkel och robust binär återkoppling algoritm som reglerade sonikeringstiden för envar del av sonikeringsbanan på basen av temperaturökningen, som mättes med volymetrisk MR termometri. Återkopplingsalgoritmen evaluerades *in vivo* i grisar och påvisades att minska variationen i den ablerade vävnadsvolymen med cirka 70% för enskilda sonikeringar.

Avhandlingens tredje mål var att utveckla en kompensationsmetod för rörelse genom avbildningsplanet för realtids MR termometri utan att störa temperaturmätningen. Detta åstadkoms med en fett-selektiv navigator, som också visade sig vara bättre än den konventionella navigatorn för direkt följande av en njures rörelse under fri andning. Navigatorn kunde också användas för noggrann indexering av uppslagstabeller för korrigering av referensfas för MR termometri av mobila organ. Genom att kombinera den fett-selektiva navigatorn med existerande metoder för rörelsekompensation i avbildnings-planet och referensfaskorrektion, kunde en 3D rörelsekompensation för både MR termometri och för MR-HIFU uppnås.

Ämnesord (Nyckelord) HIFU, MR termometri, MR-HIFU, ablation, återkopplad reglering, rörelsekompensation

ISBN (tryckt)	978-952-248-198-6	ISSN (tryckt)	1795-2239
ISBN (pdf)	978-952-248-199-3	ISSN (pdf)	1795-4584
Språk	engelska	Sidantal	118 s. + app. 70 s.
Utgivare	Institutionen för medicinsk teknik och beräkningsvetenskap, Tekniska högskolan		
Distribution av tryckt avhandling	Institutionen för medicinsk teknik och beräkningsvetenskap		

☒ Avhandlingen är tillgänglig på nätet http://lib.tkk.fi/Diss/2009/isbn9789522481993/

Preface

The work presented in this thesis has been performed at Philips Medical Systems MR Finland during the years 2005 – 2009 in close collaboration with the Imagerie Moléculaire et Fonctionnelle (IMF) laboratory at the University of Bordeaux 2, France. I am very grateful towards Philips for the opportunity to participate in the interesting research that brought this thesis about, and for the possibility to publish both the theory and results of this research.

It has been a great privilege to work with my instructor for this thesis, Dr. Gösta Ehnholm, whom I wish to thank for his guidance throughout the years as well as for his infectious enthusiasm and witty remarks. I would also like to express my gratitude to my supervisor, Prof. Pekka Meriläinen, for his support, suggestions, and aid in general academic matters. I furthermore wish to thank Prof. emeritus Toivo Katila for the encouragement and support that he provided during my studies. Pre-examiners Prof. Raimo Sepponen and Prof. Juha Töyräs are in turn appreciated for their careful review, constructive criticism and suggestions for improvements.

The research and experiments for this thesis were in large part carried out at the IMF laboratory in Bordeaux, and I am indebted to Prof. Chrit Moonen and the friendly IMF staff for taking me on as one of their own for more than half a year, albeit one that does not speak French. I also wish to thank Prof. Moonen for his advice, views, and the constructive friendly down-to-earth dialog that he always seemed to have time for. I would like to express my deepest gratitude to Dr. Mario Ries for his guidance on all matters of MR thermometry, but also for his distinct and enjoyable humor. I am very thankful to Dr. Bruno Quesson for his aid in preparing and performing the experiments that are the backbone of this thesis, as well as for his extensive advice on scientific writing. My colleague Dr. Charles Mougenot also deserves my deepest gratitude for his help in performing these experiments.

I would furthermore like to thank Panu Kauppila, Dr. Sham Sokka, and general manager Dr. Teppo Jyrkkiö for both allowing and encouraging the writing of this thesis.

I am also very grateful for the efforts of my co-authors Julia Enholm, Silke Hey, Dr. Baudouin Denis de Senneville, Dr. Greg Maclair, Dr. Matthieu Lepetit-Coiffé, Yasmina Berber, Prof. Brigitte Le Bail, and Dr. Christophe Laurent without whom the publications and this thesis could not have been written.

I wish to thank Dr. Teuvo Vaara, Jaakko Tölö, Dr. Erkki Vahala, Dr. Thomas Andreae, and Anne Niemi for their aid, advice, and contributions throughout the years. I also wish to thank my other colleagues at Philips that are too numerous to all be mentioned by name. Your camaraderie and expertise has made working with you all a truly rewarding experience.

My deepest gratitude also goes to my parents Tove and Peter Köhler for their never-ending support. My brothers Arne, Berndt, and Klaus are also very much appreciated for their support.

I also wish to thank my son Erik for the joy that he has brought me over the last couple of years and for the constant reminder that he provides of the more important things in life than physics. Most of all, I would like to thank my wife Anna for her patience, support, and love without which I would certainly not have endured this process.

Espoo, 1st of November, 2009

Contents

List of Publications

This thesis consists of an overview and of the following publications which are referred to in the text by their Roman numerals.

I M.O. Köhler, C. Mougenot, B. Quesson, J. Enholm, B. Le Bail, C. Laurent, C.T.W. Moonen, and G.J. Ehnholm. Volumetric HIFU ablation under 3D guidance of rapid MRI thermometry. Medical Physics 2009;36(8):3521–3535.

II J.K. Enholm, M.O. Köhler, B. Quesson, C. Mougenot, C.T.W. Moonen, and S.D. Sokka. Improved Volumetric MR-HIFU Ablation by Robust Binary Feedback Control. IEEE Transactions on Biomedical Engineering 2009, In press.

III M.O. Köhler, C.T.W. Moonen, and M. Ries. Spectral Selective Pencil-Beam Navigator for Abdominal Imaging. Helsinki University of Technology Publications in Engineering Physics, Report TKK-F-A860.

IV S. Hey, G. Maclair, B. Denis de Senneville, M. Lepetit-Coiffé, Y. Berber, M.O. Köhler, B. Quesson, C.T.W. Moonen, and M. Ries. Online correction of respiratory-induced field disturbances for continuous MR-thermometry in the breast. Magnetic Resonance in Medicine 2009;61(6):1494–1499.

V M. Köhler, G. Maclair, B. Denis de Senneville, C. Moonen, and M. Ries. 3D Navigated Real-Time Thermometry for Abdominal Imaging. In: Proceedings of the 16th Annual Meeting of ISMRM, Toronto, Canada, 2008 (abstract 1226).

Author's contribution

In Publication **I**, the concept of volumetric ablation and multiplane volumetric thermometry are presented. The improved efficiency and ablation performance of using the volumetric sonication method is established, and the feasibility and value of the volumetric thermometry in combination with volumetric ablation is discussed. The author designed both the ablation and thermometry methods, and optimized the related parameters. He participated in most of the animal experiments, taking responsibility for the use of the MR-HIFU system. The author also had primary responsibility for the production of the manuscript.

Publication **II** presents a robust nonparametric feedback algorithm designed for the volumetric MR-HIFU ablation strategy presented in Publication **I**. The author had a key role in the development of the concept of binary feedback control, for which a patent has been filed. He performed the extensive simulations on which the control is based, and to which the experimental results are compared in the paper. He participated in most of the animal experiments, taking responsibility for the use of the MR-HIFU system. The author contributed greatly to the manuscript, especially regarding the simulation and experimental data as well as their presentation.

Publication **III** presents a spectral selective pencil-beam navigator that can be used for direct tracking of organ motion without disturbing the water-proton magnetization used for thermometry. The author contributed extensively to development of the concept, implemented the software on the Philips MR scanner, and performed the simulations as well as participated in the experiments. The author also had primary responsibility for the production of the manuscript.

In Publications **IV**, a multi-baseline model-corrected thermometry technique is developed and tested in the breast of five volunteers without applying heat. The author implemented the pencil-beam navigators in the software of the Philips MR scanner.

These navigators are used to retrieve the appropriate baseline images from the look-up table in this publication.

In Publications **V**, the author combined 2D motion-compensation with the spectral selective pencil-beam navigator of Publication **III** for 3D motion compensated MR thermometry. The author had main responsibility for the abstract.

List of Abbreviations

2D	Two dimensional
3D	Three dimensional
CT	Computed tomography
EM	Equivalent minutes at 43 °C, unit of thermal dose
EPI	Echo planar imaging
FDA	Food and drug administration
FFE	Fast field echo
FOV	Field of view
FWHM	Full width at half maximum
HIFU	High-intensity focused ultrasound
HZ	Halo zone as indentified in gross pathology
IMF	Imagerie Moléculaire et Fonctionnelle
LQR	Linear quadratic regulator
MR	Magnetic resonance
MR-HIFU	Combination of HIFU therapy with MR guidance
MRI	Magnetic resonance imaging
N	Normal tissue as indentified in gross pathology
PID	Proportional-integral-derivative, a control algorithm
PRF	Proton resonance frequency
RF	Radio frequency
RZ	Red peripheral zone as indentified in gross pathology
SENSE	Sensitivity encoding
SNR	Signal-to-noise ratio
TSE	Turbo spin echo
TSENSE	Temporally adaptive sensitivity encoding
WZ	White central zone as indentified in gross pathology

List of Symbols

B_0	Main magnetic field
B_{loc}	Local magnetic field
I	Ultrasound intensity
N	Number of transducer elements
S	Transducer element surface area
T	Temperature
T_1	Longitudinal relaxation time
T_2	Transverse relaxation time
T_{ar}	Temperature of arterial blood
TD_{43}	Thermal dose in equivalent minutes at 43°C
TE	Echo time
TR	Repetition time
T_{ref}	Reference temperature
ΔB	Deviation from B_0 in the current image
ΔB_{ref}	Deviation from B_0 in the reference image
ΔT	Temperature change
ΔT_{app}	Apparent temperature change
ΔT_i	Temperature change until dynamic image i
ΔT_{real}	Real temperature change
c	Speed of sound
c_{b}	Specific heat capacity of blood
c_{t}	Specific heat capacity of tissue
$\text{d}S_j$	Infinitesimal part of the transducer element surface area
f	Ultrasound frequency
i	Imaginary unit
k	Combined wave-number and attenuation
k_{t}	Heat conductivity of tissue
l_j	Distance from transducer element j to the desired focus location

p	Ultrasound pressure
p_0	Initial ultrasound pressure at the surface of the transducer
$\bar{r}$	Vector from origin to the desired location
$\bar{r}_j$	Vector from origin to the center of the transducer element j
t	Time
t_i	Acquisition time of dynamic image i
$v_{n,j}$	Velocity perpendicularly to surface of transducer element j
w_b	Blood perfusion rate
x	Distance travelled by ultrasound in attenuating tissue
Φ	MR image phase
α	Ultrasound attenuation
α_a	Ultrasound attenuation due to absorption
α_s	Ultrasound attenuation due to scattering
α_T	Temperature dependent water chemical shift in ppm/°C
δ	Chemical shift
δ_0	Temperature independent part of chemical shift
δ_T	Temperature dependent part of chemical shift
γ	Gyromagnetic ratio
φ_j	Phase of transducer element j
λ	Ultrasound wavelength
π	Pi
ρ	Tissue density
σ	*S*creening factor
σ_T	Temperature standard deviation

List of Figures

1 Introduction

High-intensity focused ultrasound (HIFU) is an attractive and efficient noninvasive technique for local hyperthermia and ablation of pathological tissue. The mechanical ultrasound waves emitted by the transducer propagate through intact skin and can be brought to a small high-intensity focus at the desired target location, which in turn produces a rapid local temperature rise. HIFU can thus be used for selective tissue destruction by producing well-defined volumes of thermal coagulation and necrosis deep within the body while sparing surrounding tissues.

The biophysical effects of high-intensity ultrasound were first studied extensively in 1927 by Wood and Loomis (1). They observed that planar ultrasound waves, propagating in parallel towards the target, could rupture biological cell membranes provided the intensity was sufficiently high. This observation spurred a lot of interest and the first recorded mention of the possibility of using ultrasound for cancer treatment was made in 1933 (2). In 1942, Lynn *et al.* (3) suggested that a geometrically concave transducer could be used to increase the local intensity by focusing the ultrasound waves, while keeping the intensity low in surrounding areas. This allowed for inflicting tissue damage to a well-defined deep-seated focal spot while sparing surrounding tissue. Although a substantial amount of research was performed toward clinical applications (mainly ablation of the central nervous system) during the following decades (4-10), HIFU did not gain widespread clinical acceptance as a technique for local hyperthermia or tissue ablation mainly due to a lack of suitable guidance.

Magnetic resonance imaging (MRI) was first suggested for providing the necessary guidance in 1992 by Cline *et al.* (11). This noninvasive imaging modality has excellent soft-tissue contrast and is widely used for image guided interventions, and can also aid in the treatment planning of HIFU therapy. Moreover, several MR tissue parameters are altered as a result of ablation and MRI can thus also be used to visualize the extent and severity of tissue damage following treatment (12, 13). The perhaps most important utility of MRI for HIFU therapy is, however, its ability to produce high-resolution *in*

vivo temperature images that can be used to visualize the temperature rise in real-time in any imaging plane within the body (14, 15).

The clinical potential of HIFU combined with MRI (MR-HIFU) for providing noninvasive, controlled, safe, and accurate hyperthermia has seen this therapeutic modality being used for a number of applications during the past decade. The main clinical application of MR-HIFU to date has been for ablation of uterine fibroids (16-19), which are very common benign smooth-muscle tumors located within the uterus. These tumors can, if sufficiently large, assert substantial pressure on surrounding anatomical structures causing pain and a general reduction in quality of life (20). MR-HIFU has several advantages as compared to the currently available alternatives of hysterectomy and uterine artery embolization as it is less invasive, and has superior specificity, shorter recovery periods, and less risk of adverse events (17, 21). In the breast, MR-HIFU has been used for treatment of benign breast fibroadenoma (22), but also for treatment of malignant breast carcinoma (23-26). A “problem” currently inhibiting the widespread use of MR-HIFU for the ablation of breast tumors is that conventional surgical techniques are very accurate, specific, and safe. Some initial feasibility results have also been recently reported for palliative treatment of painful bone metastasis (27-29) and ablation of brain tumors with MR-HIFU (30). However, the reported use of MR-HIFU for ablation of brain tumors was invasive as it first required the removal of a piece of the skull to create a window for ultrasound access (30).

Preclinical research has also been performed on other applications, such as MR-HIFU ablation of prostate cancer (31-33). The clinical feasibility of HIFU for prostate ablation has also been shown using ultrasound guidance (34, 35). Local mild hyperthermia induced and controlled by MR-HIFU has been suggested for enhancing local drug delivery using for example chemotherapy agents encapsulated in thermosensitive liposomes (36-39), and for temporally and locally disrupting the blood-brain barrier to allow drugs to enter the central nervous system (40, 41). MR-HIFU induced mild hyperthermia has also been shown capable of providing the much needed spatial and temporal control of gene therapy by using thermosensitive promoters (42, 43).

1.1 Magnetic resonance guided high-intensity focused ultrasound ablation strategies

Traditionally, HIFU ablation has been done in one point focal point at a time followed by a cooling period to allow intervening tissues within the beam path to return to body temperature (19, 44). Due to the small size of the focal point (few millimeters in diameter at 1 MHz), this point-by-point approach requires numerous point sonications to ablate the entire region of interest, thereby making this method of ablation inherently inefficient. Recent advances in phased-array transducer technology allow for an alternative approach, as phased-array transducers can electronically displace the focus by altering the phase of the driving signal of the individual elements (45, 46). This allows for splitting the focal point into several simultaneous foci or alternatively electronically steering a single focal spot along a trajectory during continuous sonication, all while the transducer remains stationary. Phased-array transducers thus provide a freedom for creating different ablation strategies that can easily be made more efficient than point-by-point ablation.

In order to improve the ablation efficiency, larger volumes have to be ablated per sonication event, which in turn requires larger amounts of energy to be deposited for each sonication. Since all biological tissues absorb ultrasound energy to various extents, the increase in deposited energy will inevitably also lead to higher temperatures outside of the target area, particularly in the near field of the ultrasound beam path (47, 48). Hence, all potentially heated regions should be monitored by MR thermometry simultaneously to ablation in order to ensure the safety of the therapeutic procedure. This is particularly important for sensitive near-field tissue interfaces such as the skin and the interface between subcutaneous fat and muscle.

The primary aim of the research presented in this thesis was to develop an efficient yet safe method of MR-HIFU ablation for the Philips Healthcare clinical MR-HIFU system and evaluate its' efficacy in a large animal model. This is the topic of Publication **I**.

1.2 Feedback control of magnetic resonance guided high-intensity focused ultrasound

A problem of MR-HIFU therapy is that the tissue thermal response depends largely on unknown tissue properties such as perfusion, absorption, and thermal conduction. This makes it very difficult to accurately predict the appropriate power for ablating the desired tissue volume. One solution for obtaining a more reliable treatment outcome is to use a closed-loop feedback to regulate the power based on the temperature rise seen in the MR temperature images (49, 50). However, in order for the ablation to be as efficient as possible it is preferable to regulate the sonication trajectory rather than the power. This allows a high and constant power level to be used during the sonication, which is preferable because heat diffusion will spread and disperse heat with time. Considerable amounts of heat are therefore lost via diffusion if unnecessarily long sonication durations are used.

The secondary aim of this research was thus to provide a robust feedback control designed to improve the reliability of the MR-HIFU ablation strategy developed for the Philips Healthcare MR-HIFU system in Publication **I**. This is the topic of Publication **II**.

1.3 Motion compensation of magnetic resonance thermometry and high-intensity focused ultrasound ablation

Proton resonance frequency (PRF) shift based MR thermometry is the most commonly used method of MR thermometry and uses the phase difference between dynamically acquired images to calculate the temperature change (15). This makes PRF thermometry sensitive to phase perturbations by for example accidental motion or physiological activity. Several pathologies in the abdomen are very good candidates for MR-HIFU but are subject to both rigid and non-rigid motion during the respiratory cycle, which may induce artifacts in the PRF thermometry if appropriate corrections are not applied.

Classical image registration techniques, such as estimation of affine transformation and optical flow, have proven capable of removing misregistrations between subsequent

dynamic images due to in-plane motion (51-54). However, although the imaging plane can be aligned with the main axes of organ motion in order to reduce the 3D motion compensation problem to compensation of in-plane motion, this approach imposes an unnecessary constraint by removing the freedom to choose the position of the imaging slice. A preferable approach would be to use some form of real-time through-plane motion compensation, which is possible using conventional pencil-beam navigators (55). These navigators are, however, designed for the tracking of the diaphragm motion during breathing and are not well-suited for the direct tracking of the organs of interest, which is necessary for accurate motion compensation. The conventional navigators suffer from mainly two disadvantages: the navigator signal has poor contrast within the abdomen and the inevitable cross-section of the navigator with the imaging plane perturbs the magnetization at the cross-section. The resulting phase perturbations may again give rise to artifacts in the temperature images or at the very least reduce the temperature accuracy. The resulting perturbation of the navigator at the cross-section may in turn be problematic for the motion estimation algorithm, especially if the induced partial saturation is the dominant feature within the navigator profile as may well be the case. However, because the fat is typically discarded from thermometry in order to avoid erroneous temperature readings, a fat-selective pencil-beam navigator would avoid perturbing the magnetization of the imaging slice and vice versa. Such a navigator would also provide a good contrast as fat is commonly abundant in the abdomen and most abdominal organs are surrounded by a sheath of fat.

Even though misregistrations between the dynamically acquired images are corrected accurately, non-temperature dependent phase fluctuations generally remain (56, 57). These phase fluctuations are caused by variations in the local magnetic field experienced by the organ during the respiratory cycle, which in turn arise due to an inhomogeneous *in vivo* magnetic field. The use of a multi-baseline method is a common approach for addressing these phase-fluctuations (51, 56, 58). In this approach, a look-up-table of numerous reference phases are acquired in a training stage with no heat applied. Then during hyperthermia, the appropriate reference phase image that represents the current stage of the respiratory cycle is retrieved from the look-up-table.

If the look-up-table is sparsely populated, temperature artifacts may occur due to discretization when the closest match is chosen from the look-up-table during hyperthermia. Furthermore, the indexing and retrieval from the look-up-table has traditionally been performed using image based information (51, 58), which is incapable of taking into account out-of-plane motion that may also affect the local magnetic field fluctuations.

Provided the algorithms are efficient, it is possible to obtain accurate 3D motion compensated temperature images in real-time by combining in-plane, through-plane, and phase-reference corrections. The obtained motion estimate may also be used to steer the HIFU beam according to the 3D motion of the target, thereby keeping the focal spot fixed within the mobile target. This would allow for a fully 3D motion compensated MR-HIFU ablation or hyperthermia procedure of any abdominal organ, provided an acoustic path can be found for the ultrasound to propagate from the transducer to the target.

The third aim of the thesis was thus to develop and demonstrate the feasibility of a fat-selective navigator for providing the missing real-time through-plane motion correction for a fully 3D motion compensated MR-HIFU ablation procedure. The development and demonstration of the feasibility of the fat-selective navigator for through-plane motion correction was the topic of Publication **III**. The demonstration of the improved multi-baseline correction accuracy obtained when using a model-based look-up-table correction with navigator information for accurate indexing was the topic of Publication **IV**. Three-dimensional motion compensation of MR thermometry was in turn the topic of Publication **V**. The feasibility of a fully 3D motion compensated MR-HIFU ablation, including real-time motion compensation of both thermometry and focal point position, was demonstrated in Publication **III** on *in vivo* porcine kidney. The presented fat-selective navigator was utilized for a more accurate through-plane motion estimation and compensation.

1.4 Context of this thesis

The bulk of the work performed for this thesis was part of a group effort at Philips Healthcare, Finland, and the IMF (Imagerie Moléculaire et Fonctionnelle) laboratory at the University of Bordeaux, France, to develop and validate an instrument for efficient and safe delivery of non-invasive therapy by MR-HIFU. The Food and Drug Administration (FDA) in the USA, and other regulatory bodies, have stringent requirements on the technical and scientific basis for the function and performance of such systems, and for documenting that these requirements are fulfilled. Several novel methods and specifications have been developed for this clinical MR-HIFU platform that is currently being utilized in a pilot study for the ablation of uterine fibroids. The most important results of the related research and the necessary physics background are presented in this thesis. This research is presented in Publications **I** and **II**.

The latter part of the thesis describes the research performed towards demonstrating the feasibility of MR-HIFU ablation of abdominal organs, particularly the kidney and liver. Related research has been performed at the IMF laboratory in Bordeaux since the beginning of the decade and the feasibility of several methods aimed at reducing motion induced temperature artifacts to an acceptable level have been convincingly demonstrated. Recent development in computer hardware combined with the MR-HIFU platform developed by Philips Healthcare allowed for further progress towards the goal of real-time motion compensated MR-HIFU ablation of abdominal organs. Some of the more important results of the related research are presented in this thesis along with the necessary background for understanding the problems and the proposed solutions. This research is presented in Publications **III** – **V**.

The thesis is divided in two parts focused on the two central components of MR-HIFU: The methods for delivering the energy, high-intensity focused ultrasound (HIFU, Section 2), and the means of measuring the temperature change, planning the treatment and validating the outcome, magnetic resonance imaging (MRI, Section 3). The aims of the thesis are summarized below and the fulfillment of these aims is discussed in the

conclusions (Section 4). A brief summary of the main results of the publications is also provided (Section 5).

	Aims	Publication
1.	Develop a safe and efficient method for clinical MR-HIFU ablation.	**I**
2.	Develop a feedback control algorithm to improve the reliability of the MR-HIFU ablation strategy developed under aim 1.	**II**
3.	Develop a real-time through-plane motion compensation method to enable 3D motion compensation of MR-HIFU for the treatment of mobile organs.	**III, IV, V**

2 High-intensity focused ultrasound therapy

This chapter focuses on technical aspects of HIFU induced tissue destruction. Different sonication strategies are discussed in a separate subsection, with emphasis on the volumetric sonication strategy developed in Publication **I**. Feedback control methods, which may be used to improve the reliability and consistency of the induced tissue damage, are also discussed. Different methods of feedback control are distinguished and the binary feedback developed in Publication **II** is described in detail.

The generation of HIFU and the interaction of HIFU with biological tissue are also briefly described as they constitute the foundation for any HIFU therapy and are furthermore necessary background in the discussion of the different sonication strategies and methods of feedback control. The book *Physical principles of medical ultrasonics* compiled by Hill, Bamber, and ter Haar, can be recommended for more information on therapeutic ultrasound and the interaction of ultrasound with biological tissue (59).

2.1 High-intensity focused ultrasound physics

2.1.1 Focused ultrasound and acoustic properties of therapeutic HIFU

Most modern HIFU transducers are made of a piezoceramic or piezocomposite material and have the shape of a spherical shell (19, 44, 46, 60-66). Figure 2.1 shows a schematic of a such a geometrically focused spherical shell transducer as first suggested by Lynn *et al.* in 1942 (3). The resulting focus is located close to the geometrical center of curvature and the increase in the intensity at the focal spot can easily be a factor of 1000 as compared to using non-focused plane waves. Commonly used spatial maximum intensity levels for HIFU ablation are around 1000 – 3000 W/cm^2, whereas the intensity levels used for diagnostic ultrasound are around 0.1 – 0.5 W/cm^2 (59, 67-72). Diagnostic ultrasound is furthermore applied in short bursts of a few microseconds, whereas HIFU is applied continuously for several tens of seconds (59, 70-74). The size of the focus is commonly determined as the full width at half maximum (FWHM), or as the size at -3 dB or -6 dB (51, 64, 65, 71, 75). Whatever the used definition, the size of

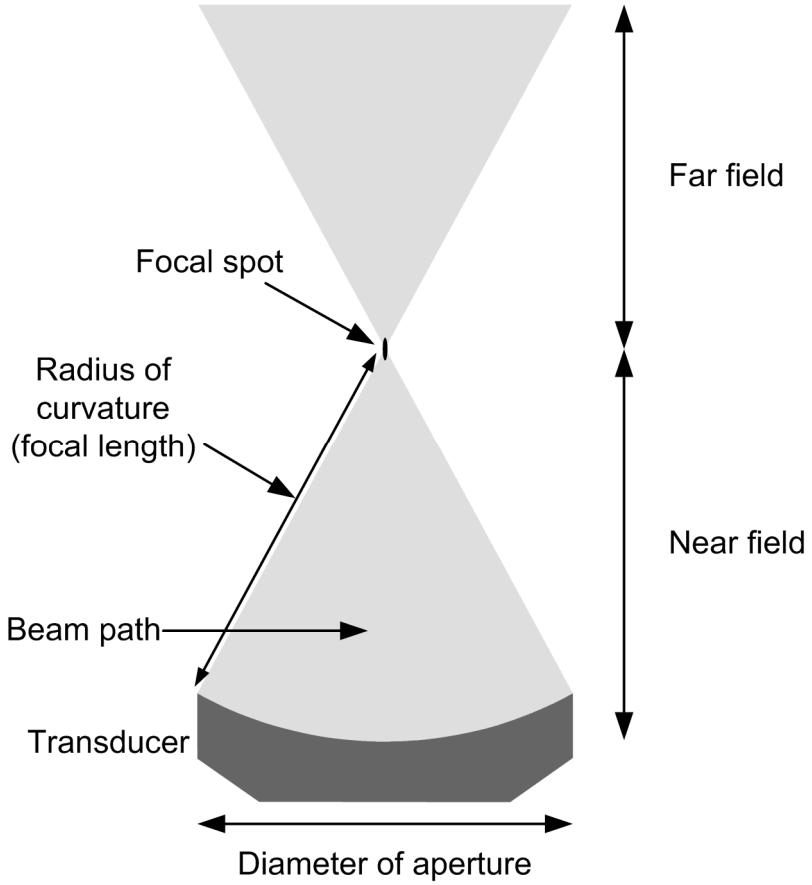

Figure 2.1: Schematic of a spherical shell transducer. The ellipsoid focal spot (in black) is in scale with the radius of curvature and aperture.

the ellipsoid focal spot is determined by the ratio of the transducer radius of curvature and the diameter of the aperture, and is also linearly dependent on the wavelength. The wavelength λ is in turn determined by the chosen frequency f according to

$$\lambda = c / f \,, \tag{2.1}$$

where c is the speed of sound in the target tissue, which is typically close to that of water in human soft tissues *i.e.* approximately 1540 m/s (76, 77). For a typical extracorporeal HIFU transducer, such as that used in Publication **I** with a 12 cm radius of curvature and 13 cm aperture diameter, the ellipsoid focal spot had a width and length of approximately 1 mm and 7 mm, respectively, when the transducer was

operated at 1.2 MHz. In general, the ultrasound frequency used for HIFU therapy depends on the target and the required penetration depth, with extracorporeal transducers typically using frequencies in the range of 0.8 – 1.6 MHz, whereas intra-cavitary transducers for such applications as prostate ablation use higher frequencies in the range of 2 – 4 MHz (19, 22, 35, 65, 78-80).

2.1.2 Phased-array transducers and electronic focal point deflection

HIFU transducers can advantageously be designed as phased arrays to increase the flexibility and efficiency of the HIFU therapy (46, 61-63, 66, 81-84). The increase in flexibility comes from the fact that phased-array transducers consist of multiple piezoelements that can each be driven with an individual phase and amplitude. This allows for ablating larger tissue volumes during a single sonication event without the need for mechanical displacement since the focal spot of the phased array HIFU transducer can be electronically steered by altering the phase of the different elements as shown in Figure 2.2.

The phase required for any given element φ_j in order to obtain constructive interference at the desired focal spot is determined by

$$\varphi_j = 2\pi \frac{l_j}{\lambda}, \tag{2.2}$$

where $l_j = \left|\bar{r} - \bar{r}_j\right|$ is the distance from the center of the element $\bar{r}_j$ to the desired focus location $\bar{r}$ as shown in Figure 2.2. The phase of the different elements can be uniformly shifted without affecting the focal point position. This is because it is the relative phase of the element pressure fields that determines whether or not constructive interference is obtained at the desired location. The pressure field of an electronically steered phased-array transducer may be written as a linear sum of the pressure fields emitted by the individual elements, if neglecting nonlinear effects as is commonly done. Using the

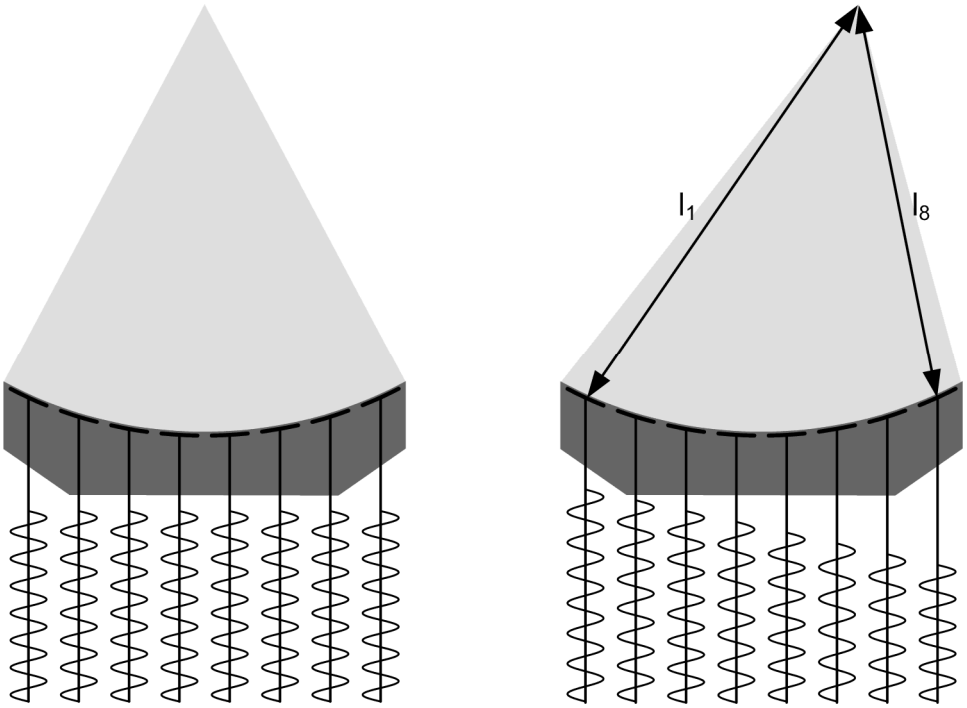

Figure 2.2: Schematic of a phased-array transducer with eight elements focused at the geometric focus (left) and deflected perpendicularly to the beam axis (right). The sinusoidal signals coming in from below all have the same phase with respect to each other when focusing at the geometrical focus. By changing their relative phase it is possible to electronically steer the focus away from the geometrical focus.

Rayleigh integral, the pressure field in a homogeneous medium may be written as (61, 85)

$$p(\bar{r}) = \frac{\mathrm{i}kc\rho}{2\pi} \cdot \sum_{j=1}^{N} v_{n,j} \left(\iint_S \frac{\exp\left(-\mathrm{i}k\left|\bar{r} - \bar{r}_j\right|\right)}{\left|\bar{r} - \bar{r}_j\right|} \mathrm{d}S_j \exp\left(\mathrm{i} \cdot \varphi_j\right) \right), \tag{2.3}$$

where the ρ is the tissue density, $k = 2\pi f/c - \mathrm{i}\alpha$ is the combined wave-number and attenuation, $v_{n,j}$ is the velocity perpendicularly to the surface of element j and φ_j is the phase at which the element is driven. The integral is over the surface of the individual elements, each with an identical area S, and the summation is over all N elements in the phased array. For layered tissues, Equation 2.3 can be used by propagating the pressure

field to one tissue layer at a time, taking into account reflection, transmission and diffraction (85-88). The intensity may in turn be written as

$$I(\bar{r}) = \frac{|p(\bar{r})|^2}{c\rho}, \tag{2.4}$$

where $p(\bar{r})$ is the pressure obtained from Equation 2.3. Figure 2.3 shows the intensity distribution calculated with Equation 2.4 for a 256-element phased-array transducer focused at the geometrical focus and electronically deflected perpendicularly to the beam axis by 8 mm. Some weak secondary lobes can be seen when the focus is deflected off-axis by 8 mm.

The range over which electronic steering can be performed is limited by the aperture of the individual elements as the transducer elements have a finite size (typically between 2 – 10 mm in diameter (46, 51, 64)) and thus directional pressure field (shown in Figure 2.4). Excessive off-axis steering from the geometrical focus will therefore result in a severe decrease in focus intensity, incompatible with HIFU ablation. Consequently, phased-array HIFU transducers are commonly limited to approximately ±10 – 20 mm electronic deflection perpendicularly to the beam axis, and 20 mm along the beam axis away from the geometrical focus (46, 51, 64, 89). Moderate electronic steering along the beam axis towards the transducer increases the focal spot intensity, whereas excessive deflection will reduce the intensity as the desired focal spot will be outside the aperture of several elements.

In addition to a drop in maximum intensity, electronic deflection will also alter the shape of the focal spot as well as introduce secondary unintended parasite foci also referred to as grating or secondary lobes. Deflection perpendicular to the beam axis will for example broaden the focal spot, whereas moderate deflection towards and away from the transducer will shorten and elongate the focus, respectively. Secondary lobes will typically occur in the opposite direction of deflection when deflecting off-axis,

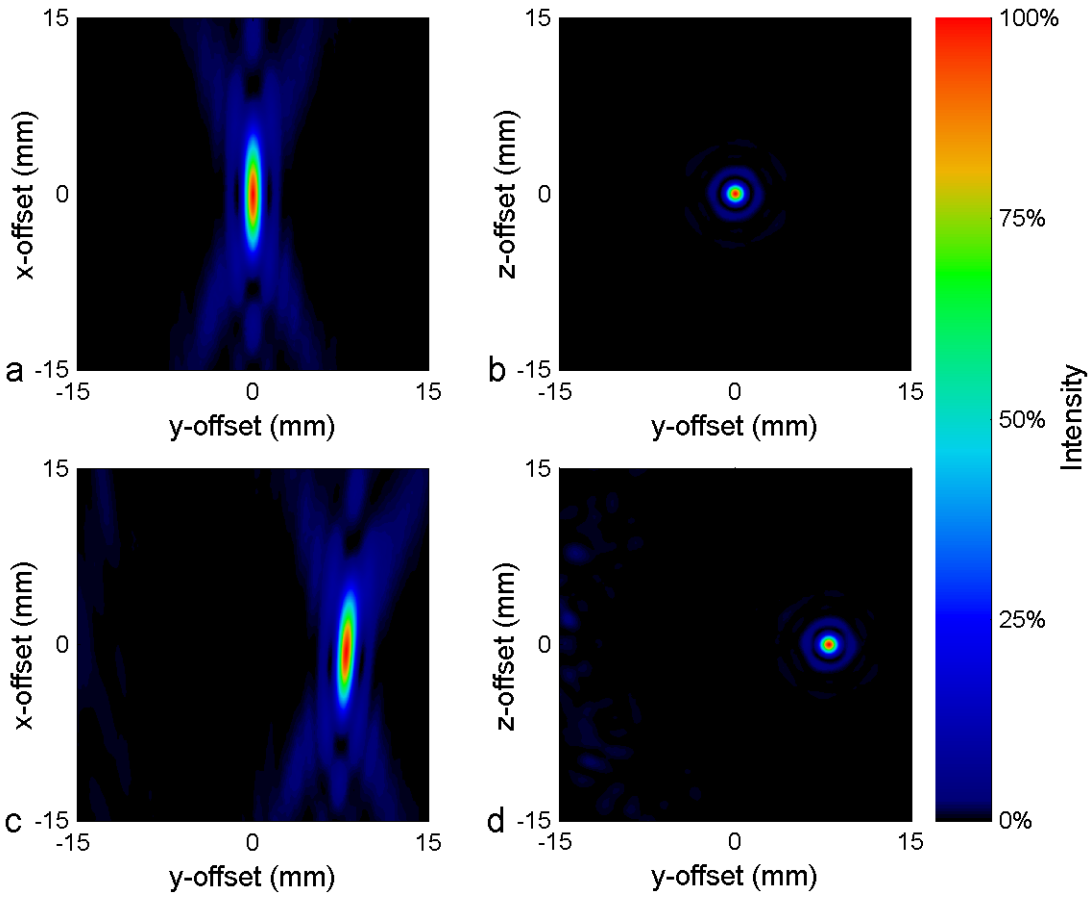

Figure 2.3: Theoretical intensity distributions of a spherical shell 256-element phased-array transducer (12 cm radius of curvature) with no electronic deflection (a, b) and with an 8 mm off-axis electronic deflection (c, d). The intensity distributions, centered on the geometrical focus, are shown along the beam axis in the plane of electronic deflection (a, c) and perpendicular to the beam axis (b, d). Both views are centered on the focal point.

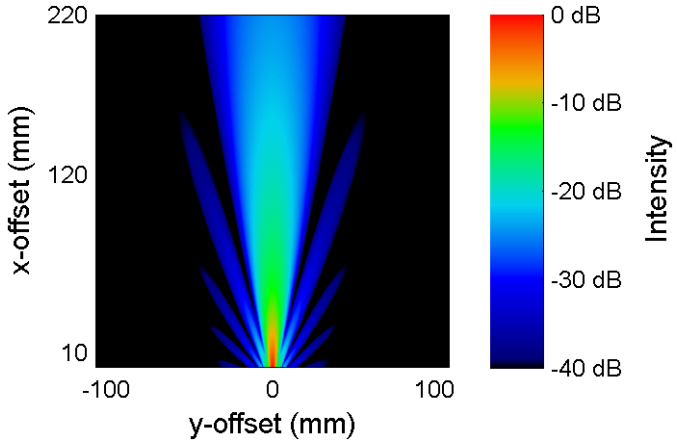

Figure 2.4: Intensity distribution of a single transducer element with a diameter of 7 mm, 12 cm radius of curvature, and 1.2 MHz operating frequency.

whereas these lobes are not as severe for deflection along the beam axis. The design of the phased-array transducer greatly affects the amount and severity of the side lobes (46, 63, 64, 89). A symmetrically sectioned transducer surface, such as an annular (90-92), sector-vortex (66, 90, 93), hexagonal (46, 63, 64), and spherical (61, 62) sectioned surface, may give rise to grating lobes even when no deflection is performed if a particularly high degree of symmetry is used such as for hexagonal or square element positioning (46, 63, 64). Furthermore, off-axis deflection with these regular designed arrays increases the severity of these secondary foci (46, 63, 64, 89). By reducing the regularity and symmetry of the element positioning, by for example utilizing a pseudo-random design, the level of the secondary lobes can be dramatically reduced thereby allowing for significantly improved beam-steering capabilities (46, 63, 64, 89).

2.1.3 MR-HIFU platform

Ultrasound waves cannot propagate in air and need an acoustic path from the transducer and into the body. This is accomplished in clinical HIFU platforms by submerging the transducer in a degassed water-bath that is sealed within an MR compatible table top using a thin membrane (19, 44, 75). This membrane also acts as an acoustic window through which the ultrasound waves may propagate. Alternative methods where the transducer is confined in a plastic bag inside a table-top have also been suggested (94). This HIFU table top can be used as any other conventional MR patient table, and can be moved in and out of the MR scanner. A gel pad is often positioned on top of the membrane to improve the acoustic coupling between the water tank and the skin of the patient (19, 95). Ultrasound gel or degassed water may also be applied at both sides of the gel pad, or alternatively instead of the gel pad, to improve the acoustic coupling at the interfaces between the water tank and the patient (19, 22, 95). A schematic of a pig positioned on top of the Philips clinical HIFU platform can be seen in Figure 2.5. Intra-cavitary transducers intended for prostate ablation use an entirely different setup as the casing of the transducer is in direct contact with the wall of the cavity (80, 96, 97).

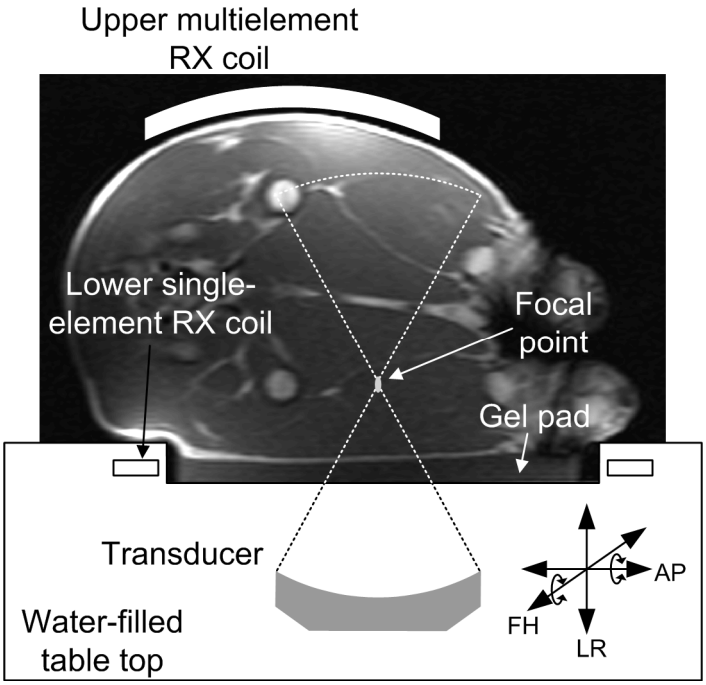

Figure 2.5: Schematic of the Philips clinical HIFU platform viewed in the transverse plane with a pig placed in a left decubitus position on top of the platform. The integrated multielement MR receive coil is also shown. The lower element is a loop surrounding the acoustic window in the table top through which the ultrasound propagates. The piezoelectric motors that control the positioning allow for three degrees of translational motion and two degrees of rotational motion. This HIFU platform is used in Publications **I – III**. Reproduced from Publication **I** with permission from AAPM.

Accurate and flexible positioning of the transducer is a crucial prerequisite for inducing localized thermal damage in the desired target region. Conventional motors cannot be used inside the MR and early positioning devices used hydraulic pistons to accurately position the transducer (44, 75, 98). More accurate positioning devices have since been developed, and most modern HIFU transducer positioning devices are software controlled and use piezoelectric motors (22, 99, 100) or robotics (101, 102) for accurate mechanical displacement of the transducer. More details on the Philips clinical HIFU platform can be found in Publication **I**.

2.2 Interaction of high-intensity focused ultrasound with tissue

2.2.1 Ultrasound propagation and tissue heating

As ultrasound propagates through biological tissue it loses energy, or becomes attenuated, partially through absorption and partially through scattering. The fluctuations in pressure induce vibrational and rotational motion of the tissue molecules that in turn causes a rise in temperature (59, 79). This phenomenon can also be interpreted as absorption and conversion of mechanical ultrasound energy into heat energy. The scattering of ultrasound due to tissue inhomogeneities will also affect the energy of the propagating wave, since the scattering will redirect and disperse the ultrasound waves out of the main beam. The attenuation of the propagating pressure caused by both absorption and scattering can be written as

$$p(x) = p_0 \exp(-\alpha x), \tag{2.5}$$

where p_0 is the initial pressure profile directly outside of the transducer surface, and x is the distance travelled by the ultrasound in the tissue with an attenuation coefficient $\alpha = \alpha_a + \alpha_s$ that contains both an absorbing and scattering component. Higher ultrasound frequencies cause an increase in attenuation, with the relationship being approximately linear for most biological soft tissues within the frequency range of interest for therapeutic HIFU (59). The attenuation varies significantly for different human tissues with aqueous tissue such as blood having a low attenuation of approximately $1\ \mathrm{NpMHz^{-1}m^{-1}}$, soft tissues such as muscle have a slightly higher attenuation of $4 - 15\ \mathrm{NpMHz^{-1}m^{-1}}$ and bone has a very high value of $150 - 300\ \mathrm{NpMHz^{-1}m^{-1}}$ (59, 76, 103). There is, however, significant variation in the attenuation of any biological tissue type. The attenuation can even vary greatly within the same individual for inhomogeneous tissue types, such as uterine fibroids.

Tissue interfaces within the beam path may cause reflection due to a mismatch between the acoustic impedance of the two tissues, although the impedances of biological soft tissues are very similar and this effect is mostly negligible (59, 77, 103). However,

ultrasound waves reaching a tissue interface at an angle may be subject to both reflection and refraction (85-88). The reflection will reduce the energy contained in the transmitted ultrasound beam, whereas refraction will alter the direction in which the transmitted ultrasound waves continue to propagate in the new tissue layer. This refraction may shift the focus away from the geometrical focus, dephase and/or distort the focal spot (85-88). If a phased-array transducer is used and the speed of sound in the different layers can be determined (with for example CT imaging (104, 105)) then the focal spot may be recovered at the desired location by applying appropriate phase corrections (85, 88).

The resulting temperature rise caused by absorption of HIFU energy is often described using Pennes' bioheat transfer equation (106) that takes into account the heat diffusion as well as heat loss through perfusion. The temperature rise induced by ultrasound as estimated by the bioheat transfer equation is given by

$$\rho c_{\mathrm{t}} \frac{\partial T(\bar{r},t)}{\partial t} = k_{\mathrm{t}} \nabla^2 T(\bar{r},t) - w_{\mathrm{b}} c_{\mathrm{b}} \left(T(\bar{r},t) - T_{\mathrm{ar}}\right) + \alpha_{\mathrm{a}} I(\bar{r},t), \qquad (2.6)$$

where $T(\bar{r},t)$ is the temperature distribution at time t, c_{t} and c_{b} are the specific heat of the tissue and blood pool, respectively, k_{t} is the heat conductivity of the tissue, w_{b} is the blood perfusion rate, T_{ar} is the temperature of the arterial blood, and the intensity $I(\bar{r},t)$ is the intensity of the ultrasound as given by Equation 2.4. Heat conductivity does not vary significantly between different biological soft tissues and can be taken to be around 0.6 $\mathrm{Wm^{-1}{}^{o}C^{-1}}$, with the exception of fat which is a good insulator and has a lower conductivity of around 0.2 $\mathrm{Wm^{-1}{}^{o}C^{-1}}$ (88, 107). The rate of perfusion is significant in highly perfused organs such as the kidney or liver, notably reducing the heating efficiency of HIFU in these organs, whereas perfusion has much less of an effect in other soft tissues (107-109). The absorption coefficient used in the bioheat transfer equation is often assumed to be the same as the attenuation coefficient, since absorption and scattering can difficultly be distinguished and both are related to similar phenomena (59, 88).

2.2.2 High intensity phenomena

At sufficiently high pressure amplitudes, the single frequency sinusoidal waveform may begin to distort and a shock-front can gradually form (59, 79, 110). This nonlinear ultrasound propagation causes energy to be transferred from the main frequency to the higher harmonics that in turn results in a local increase of energy absorption due to the increase in the absorption coefficient at higher frequencies (59, 79, 110-112). Nonlinear propagation may thus be utilized to increase the heating efficiency at the focus by applying sufficiently high power levels to generate higher harmonics near the focus (110, 112). Despite proof that nonlinear ultrasound propagation may be significant at the intensities used in HIFU ablation (110-112), these effects are commonly ignored and the temperature is assumed to scale linearly with the applied power.

As ultrasound propagates through tissue, the alterations in local pressure may induce small cavities in the tissue if the pressure amplitude is sufficiently high (67, 113). This process is referred to as cavitation (114). The intensity levels at which cavitation occurs is in the vicinity of where nonlinear effects may become significant (67, 112, 113). Hence, cavitation may occur at the intensities used for HIFU ablation (67, 68, 113). It is, however, often desired to avoid cavitation, since it may cause uncontrolled and unpredictable tissue damage in and near the target region (68, 95, 115, 116). Cavitation monitoring is therefore commonly utilized to detect the onset of potentially detrimental cavitation (32, 67, 68, 113). The presence of cavitation may nevertheless facilitate the HIFU ablation by improving the heating efficiency. This is because the multiple scattering of incident ultrasound waves within the cloud of bubbles induced by cavitation effectively traps the ultrasound within this region, thereby increasing the local absorption of ultrasound energy (67, 117).

2.2.3 Thermal dose

The concept of thermal dose was introduced as a measure of thermal damage by Sapareto and Dewey in 1984 (118). This model, which is based on the Arrhenius model of physical reaction rate, does not only take into account the current temperature but

also the entire temperature history in estimating the thermal damage. The equation describing the thermal dose is written as

$$TD_{43}(t) = \int_0^t R^{(43-T(\tau))} \mathrm{d}\tau \,, \tag{2.7}$$

where

$$R = 0.25 \quad (T < 43)$$
$$R = 0.5 \quad (T \geq 43)$$

and TD is the thermal dose in equivalent minutes at 43 ºC (EM), t is the time and $T(\tau)$ the time-dependent temperature. Due to the logarithmic relationship between the thermal dose and temperature, the spatial distribution of the thermal dose is typically much sharper than for the somewhat diffuse temperature. The thermal dose thresholds for different levels of thermal damage have been shown to differ somewhat between tissues (119-125). However, a threshold of 240 EM is generally considered to be a good representative for full coagulative necrosis (74, 100, 115, 125-127). Similarly, 30 EM has been reported to be a relevant predictor for onset of tissue damage (74, 125). These thresholds are therefore used in Publication **I** and **II**, as indicators of moderate tissue damage and complete necrosis.

In the presence of thermal noise, the logarithmic temperature relationship of the thermal dose will induce errors in the thermal dose estimate if the effect of thermal noise does not average to zero. If a normal distribution of the temperature is assumed, as is commonly done for the temperature estimates obtained from MR thermometry (see Section 3.2.1), then the thermal dose increments will follow a log-normal distribution. Normal noise with a standard deviation of σ_T (°C) will thus on average result in an overestimation of the thermal dose with a factor of

$$\exp\left(0.5\sigma_T^2 \ln^2 2\right) \tag{2.8}$$

if no compensation is applied (128, 129). Hence, for a relatively low temperature standard deviation of 1.2 °C as in Publication **I**, the thermal dose would be overestimated by 40%, whereas for a slightly higher temperature uncertainty, $\sigma_T = 2$ °C, the overestimation exceeds 150%. The overestimation can, however, be accounted for by dividing the thermal dose obtained from Equation 2.7 with the overestimation factor of Equation 2.8.

2.2.4 Histology

The volume of induced tissue damage is sometimes referred to as a thermal lesion, particularly in histology (100, 129-135). It should be noted that a thermal lesion is commonly taken to indicate the tissue thermal damage inflicted by a single ablation. Three regions of different levels of thermal damage can commonly be distinguished within the HIFU induced thermal lesions (131, 136). The central white zone, red peripheral zone and outer halo zone, named after their appearance on gross examination of fresh tissue following excision, can be seen in Figure 2.6. The thermal damage is most severe in the central white and red peripheral zones, and an acute inflammatory response, necrotic blood vessels, and congestion of blood flow can generally be observed, all indicative of irreversible coagulative necrosis (131, 136-138). Oedema is, however, more severe in the peripheral red zone, where the cells are also more commonly fragmented (131, 138). The outer halo zone, sometimes not identified, typically appears only to be oedematous without necessarily any other indication of tissue damage (131, 136). More details on the histological results commonly encountered for thermal lesions induced by HIFU can be found in Publication **I**, where *in vivo* thermal lesions induced in porcine thigh with the proposed volumetric ablation strategy were analyzed both via gross pathology and histology to verify the extent of tissue damage.

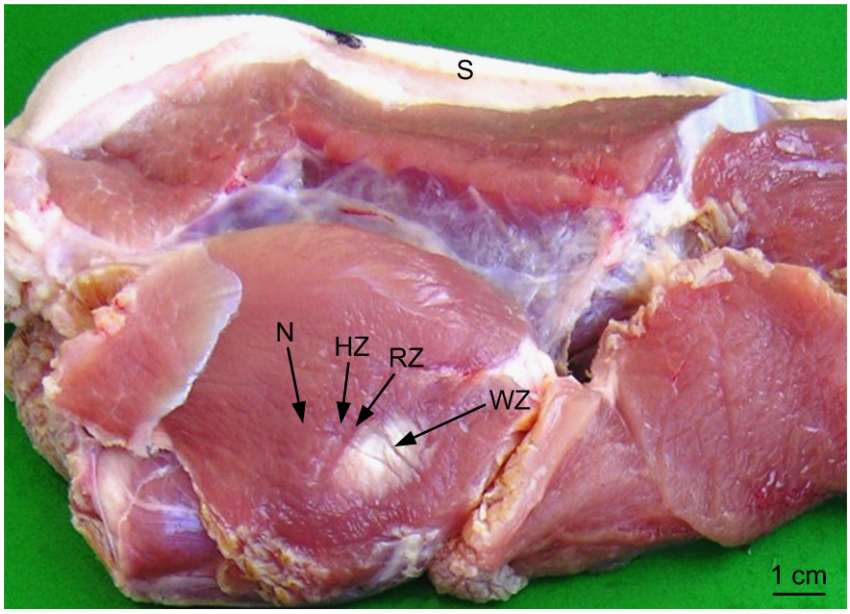

Figure 2.6: Gross pathology of fresh porcine muscle tissue. The thermal lesion can clearly be identified and contains three different regions: a central white zone (WZ), a red peripheral zone (RZ), and an outer halo zone (HZ). The skin (S) and normal tissue (N) are also identified. The longest axis of the ellipsoid thermal lesion is perpendicular to the skin and was parallel to the axis of the HIFU beam path.

2.3 Sonication strategies (I)

The volume targeted for HIFU therapy is typically larger than the size of the focal point. Traditionally, this has been solved by iteratively sonicating a single focal point at a time until the desired volume is ablated, as schematically demonstrated in Figure 2.7 (19, 23, 44, 116, 127, 134, 139). Each sonication is typically followed by a delay to allow the skin and fat layer in the near field to cool down before the next sonication (47, 48, 116, 139, 140). This point-by-point sonication method is inherently inefficient since a large part of the applied heat is lost via heat diffusion out of the small sonicated region without being utilized for ablation. Moreover, a large amount of single point ablations are needed to cover the target region, each separated by a cooling period, which further reduces the efficiency of this sonication strategy (47).

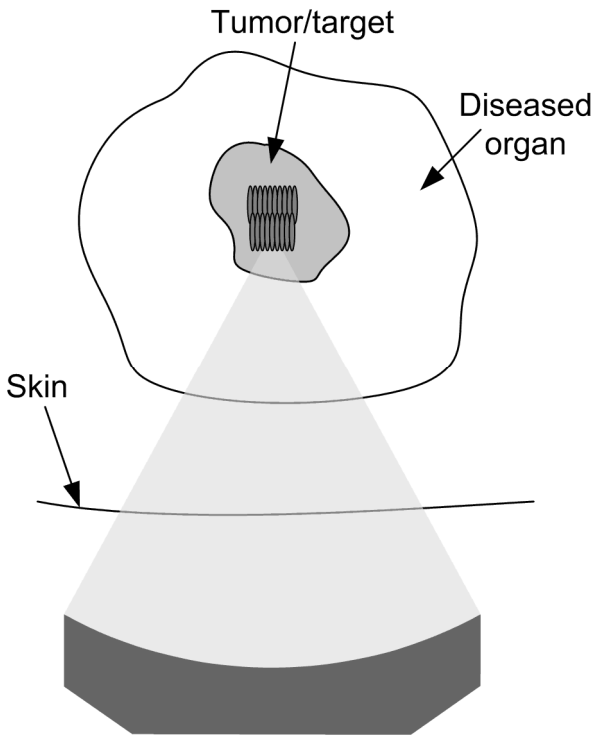

Figure 2.7: Schematic drawing of a traditional sonication strategy using several overlapping single point ablations to cover the target region.

By utilizing mechanical displacement, a larger region can be ablated per sonication by mechanically scanning the focal point around the target region (98, 141-143). If the speed and trajectory of the scanning are chosen appropriately, then a contiguous volume can be ablated. The main disadvantage of this approach is that the instantaneous temperature distribution around the focal point can become very inhomogeneous due to the relatively slow mechanical displacement of the transducer and the focal point (98, 143). This is more of a problem for ablative sonications where higher temperatures are required than for mild hyperthermia. The mechanical movement of the transducer inside of the MR scanner also induces changes in the magnetic field as the susceptibility of the transducer and surrounding water bath are not the same. These magnetic field perturbations need to be corrected in order to avoid artifacts in the MR temperature images calculated with PRF thermometry (see Section 3.2). Although such a correction can be performed (144), residual artifacts are nevertheless likely to persist.

Another alternative for increasing the ablation volume per sonication is to use multiple transducers that either remain stationary or are mechanically translated during sonication (145-149). However, the successful fitting of the multiple transducers into the MR-HIFU table-top and magnet bore can prove difficult. If mechanical movement becomes necessary during sonication then the same issues of magnetic field perturbation as for the single transducer approach remain.

Phased-array transducers make the need for mechanical displacement during sonication obsolete by allowing for rapid ablation of volumes larger than a focal spot while the transducer is stationary. This can be achieved by precisely adjusting the relative phase of the acoustic waves generated by each element to split the focus into multiple simultaneous foci (45, 48, 62, 84, 150) or alternatively temporally switch between predetermined multifoci patterns while continuously sonicating (66, 150-153). However, a problem of multifoci patterns is that they suffer from energy deposition in side lobes that may be located outside of the intended ablation region (61, 62, 83). This is especially a problem for transducers with a high degree of symmetry or when numerous simultaneous foci are used (61).

The approach presented in Publication **I** overcomes this problem by electronically switching a single focal point between a number of predetermined locations, thereby minimizing unwanted secondary foci and maximizing heating efficiency. The volumetric sonication strategy proposed in this publication used a single focal spot that was electronically steered along a trajectory consisting of multiple outward-moving concentric circles, inspired by the inside-to-out spiral trajectories of Salomir *et al.* (98). These circles were positioned in a plane perpendicular to the beam axis and centered on the axis of propagation. Each circle contained several predetermined focal points that were regularly positioned on the circumference of the circle. The sonication duration for each circle was determined via off-line simulations using Pennes' bioheat equation (Equation 2.6). An example trajectory is shown in Figure 2.8. The proposed trajectory design is flexible and allows differently sized trajectories to be generated by simply adding or removing outside circles.

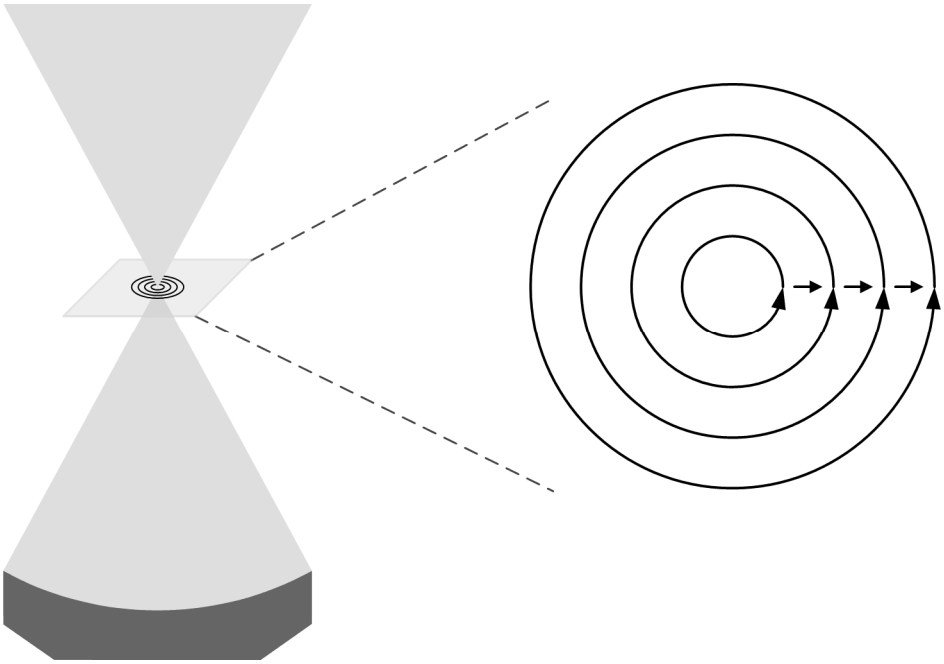

Figure 2.8: Schematic of the volumetric trajectories in Publication **I**. The trajectories are centered on the axis of propagation and positioned in the plane perpendicular to the beam axis. The close-up clarifies the design of the volumetric trajectories: sonication of each concentric circle, outwards movement to following circle at end of predetermined sonication time of circle, and end of sonication after predetermined sonication time of final circle.

This design of concentric outward-moving circles is energy efficient because it utilizes the inherent outwards diffusion of heat already deposited during the sonication of the inner trajectory circles to elevate the starting temperature of the outer circles. Consequently, less heat is lost via diffusion out of the region of interest and the energy efficiency is significantly improved with trajectory size, while the temperature gradients at the borders remain steep. Moreover, the circular shape of each sub-trajectory is also more energy efficient than sub-trajectories with corners. For example, square shaped sub-trajectories would require excess heat to be deposited at the corners in order to maintain the intended shape of the temperature distribution, because heat diffusion will strive towards eliminating temperature gradients. Furthermore, the rapid and repetitive sweeping of the sonication locations on each circle with the distance between consecutive locations maximized, ensured an even heat elevation over the sonicated

circle. Further details on the design of these volumetric trajectories can be found in Publication **I**.

In Publication **I**, the volumetric sonication design of concentric circles was evaluated by performing a total of 32 ablations on *in vivo* porcine thigh. Three differently sized trajectories with a diameter of 4 mm (1 circle), 12 mm (3 circles), and 16 mm (4 circles) were tested. A similar power level was used for the different trajectories, but the sonication time was longer for the larger trajectories in order to provide sufficient energy to the target area. The power used was constant and high, but the target region intensity was kept below levels known to cause cavitation. An example of the temperature rise and thermal dose created by these volumetric sonications can be seen in Figure 2.9. The ablated volume for each sonication was determined assuming an ellipsoid thermal lesion shape. The diameter and length of the thermal lesion was estimated from the thermal dose volume above 240 EM, as calculated from the temperature maps obtained with multiplane MR thermometry (see Section 3.2.8). The energy efficiency (calculated as thermal dose volume above 240 EM per unit of deposited energy) increased with trajectory size and was 0.03, 0.24, and 0.52 cm^3/kJ, for the 4, 12, and 16 mm diameter trajectories, respectively. The proposed volumetric sonication strategy created well-defined thermal lesions with thermal dose uniformly above 240 EM within the trajectory and sharp thermal dose borders. The transition zone between the necrotic thermal lesion and surrounding healthy tissue was very narrow as estimated by the thermal dose and confirmed by histology. Although the amount of sonications needed is reduced when using volumetric ablation, several sonications are nevertheless needed to treat large uterine fibroids that may be as large as 350 cm^3 (154).

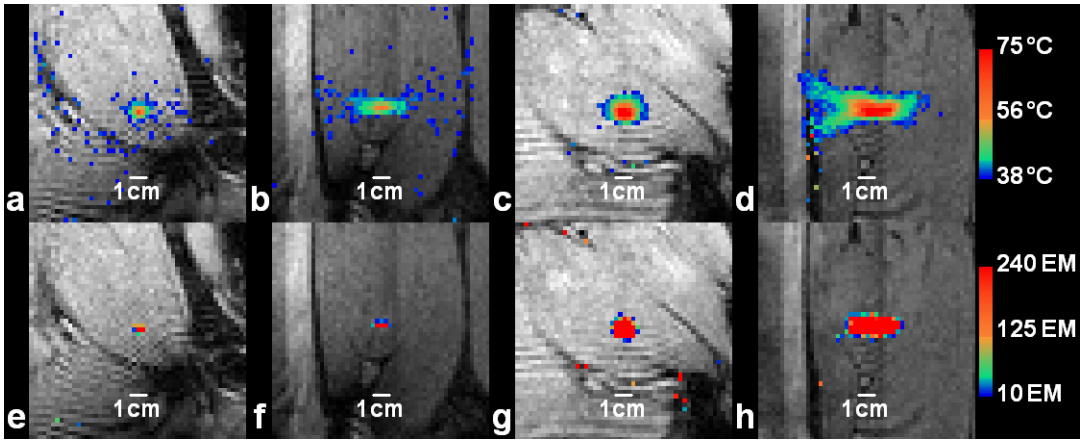

Figure 2.9: Typical target region temperature and thermal dose for a 4 and 16 mm diameter trajectory viewed in the coronal and sagittal plane. The shown temperature and thermal dose images were acquired at end of sonication and 4 min after end of sonication, respectively. The top row shows the target region temperature for the (a), (b) 4 mm and (c), (d) 16 mm diameter trajectory. The bottom row shows the target region thermal dose for the (e), (f) 4 mm and (g), (h) 16 mm diameter trajectory. Images (a), (c), (e), and (g) show the temperature and thermal dose in the middle coronal slice, and images (b), (d), (f), and (h) show the corresponding thermal data in the simultaneously acquired sagittal slice. In the sagittal view, the transducer is at the left-hand side of the image.

Even though volumetric sonication methods are more efficient than point-by-point sonication, they nevertheless require a larger amount of total energy to be deposited per sonication event. This is a disadvantage of any volumetric ablation method where a larger volume is ablated than a single focal point. This increase in deposited energy also causes an increased near-field heating, which in turn increases the risk of related adverse events particularly for shallow targets close to the skin (47, 61, 65, 155). To reduce this risk and ensure the safety of the treatment, rapid multiplane MR thermometry with dedicated near field, beam path, and target region monitoring was performed simultaneously to the volumetric ablation in Publication **I**. The presented volumetric thermometry prevents undetected excessive temperature rise from occurring in the near field, and the online visualization and temporal resolution of the MR thermometry allows the operator to intervene should unexpected events occur. We have

since explored the usefulness of dedicated monitoring of the near field in more detail (156, 157).

The increased near-field temperature associated with volumetric sonication also mandates longer cooling periods between sonications in order to avoid excessive thermal build-up in the near field (47, 48, 61, 140, 152, 155, 157). Dissipation of the heat accumulated in the near field via diffusion is, moreover, slow due to small temperature gradients. However, the effect of perfusion may be more significant in cooling the skin and subcutaneous tissue layers than diffusion (47, 109). Consequently, the advantage in treatment time of volumetric ablation as compared to point-by-point ablation is less than indicated by the energy efficiency, even though the use of volumetric ablation will nevertheless reduce treatment time.

Insufficient cooling times are a serious concern, because too short delays between sonications will result in thermal build-up being accumulated over a period of several sonications that may eventually lead to adverse near-field events such as skin burns. However, the build-up may be reduced by minimizing the overlap of successive sonications, and by spreading the energy over a large near-field area by using large aperture transducers (47, 48, 157). This would in turn reduce the required cooling times, and subsequently also reduce treatment time.

2.4 Feedback controlled ablation (II)

A problem of HIFU therapy is that *in vivo* tissue parameters that govern tissue heating are typically unknown prior to treatment. These parameters may furthermore vary locally due to differences in tissue composition and architecture, as well as due to physiological differences. Temperature itself may, moreover, also affect the tissue parameters. It is hence very difficult to prior to the sonication predict the appropriate power level to apply.

One rudimentary approach for estimating the appropriate power level is to use a low power test sonication to “probe” the thermal response of the tissue (16, 75). Assuming a

linear relationship between the applied power and the temperature rise, one can obtain an estimate of the required therapeutic power based on the power used in the test sonication and the small temperature rise that is induced. The use of test sonications does improve the accuracy of the applied power, subsequently improving the reliability of the ablation outcome as compared to blindly choosing a power level. However, the scaling of the therapeutic power based on a test sonication assumes a linear relationship between the applied power and the temperature rise. This might be an adequate approximation for short sonications, but it is no longer accurate when diffusion and perfusion have time to affect the temperature rise (see Equation 2.6). Furthermore, the linear scaling of the power using a test sonication is only accurate for single point sonications, as the effect of diffusion is not accounted for. Test sonications were used in both Publications **I** and **II** to obtain an initial estimate of the power level, which was updated based on the results of the therapeutic ablations.

A more accurate and reliable approach is, however, to use a feedback loop to regulate the power based on the temperature rise seen in the MR temperature images (49, 50, 158-162). The basic feedback algorithms aim to control the temperature in a point by automatically adjusting the applied power based on the difference between the actual observed temperature and the target temperature curve (49, 159, 162). The target temperature is typically a smooth curve with a gradually increasing initial part followed by a plateau, which allows the feedback algorithm to accurately follow the target temperature evolution without inducing oscillations or overshoots. The actual control algorithm can advantageously be based on existing classical controllers such as a proportional-integral-derivative (PID) controller (49) or a linear quadratic regulator (LQR) (162). These control algorithms improve the stability and performance of the feedback control as compared to directly adjusting the power based on the difference between the current target temperature and current actual temperature. The control algorithms are, moreover, often based on the bioheat transfer equation (Equation 2.6) to further improve the controller performance (49, 159, 162).

Of significantly more interest than the single point temperature control discussed above is of course a simultaneous spatial and temporal temperature control. Feedback control algorithms may be applied to obtain a desired 2D temperature profile (98, 163) or even control the evolution of the temperature distribution in 3D (164). The main benefit provided by spatial controllers is that they may correct for spatial inhomogeneity and temporal variance in tissue thermal response, something which is not possible by other means. Early studies on spatio-temporal feedback control were limited by the use of single-element transducers, and feedback was consequently used to merely adjust the speed of the mechanical displacement (98) or in a more advanced approach use a PID controller to adjust both displacement speed and applied power (163). Phased arrays provide an immense improvement for spatio-temporal controllers as they allow any point within the range of electronic displacement to be sonicated at any time without restrictions on displacement speed. Consequently, phased-array transducers allow for rapid 3D spatio-temporal control where for example the sonication trajectory and the energy deposition in the trajectory points can be dynamically altered for every acquired MR temperature map (164). The controller could alternatively update the driving amplitude and phase of the different transducer elements, thereby dynamically altering the multifoci pattern, although this might not be desirable due to potential side lobes (165). Spatio-temporal control of prostate ablation with transurethral transducers has also been reported, although these methods differ significantly from the methods described above as the control for prostate ablation is on the mechanical rotation of the rod-shaped transducer and on the applied power (33, 166).

A disadvantage of the parametric control algorithms discussed above is that they are all sensitive to errors in the estimates of the tissue parameters as the controllers are based on the bioheat equation. If sufficiently large deviations occur in the estimate then the controller may begin to oscillate, or alternatively lag behind the target temperature (49, 162). This is less of a problem in spatio-temporal controllers than for single point controllers as errors in the a priori estimated parameters result in an altered sonication trajectory that inherently attempts to compensate for these estimation errors. A

disadvantage particular to the LQR algorithm is that it is computationally intensive and may thus not be compatible with real-time control (162).

A robust non-parametric feedback method was introduced in Publication **II**, specifically designed to improve the reproducibility and reliability of the volumetric sonication approach outlined in Publication **I**. The first step of this binary control algorithm is calculating the mean temperature from the subset of voxels in the MR temperature images corresponding to the currently sonicated circle at each acquired dynamic. The calculated mean temperature is compared to a predetermined limit, and if this limit is exceeded then the controller switches the sonication to the next circle. This continues until the final circle of the trajectory has reached its' mean temperature limit. The limits are obtained from off-line trajectory optimizations using Equation 2.6, and calculating the voxel sized mean temperatures at the time when the sonication circles of a trajectory are switched. Due to the non-parametric approach, this algorithm is computationally fast as well as inherently stable and oscillations that might be a problem for parametric control algorithms cannot occur (49, 162). The simple design moreover makes for a robust control, also in the presence of disturbances or unexpected thermal behavior due to abnormal thermal parameters. A further advantage is that the control is on time and not power, and that there is no need for a smooth ramping of a target temperature as is necessary for some parametric controllers (49, 163, 164). This enables the sonication to immediately begin at a high ablation power allowing for an efficient, rapid, and controlled ablation.

In Publication **II**, a total of 90 *in vivo* sonications were performed in a large animal model. The simple yet efficient feedback was shown to improve the reproducibility of the ablation by significantly reducing the standard deviation of the thermal lesion diameter by 48%, 86%, 79%, and 70% for the 4, 8, 12, and 16 mm diameter trajectories, respectively. Furthermore, when utilizing binary feedback, the resulting diameters of the 240 EM thermal dose volumes were much closer to the planned ablation size as given by the trajectory diameters. Another advantage was that the energy efficiency improved as a consequence of the feedback control, because the deposited energy was sufficient

but not excessive. This should, moreover, also reduce the cooling times as excessive energy deposition is avoided, thereby reducing near field accumulation. This should in turn further improve the treatment speed.

The binary feedback algorithm of Publication **II** does have some disadvantages that also arise due to the simple algorithm design. For example, the feedback cannot accurately account for spatial inhomogeneities occurring within the sonicated circle, and binary feedback may thus not be suitable for very inhomogeneous tissues. However, using the mean temperature within the sonicated circle does give some tolerance for spatial inhomogeneities. Consequently, the binary feedback did perform well in the vicinity of for example muscle fascia and the femoral vein in porcine thigh. The second main disadvantage is that the proposed feedback is not well-suited for accurately maintaining the temperature at a certain predefined level for an extended period of time, which is required for HIFU-activated local drug and gene delivery, as well as gene therapy (37, 43, 167, 168).

Despite of these disadvantages, the binary feedback algorithm nevertheless provides a robust control of the volumetric ablation that improves the reproducibility and reliability of the sonication outcome. The perhaps most important advantage as compared to other presented temperature regulating controllers is that the combination of binary feedback and volumetric concentric-circle ablation allows for a controlled, rapid, and energy efficient ablation of large volumes (162-164). The cost is a little less accuracy in the temperature control that may lead to under- or overheating at the border of the trajectory. Despite of this, the trajectory design and heat diffusion will ensure a thermal dose uniformly above the threshold of 240 EM within the trajectory borders. Further details on the design and results of the binary feedback algorithm can be found in Publication **II**.

Because the thermal dose determines the success of the ablation and not the temperature, a spatio-temporal control of the thermal dose would be preferable over a control of temperature. Although such controllers have been suggested and their

feasibility shown (169-173), most research on this topic is done using only simulations and there is little evidence of the functionality of the proposed controllers *in vivo*. Several of the presented approaches are also computationally intensive and may thus not be directly applicable to real-time control without simplifications to the control algorithms. Thermal dose controllers are nevertheless of substantial interest as they might be able to accurately control the therapeutic outcome also in the presence of spatial inhomogeneities, while applying the minimal energy to ablate the desired volume. It has recently also been shown that temperature or thermal dose control can be applied simultaneously to motion correction of MR-HIFU (51, 174), thereby allowing for a controlled MR-HIFU procedure in moving abdominal organs, such as the kidney or liver.

3 Magnetic resonance guidance of high-intensity focused ultrasound therapy

MRI provides a variety of different soft-tissue contrast mechanisms which reflect structural differences on both the macroscopical and microscopical level of the examined tissue (13). The modality is therefore well-suited to depict both healthy and pathological tissue, and to follow pathological processes in time (12, 175, 176). Consequently, MRI has in recent years taken an important role in the planning of surgical interventions, including non-invasive therapeutic approaches such as HIFU therapy (73, 75).

Due to its propagation properties and its specific absorption rate in biologic tissue, high-intensity focused ultrasound was singled out very early as an attractive candidate for noninvasive ablation of pathological tissue. However, the lack of suitable image guidance has prevented HIFU therapy from gaining widespread clinical acceptance until recently. MRI would seem ideal for providing this necessary guidance and the use of MRI for planning, monitoring, and post-treatment verification of the HIFU therapy was first suggested by Cline *et al.* in 1992 (11). Successful clinical use of MR guided HIFU therapy (MR-HIFU) has since been reported by several authors for different applications (16, 19, 23, 24, 27, 30, 75, 177).

This chapter presents an overview of the use of MRI for guidance of HIFU therapy. The use of MRI for therapy planning is briefly discussed as this constitutes the basis for any image guided therapy, including MR-HIFU. Therapy monitoring by MR thermometry is explained in some detail as this is the main advantage in using MRI as compared to other imaging modalities for guidance of HIFU therapy. This discussion also aims to explain the importance of appropriate motion compensation. The methods developed in this work for motion compensation of MR thermometry, navigators for through-plane motion compensation and for correction of the phase reference, are described in more detail in Publications **III** and **IV**. The combination of the in-plane 2D motion compensation with the through-plane motion compensation for 3D motion

compensation of thermometry is explained in more detail in Publication **V**. The combination of 3D motion compensated thermometry with beam steering of the focal point according to the observed 3D motion is in turn demonstrated to provide a fully 3D motion compensated MR-HIFU therapy in Publication **III**. Details on the development of the multiplane volumetric thermometry for improved monitoring coverage are in turn given in Publication **I**. A discussion on the use of MRI for verification of treatment outcome is also included as the ability of MRI to noninvasively assess tissue damage is another important aspect of this imaging modality facilitating guidance of the HIFU therapy.

3.1 Therapy planning

The excellent soft-tissue contrast provided by MRI makes this noninvasive imaging modality ideal for identifying and localizing the abnormal tissue to be targeted for any form of image guided therapy or treatment. High-resolution MR images can therefore be used for accurate planning of the MR-HIFU therapy if the relationship between the coordinate system of the planning images and the coordinate system of the ablation device, *i.e.* the transducer, is known. A graphical user interface to which these planning images are imported can then be used to create the MR-HIFU treatment plan by defining the position and angulation of the planned ablations, and examining the corresponding beam paths for acoustic barriers such as bone or air filled cavities. The efficiency and accuracy of this treatment planning can be improved by creating graphical overlays of the transducer and beam path on the planning images that are updated according to the actual transducer position. The time needed for transducer positioning can be reduced and planning efficiency further improved if the transducer positioning is software controlled. Such a setup as outlined above allows for visualizing and interactively adjusting the treatment plan and transducer position in reference to the target region anatomy, much in the same manner as in stereotactic surgery. An example of a treatment plan for a uterine fibroid patient created with a HIFU therapy planning software can be seen in Figure 3.1.

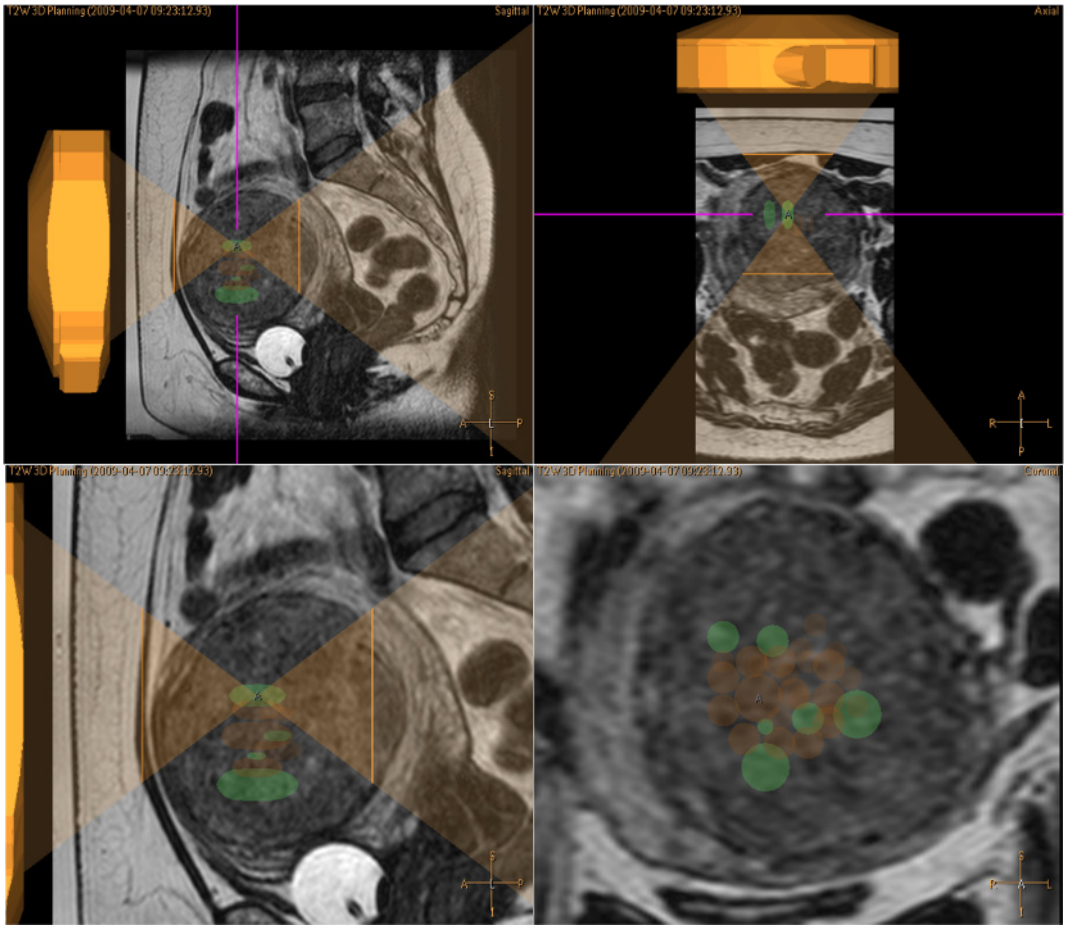

Figure 3.1: Sagittal (top left, zoomed bottom left), transverse (top right), and coronal (bottom right) images of a treatment plan for a uterine fibroid therapy. The fibroid to be treated corresponds to the round area of low signal in the middle of the images. The magenta line in the sagittal and transverse image in the top row represents the position of the coronal slice. The transducer is shown as a solid yellow overlay in the sagittal and transverse images. The semi-transparent cones in these images correspond to the ultrasound beam path. The semi-transparent green and red ellipsoid overlays represent the planned and performed ablations, respectively.

3.2 Treatment monitoring by magnetic resonance thermometry

The objective of any thermal therapy is to adequately treat the target while sparing adjacent healthy tissue. However, the heat diffusion, absorption, and perfusion of the tissue all vary as a function of tissue architecture, tissue composition, local physiological parameters and temperature. These parameters may furthermore change due to coagulation or necrosis. This makes predicting the temperature distribution exceedingly difficult. Continuous acquisition of temperature maps during treatment would therefore significantly improve the control of the thermal therapy outcome by estimating the temperature distribution near and at the target.

Several MR parameters such as relaxation constants, diffusion, and resonance frequency are temperature sensitive, because the motion, the interaction with macromolecules and the hydrogen bonds of the water-molecules change with temperature. By choosing the MR imaging sequence appropriately, continuous dynamic MR imaging can provide real-time information on the instantaneous *in vivo* temperature distribution in any imaging plane at a good spatial and temporal resolution. MR temperature imaging, or thermometry, has been suggested for monitoring hypothermia during cryosurgery (178) as well as for monitoring hyperthermia induced by laser (179), microwave (135), radio frequency (RF) (180, 181), and HIFU (14). The use of MR for thermometry was initially suggested by Parker *et al.* in 1983 (182), even though the temperature dependency of several MR parameters had already been established earlier (183-185). The method suggested by Parker was based on monitoring the longitudinal relaxation constant (T_1). Since then several other methods of thermometry have been suggested. The most widely used of these methods is thermometry based on the diffusion constant as first suggested by Le Bihan *et al.* (186), thermometry based on the proton resonance frequency (PRF) shift as suggested by Ishihara *et al.* (15), as well as thermometry based on the longitudinal relaxation constant.

PRF shift thermometry is by far the most widely used method of thermometry and is also the method used in Publications **I** – **V**. Because of this, discussion on other forms of thermometry is here omitted. Details on T_1-based and diffusion constant based

thermometry, as well as other methods of thermometry, can be found in the excellent reviews of Quesson *et al.* (187), Denis de Senneville *et al.* (188), and Rieke *et al.* (189).

3.2.1 Proton resonance frequency shift thermometry

PRF temperature dependence was first observed by Hindman in 1966 (184) when studying intramolecular forces and hydrogen bond formation between water molecules. A hydrogen nucleus is screened more efficiently from the main magnetic field by the electron cloud when part of a free water molecule, than when in a water molecule that is hydrogen bonded to another water molecule. This is because the hydrogen bonds distort the electronic configuration of the water molecules, thereby reducing the electronic screening. The fraction of water molecules that are hydrogen bonded depends on the temperature and an increase in temperature causes the hydrogen bonds to bend, stretch, and break, thus reducing the average time spent by the water molecules in a hydrogen-bonded state (184, 190, 191). This again increases the screening ($\sigma(T)$) seen by the hydrogen nuclei, which decreases the local magnetic field B_{loc} experienced by the nuclei according to

$$B_{\text{loc}} = \left(1 - \sigma\left(T\right)\right) B_0 = \left(1 + \delta\left(T\right)\right) B_0 , \tag{3.1}$$

where B_0 is the main magnetic field and $\delta\left(T\left(\bar{r}\right)\right)$ is the resulting chemical shift of the resonance frequency. This chemical shift, which is reduced by the increase in screening, has a temperature dependent part ($\delta_T\left(\bar{r}\right)$) but also a temperature independent part ($\delta_0(\bar{r})$) due to B_0 field inhomogeneities

$$\delta\left(T\right) = \delta_0 + \delta_T\left(T\right). \tag{3.2}$$

The temperature dependent part is linearly dependent on the temperature within the temperature range of interest for hyperthermia.

The decrease in the local magnetic field due to the change in the temperature dependent chemical shift will also lower the proton resonance frequency that is linearly dependent on the local magnetic field (192, 193). This temperature dependent shift in resonance frequency and thus also the chemical shift can be calculated using the phase information from the MR images of a gradient echo sequence (15)

$$\Phi(T) = \gamma\delta(T)T_{\mathrm{E}}B_0\,, \tag{3.3}$$

where Φ is the image phase, γ is the gyromagnetic ratio, and TE is the echo time of the sequence used. In order to measure the temperature dependent change in the chemical shift, the temperature independent contribution due to field inhomogeneities must be eliminated from Equation 3.3. This is typically accomplished by subtracting a reference phase image at a known baseline temperature from the phase image acquired at temperature *T*. This allows for calculating the change in temperature according to

$$\Delta T = T - T_{\mathrm{ref}} = \frac{\Phi(T) - \Phi(T_{\mathrm{ref}})}{\gamma\alpha_T T_{\mathrm{E}}B_0}, \tag{3.4}$$

where α_T is the temperature dependent water chemical shift in ppm per degree Celsius. The temperature sensitivity of the PRF method is very good as for a typical signal-to-noise ratio (SNR) of 40, field strength of 1.5 T, and echo time of 20 ms, the theoretical standard deviation is as low as 0.3 ºC (98). The inverse of the SNR is proportional to the temperature standard deviation, and a low SNR will therefore result in a high temperature uncertainty. It is important to note that the PRF technique is only capable of calculating relative temperature change, and not absolute temperature. The core body temperature is therefore typically used as the starting temperature to which the temperature variation maps are added in order to obtain absolute temperature maps.

Any gradient echo sequence can in principle be used for acquiring the phase information necessary for these temperature maps, as long as stimulated echoes can be

neglected. However, short repetition times and flip angles close to the Ernst angle are typically used, which makes efficient RF spoiling of the signal becomes crucial in order to avoid contaminating the phase information with stimulated echoes from previous excitations (138, 194). A spin echo sequence cannot be used for measuring the temperature induced phase change as the spins will be refocused at the time of image acquisition, leaving the phase image independent of chemical shift and thus also independent of temperature.

A very important advantage of the PRF method of thermometry is that the temperature dependent chemical shift α is nearly independent of tissue type and is also not affected by coagulation (195). Typical values of the temperature dependent water PRF shift vary between -0.009 and -0.01 ppm/ºC (196). However, the PRF shift is only tissue independent for aqueous tissues, as the temperature dependent PRF shift stems from changes in the hydrogen bonds that are absent in lipids (184). The PRF of lipid hydrogen is thus almost independent of temperature (197) and the presence of lipids in the phase images may therefore lead to errors in the PRF temperature images. Fortunately, fat suppression or spectral selective excitation can be used to image only water protons (198-200), thereby enabling accurate PRF thermometry in tissue where both fat and water protons are present (194).

There are, however, also some problems involved in PRF thermometry due to the assumptions made. The temperature dependency of the magnetic susceptibility causing the B_0 field inhomogeneities, $\delta_0(\bar{r})$, is commonly assumed to be negligible as in Equation 3.2, despite evidence to the contrary (197, 201, 202). For tissues with high water content such as muscle, the temperature induced change in susceptibility is about an order of a magnitude lower than that of the temperature induced chemical shift (197). This indicates that only small errors are made when omitting the influence of temperature dependent susceptibility in PRF thermometry of such tissues. The articles by De Poorter (197, 203) give more details on this subject.

The need of a reference phase also poses some problems as the phase is assumed only to be influenced by changes in temperature. However, the external magnetic field of currently available MR scanners will drift in time when the gradients are intensively utilized (204), resulting in phase drift and an apparent temperature change. This phase drift can be compensated by subtracting the average phase change seen in either an external phantom in thermal equilibrium or an internal non-heated region. If the phase drift varies in space, an improved compensation can be obtained by fitting a polynomial curve to the spatial distribution of the phase drift in the non-heated reference region and subtracting this fitted phase from the acquired phase images. An alternative approach to PRF thermometry is to not use a phase reference image at all, but instead use a polynomial fit of the phase (205) or complex data (206) from the non-heated area to estimate the background phase in the heated area. The background phase, which is the estimated phase in the heated area had it not been heated, is then used as the reference phase. This so called referenceless thermometry does therefore not need a phase drift correction, as the temporal field drift is already included in the non-heated area from which the reference phase is estimated. A disadvantage of this method is, however, that a high SNR is required and the heating needs to be confined to a small well-defined area for the polynomial fitting of the phase reference to be reliable.

Organ motion is, nevertheless, the most prevalent problem for PRF thermometry. Several abdominal organs are prime candidates for MR-HIFU but are subject to both rigid and non-rigid motion during the respiratory cycle. Not only does this motion need to be compensated and the images aligned with the reference image to avoid artifacts in the temperature images, but a correct reference phase also needs to be used since the local magnetic field experienced by the organ will vary as the organ moves through the inhomogeneous magnetic field inside the body. Removal of non-temperature related phase perturbations is thus imperative for accurate PRF thermometry of moving objects. This is the topic of the following sections.

3.2.2 Motion artifacts in proton resonance frequency shift thermometry

Motion generally causes blurring in MR images, but in MR thermometry this blurring may also induce errors in the calculated temperatures (207). PRF thermometry of moving organs will furthermore result in an artifactual temperature in any part of the currently acquired image that is misaligned with the reference image (56, 207). Motion artifacts in MR thermometry are commonly coarsely divided into two categories, intrascan and interscan motion artifacts, based on the timescale of the motion as compared to the imaging.

Intrascan motion artifacts are caused by motion during the acquisition of an MR image. Intrascan motion typically results in blurred low-quality MR images with ghosting. These artifacts can be reduced by gated acquisition schemes, which severely limit the achievable temporal resolution (188), or by accelerating the imaging sequence in which case a compromise between SNR and the speed of acquisition has to be made. For respiratory motion, acquisition times below 400 ms have been found sufficient to avoid intrascan motion (56). In order to obtain a short acquisition time, rapid acquisition schemes such as gradient-echo echo planar imaging (EPI) are often used for MR thermometry (71, 98, 208-210). This imaging technique can be combined with sensitivity encoding (SENSE) (211, 212), temporally adaptive sensitivity encoding (TSENSE) (213, 214), or other similar parallel imaging or k-space inheriting approaches to further speed up the acquisition. However, EPI is very sensitive to field inhomogeneities and prone to geometric distortions. These distortions, which are more severe for long EPI readout trains, may obscure the anatomical and temperature information (215). If prominent, the geometrical distortions need to be corrected in real-time in order to enable accurate real-time thermometry (216).

Interscan motion, on the other hand, refers to motion that occurs between the acquisition of consecutive images. If there is only interscan motion in the data set, then good quality MR images are obtained of the moving organs but the target region in successive dynamical images is not aligned. The subsequent misalignment of the currently acquired image and the reference image will in turn lead to errors in the temperature images

obtained by PRF thermometry (see Equation 3.4). These temperature errors can be reduced by using image registration techniques to estimate and correct for any 2D organ motion that might be present within the acquired imaging plane (56, 217).

3.2.3 Correction of interscan motion using image registration

The objective of image registration is to relate the coordinate of each part of the tissue in the current image to the corresponding part in the reference image (54). Although any established image registration technique may in principle be used, many are limited to correction of rigid motion which poorly represents the motion of such abdominal organs as the liver. Furthermore, in order to provide real-time non-rigid motion correction, the motion correction has to be done during the acquisition of the following dynamic image of that slice. Since the imaging time of a single slice acquired with a single-shot EPI sequence can be as short as 70 ms when using a typical matrix of 128×128, the requirement of real-time motion correction further limits the amount of suitable algorithms. Of the different image registration techniques, methods based on image intensity have been shown in the past to provide a sub-voxel precision and a robust behavior to MRI-image artifact (188). Furthermore, these methods can be implemented to allow for automatic motion correction, which requires no user interaction, and may in addition utilize the full image content instead of merely anatomical landmarks (54, 188).

The efficiency with which image intensity based methods are capable of estimating motion correctly depends largely on the nature of the transformation needed (51, 218). Global motion between two images may for example be obtained in both a robust and computationally efficient manner by estimating the affine transformation that best describes the motion (52). Even though affine transformation could be used for correcting for rigid organ motion occurring within the abdomen, it cannot accurately depict the complex non-rigid motion of for example the liver. Motion estimation algorithms based on the optical flow are, on the other hand, suitable for accurately estimating complex non-rigid motions, although at the expense of being more sensitive to disturbances and computationally more intensive than affine transformations (219). Optical-flow based algorithms estimate motion between images by computing the pixel-

by-pixel displacement based on the flow of voxel intensity between the images, relying heavily on the assumption that the image intensity is conserved and that adjacent voxels are subject to a similar displacement (53, 56). The optical flow algorithm of Cornelius & Kanade (220), that only assumes a local conservation of intensity, has been suggested for estimation of local organ displacement for motion compensation of MR thermometry (218). In the presence of large amplitude non-rigid motion, a proven approach is to first estimate a global affine transformation and use the result of this estimate as the starting point of the optical flow estimation algorithm (51, 218). The estimated motion may then be used to realign both the current magnitude and phase image with the corresponding reference images, thereby reducing interscan motion.

3.2.4 Motion correction using external devices

Respiratory gating is a simple method that can be used to reduce interscan motion by ensuring that the images are taken at the same position of the respiratory cycle (221). In this widely used technique (58, 208, 212, 222, 223), the respiratory state is estimated with an external pressure sensor. This sensor may for example be a pressure cushion fastened around the chest that measures the expansion and contraction of the chest wall during respiration (212, 221), or a sensor that measures the airway pressure (222). The acquisition of all MR images is timed to the same stage in the respiratory cycle using the output of this sensor. Mid-to-end exhalation is usually chosen for acquisition since the abdominal motion is less in this stage of the respiration cycle than during inhalation (58, 222). Respiratory gating also reduces intrascan motion by acquiring the images, particularly the k-space center, during the part of the expiration phase with least motion (222). However, respiratory gating might fail if the breathing pattern is irregular, resulting in blurred images with motion artifacts as well as errors in the temperature maps due to interscan motion (212). Moreover, the diaphragm position does not fully correlate with respiratory sensor signal, leaving some residual interscan motion of both the diaphragm and the targeted tissue despite the use of respiratory gating (58). The final and perhaps most significant disadvantage of using respiratory gating is the very poor temporal resolution that is determined by the duration of the respiratory cycle (~5 s for humans) (188). While the cryoprobe, laser-applicator, RF-electrode, and microwave-

electrode commonly used for thermotherapy are all inserted in the target tissue and thus move with the respiratory motion, the focus of the externally positioned HIFU transducer does not. In order to avoid heating tissue not intended for ablation HIFU can thus only be applied during imaging at mid-to-end exhalation when little motion occurs, which in turn leads to a poor duty cycle and inefficient heating.

Another alternative is to use ultrasound imaging to estimate the organ motion during HIFU ablation (224). The displacement, which can only be obtained in a point, may be used for aligning the MR images, and thus reduce the MR thermometry interscan motion. However, it has to be assumed that the motion of the monitored point corresponds to the motion of the entire region of interest, which is an acceptable assumption only in case of rigid motion. Another disadvantage is that the speed of sound used to estimate the displacement is temperature dependent, and a temperature elevation anywhere between the transducer and the monitored point will thus cause an error in the displacement estimate. Consequently, the motion has to be monitored in an unheated point at a distance from the heated area, which might lead to inaccurate motion estimates for HIFU ablation of organs subject to non-rigid motion such as the liver. Moreover, this restriction might also be problematic for organs undergoing rigid motion if larger volumes are heated per sonication event, because the monitored point might have to be located outside of the treated organ.

3.2.5 Motion correction using navigators (III)

Navigator echoes (225) acquired with only a single (226) or a few phase-encodings (58) can be used for estimating and correcting in-plane motion during hyperthermia. These navigator echoes can either be acquired using a separate interleaved imaging sequence (225), or as part of the imaging sequence by acquiring the echoes immediately after the slice-selective RF excitation (58, 226). The latter approach is typically preferred since no extra excitations are needed and the thermometry temporal resolution is thus not notably reduced. An inverse Fourier transform of acquired navigator echo gives a signal profile with high spatial resolution along the frequency encoding direction and a low or very low spatial resolution in the phase-encoding direction depending on the amount of

phase-encodings acquired (see Figure 3.2). In fact, if only a single phase-encoding is acquired then the navigator profile is a projection of the MR signal along the phase-encoding direction as seen in Figure 3.2 d (225, 226). The reason for keeping the number of phase-encodings low is that the acquisition time increases linearly with the amount of phase-encodings and the temporal resolution of the navigator echo would subsequently be reduced. If the temporal resolution becomes too poor, the position estimates of the monitored structure will be delayed and thus not be representative of the actual motion. If significant motion occurs during the acquisition of the navigator echo, the navigator profile will furthermore be blurred due to this intrascan motion. Despite the low spatial resolution of the navigator echo profiles in the phase-encoding direction, the location of the upper part of the diaphragm can typically be discerned. This can also be seen in Figure 3.2 where the upper part of the diaphragm can be distinguished for all images, including the projection image.

The navigator echoes can be used to detect motion by comparing the obtained navigator profile to a reference profile, which is typically taken as the profile acquired by the first navigator. The displacement between the currently obtained profile and the reference is commonly quantified using edge-detection (227), cross-correlation (225, 228) or a least-

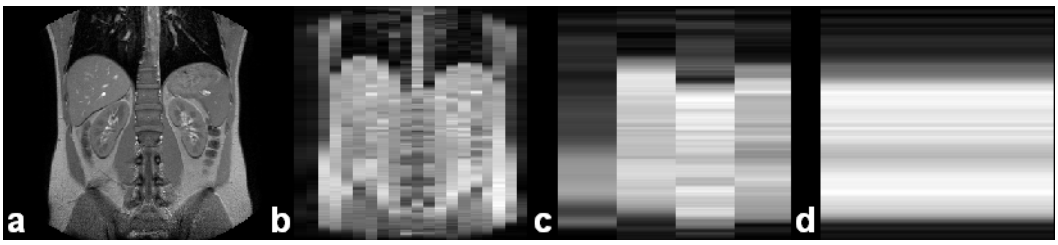

Figure 3.2: MR image of the abdomen during breath-hold (a), and anisotropic reconstructions of the same image with reduced resolution in the left-right phase-encoding direction (b – d). Acquisition time for the entire image (a) with 288 phase-encodings was 10 s. The acquisition time for the lower resolution images would have been 700 ms, 140 ms, and 35 ms, for the image with (b) 20 phase-encodings, (c) 4 phase-encodings, and (d) 1 phase-encoding, respectively. The image was acquired with an FFE sequence with TR = 35 ms, TE = 5 ms, slice thickness 7 mm, FOV 400 × 400 mm^2, and matrix 288 × 288. Informed consent was obtained from the volunteer prior to acquisition of the images.

squares approach (228). Edge-detection is the least preferred of the three methods as it requires a well-defined edge and high SNR, which are not always available (228). The cross-correlation algorithm calculates the displacement by spatially shifting the current navigator profile with respect to the reference profile in order to maximize the cross-correlation between the two navigator profiles. The displacement is determined as the spatial shift that corresponds to the maximum correlation. The least-squares method similarly shifts the currently obtained navigator profile with respect to the reference, but the displacement calculated by this algorithm is determined as the spatial shift that minimizes the variance between the two profiles. Of the cross-correlation and the least-squares method, the least-squares algorithm tends to be more robust in the presence of poor SNR or severe motion that might distort the navigator profile (228).

The obtained displacement can either be used for motion correction (225) or for gating (229). Provided the navigators are acquired at a sufficient temporal resolution, the echoes can be used to correct for both inter- and intrascan motion by phase correcting the acquired k-space data (58, 225, 226). If gating is desired then the use of navigator echoes is typically more accurate than respiratory gating via external sensors because the navigators may monitor the diaphragm position directly instead of via secondary effects such as the expansion and contraction of the chest (58). However, motion correction is generally preferred over gating as it allows for continuous imaging with little motion artifacts throughout the respiratory cycle and therefore does not notably affect the temporal resolution (225).

The major disadvantage of these navigator echoes is the poor spatial resolution in the phase-encoding direction, which makes it impossible to discern a separate moving structure. Movement seen in the projection image of Figure 3.2 d cannot for example be used to exactly correct the rigid motion of the right kidney as it is simply not possible to locate the position of this organ within the navigator profile. The navigator echoes are therefore restricted to in-plane correction of bulk motion.

A solution to this problem is offered by 2D RF pulses that can be used to excite narrow cylinders of magnetization (230, 231) as demonstrated in Figure 3.3. Such pencil-beam excitations may be used as navigators by applying a readout gradient along the main axis of the pencil beam (232). The resulting navigator profile is a perpendicular projection of all excited magnetization onto the beam axis. Because the excited pencil beam is spatially well-defined and contained within a narrow cylinder (typical diameter approximately 3 cm (233)), pencil-beam navigators may accurately monitor the motion of separate abdominal structures without using multiple phase-encodings. However, in the same manner as navigator echoes are restricted to estimation of motion within the imaging plane, pencil-beam navigators can only monitor the motion along the direction of the pencil-beam main axis. The acquisition of the pencil-beam navigator can easily be interleaved with that of the imaging sequence, and the pulse duration and acquisition of less than 6 ms (233) and about 8 ms (228), respectively, do not substantially reduce the temporal resolution of the imaging sequence. Since the pencil-beam orientation can be chosen freely it can be used for estimating through-plane motion, something which is not possible with conventional navigator echoes without introducing a separate imaging sequence with an intersecting slice-plane. Online analysis of the through-plane displacement obtained with the pencil-beam navigator may be used to update the excitation frequency of the imaging sequence RF pulses during scanning, thereby enabling slice tracking where the imaging plane moves with the monitored mobile structure (55). For segmented acquisitions, the pencil-beam navigators may thus be used to correct for both interscan as well as intrascan motion that occurs along the direction of the pencil beam. However, a problem of the pencil-beam navigators is that the off-resonance effects of the 2D RF pulses are quite complex. The excited cylinder of magnetization is only of the intended diameter in the small segment of the pencil beam from where the excitation frequency is determined (233). Outside of this region, off-resonance effects broaden and blur the circular cross-sections of the pencil beam as can also be seen in Figure 3.3 d. This is in part why only the middle of this pencil-beam navigator profile is typically used for determining the displacement (55). More details on pencil-beam navigators can be found in the excellent article by Nehrke *et al.* (233) on the optimization of spiral excitation 2D RF pulses for navigator purposes.

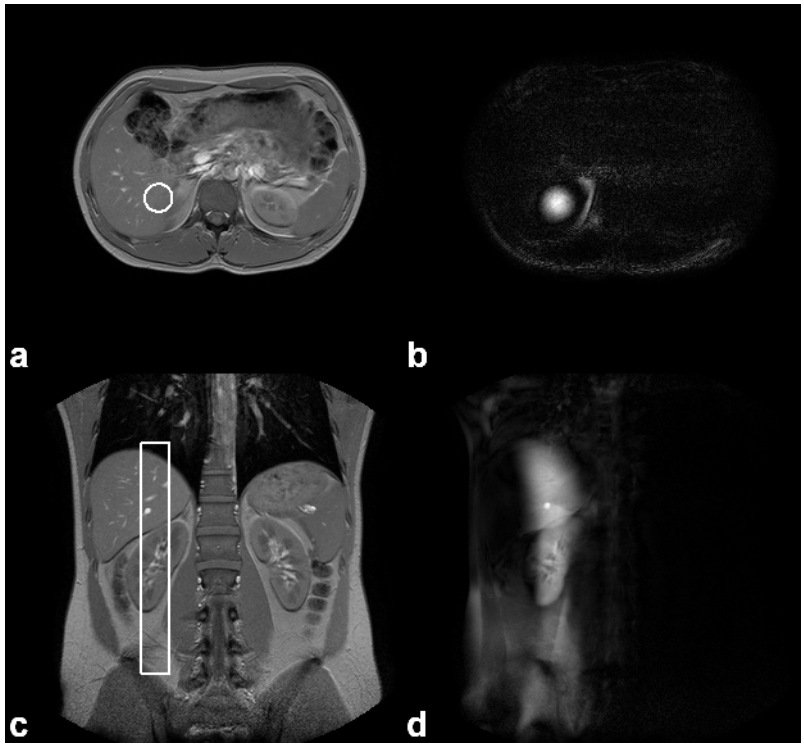

Figure 3.3: Positioning of the pencil beam in the transverse (a) and coronal plane (c) shown by the white overlay and the resulting excited magnetization as seen perpendicularly (b) and along (d) the pencil-beam axis. The images are taken from the same volunteer as in Figure 3.2 using the same FOV and matrix size. The pencil-beam excitation images were acquired by replacing the conventional 1D RF pulse with a spiral-encoded 2D RF pulse. Turbo spin echo (TSE) readout was used in the transverse view of the excited pencil beam (b) with a slice thickness of 20 mm. Fast field echo (FFE) readout was used in the coronal view of the excited pencil beam (d), causing the image to be a projection of the excited signal in the slice excitation direction (anterior-posterior). The diameter of the pencil beam was 30 mm.

For MR-HIFU, the exact estimation of the target organ motion is imperative, while all other motion estimation is of secondary interest. In order to avoid errors, it is desirable to track the motion of the target tissue directly instead of estimating the target motion via the monitored diaphragm motion as is typically done with conventional pencil-beam navigators (55, 228, 233). The main utility of the pencil-beam navigator is to assess through-plane motion for slice tracking purposes, which for the direct tracking of organ motion means that the pencil beam will need to intersect the imaging slice. This will cause a small area where the pencil beam disturbs the phase of the imaging plane or at

the very least reduces the SNR due to partial saturation. The potential phase perturbation might even induce temperature artifacts, whereas the more likely partial saturation will increase the temperature uncertainty. The intersection of the imaging slice and the pencil beam will also cause a partial saturation of the navigator profile that can in turn cause problems for the slice tracking. The partial saturation of the profile might cause the navigator to track the position of the previously excited imaging plane instead of the organ motion. The induced partial saturation can become particularly problematic for the navigator-based motion estimation if it is the dominant feature within the navigator profile as is the case in Figure 3.4. Since the fat is typically discarded from thermometry in order to avoid erroneous temperature readings, a fat-selective pencil-beam navigator would avoid utilizing the same magnetization as the imaging slice. A fat-selective navigator would thus avoid inducing possible phase perturbations and reducing the thermometry accuracy at the cross-section with the imaging plane. Similarly, the water-selective imaging plane will not cause a partial saturation of the fat-selective navigator profile, thereby allowing for undisturbed estimation and compensation of the actual organ motion. Furthermore, the conventional pencil beam also has a mainly proton density weighted signal resulting in a poor contrast between most abdominal organs and thus also a poor tracking performance. A fat-selective pencil beam avoids this issue as it provides a much improved contrast within the navigator profile as most abdominal organs are surrounded by a sheath of fat. This should further improve the tracking performance. Moreover, if the target region is within the pencil beam then the increase in T_1 caused by the heating results in a decrease in signal that might cause problems for the motion estimation algorithm (226). This is less of a problem for the fat-selective pencil beam than for the traditional non-selective pencil beam as the target tissue is seldom adipose and changes in the aqueous target tissue T_1 do not affect the lipid signal of the fat-selective pencil beam.

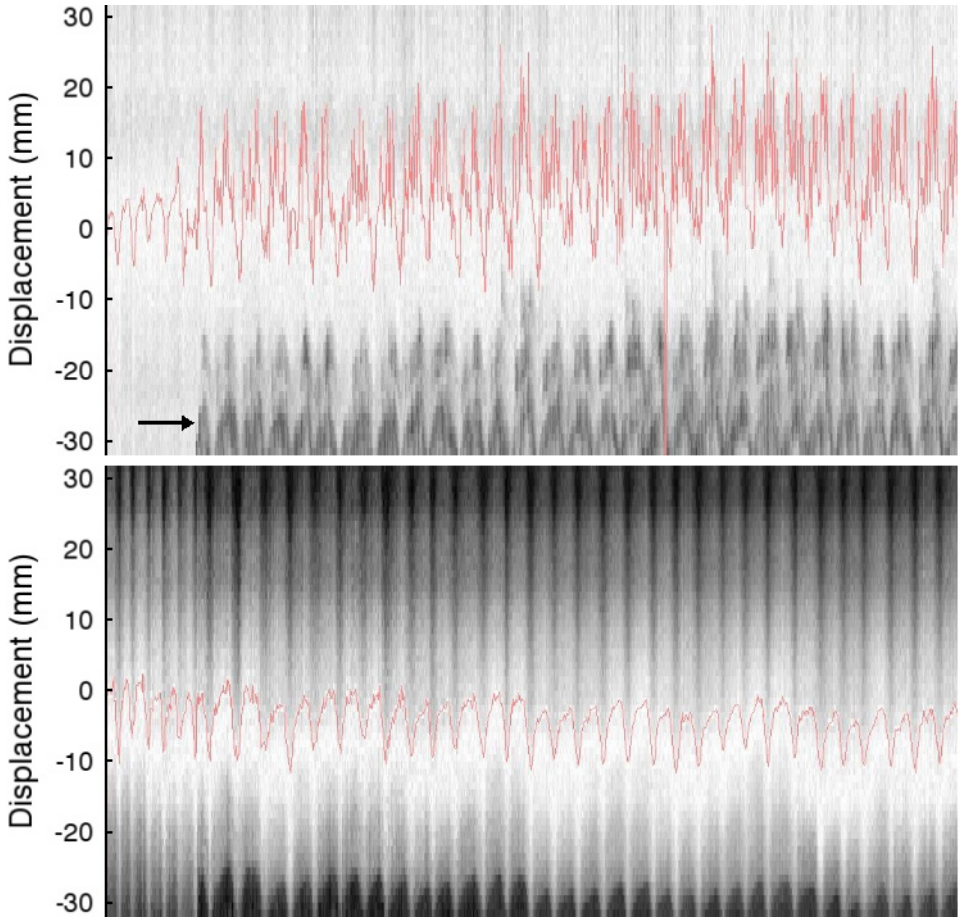

Figure 3.4: Navigator profiles of a kidney acquired with the conventional navigator (top panel) and the fat-selective navigator (bottom panel) during free breathing. The navigator profiles are plotted along the y-axis with the dynamic scan number increasing towards the right. The displacement estimated from the navigator profiles is overlaid in red. The navigators were placed in the feet-head direction across the right kidney of a volunteer in a similar fashion as shown in Figure 3.3. Informed consent was obtained from the volunteer prior to the experiment. During the learning phase of the navigator, no images were acquired and both the conventional navigator and the fat-selective navigator depict the organ motion. Once the water-selective MR thermometry begins one can clearly see an alteration in the profile of the conventional navigator, indicated by the black arrow in the top panel. The conventional navigator consequently fails to track the motion of the organ during imaging (seen as an erratic displacement estimate, red line) due to the interference of the imaging plane, whereas the fat-selective navigator estimates the organ motion correctly throughout the imaging experiment.

In Publication **III**, such a fat-selective pencil-beam navigator as described above was developed. In this publication, a binomial pulse train (200, 234) of spiral 2D RF pulses (233) was used to obtain a spectral and 2D spatial selective pencil-beam excitation. The problem of off-resonance effects becomes even more complex when adding spectral selectivity via a binomial pulse-train to the already complex off-resonance behavior of the 2D RF pulses. However, the analysis conducted in Publication **III** showed that the spectral-spatial response of the proposed binomial 2D RF pulse train was equal to the spectral response of the binomial weighting modulated by the spectral-spatial response of the 2D RF pulse. The slice tracking performance of the fat-selective pencil-beam navigator was compared to the traditional pencil-beam navigator when tracking the motion of a human kidney during free breathing. The traditional pencil-beam navigator often failed to register the motion correctly due to the poor contrast, whereas the spectral-selective pencil beam correctly estimated the motion during the entire *in vivo* tracking experiment. However, several of the misregistrations could probably have been reduced by introducing some filtering such as for example a Kalman filter (235). Informed consent was obtained from the volunteer prior to the slice tracking experiment. Publication **III** contains more details on the design of the spectral-selective pencil-beam navigator.

3.2.6 Baseline phase reference correction (IV)

In order to remove non-temperature dependent phase-fluctuations, it is not enough to merely align the current image with the reference image. This is because the image phase of any moving tissue, *e.g.* an abdominal organ, varies even when no heat is applied due to inhomogeneities in the local magnetic field. These inhomogeneities arise because the magnetic field of MRI systems is not perfectly homogeneous, and because the human body is a fairly complex and unsymmetrical composition of diamagnetic tissue with different magnetic susceptibilities. Any displacement of the observed tissue in such an environment will lead to phase changes arising from both the experienced variations of the imperfect external magnetic field and from changes in the inhomogeneous diamagnetic surroundings (201, 202). The latter effect is particularly strong for the case of respiratory motion, where the expansion and contraction of the

lungs and thorax will induce large variations in the local magnetic field (236, 237). If the reference phase image is not chosen appropriately, these magnetic field variations will cause an apparent false temperature according to (Publication **IV)**

$$\Delta T_{\text{app}}(t) \approx \Delta T_{\text{real}}(t) + \frac{\Delta B(t) - \Delta B_{\text{ref}}}{\alpha_T B_0}, \tag{3.5}$$

where $\Delta B(t)$ and ΔB_{ref} correspond to the deviation from B_0 in the currently acquired image and in the reference image, respectively. Although a precise knowledge of the susceptibility distribution would in principle allow modeling of the magnetic field and its' variations (238), accurate modeling is difficult *in vivo* especially under real-time conditions. Other approaches are therefore typically preferred to correct for the temperature artifacts induced by the local changes in the magnetic field.

Respiratory gating, as mentioned above, may be used to correct for interscan motion by acquiring the images at the same phase of the respiratory cycle. Provided the breathing is smooth and regular (212), the respiratory gating will also ensure that the targeted organ is in the same position and that the local magnetic field experienced by the targeted organ is the same for all acquired dynamic images (212, 222). Although this is a simple and effective method of ensuring the use of the correct baseline phase, respiratory gating prevents a continuous data acquisition and leads to a poor temporal resolution of the acquisition (188). Moreover, because HIFU sonication may only be performed during mid-to-end exhalation when little motion occurs, respiratory gating will also indirectly lead to an inefficient heating.

An alternative method is to renew the reference phase image in case of movement as detected by for example navigator echoes (226). Assuming motion initially occurs between times $t_{(n\text{-}1)}$ and t_n, then the local magnetic field has remained the same for all $t_i \leq t_{(n\text{-}1)}$ and will also be the same for all $t_i \geq t_n$ until motion occurs once more. However, the phase difference between the $t_{(n\text{-}1)}$ and t_n will result in a false apparent temperature due to changes in the local magnetic field induced by the motion. This false apparent

temperature change can be eliminated by taking a new baseline after the motion occurred and calculating the temperature according to

$$\Delta T_i = \Delta T_{n-1} + \frac{\Phi(T_i) - \Phi(T_n)}{\gamma \alpha_T T_E B_0}, \tag{3.6}$$

where $\Delta T_{n\text{-}1}$ is the motion corrected temperature calculated from the phase evolution up to $t_{(n\text{-}1)}$. The phase difference between $t_{(n\text{-}1)}$ and t_n is discarded from the temperature calculation. While this is an adequate method for correction of non-temperature dependent phase changes due to infrequent, *e.g.* accidental motion, it cannot be applied in the presence of continuous motion as most phase images would have to be discarded due to motion.

A more flexible method for correction of respiratory induced periodic phase-fluctuations is the multi-baseline approach (56). There are two stages to this approach: learning and intervention. During the learning stage, the acquired magnitude and phase images are stored in a look-up-table based on the current respiratory state as measured by a sensor. This sensor may for example be a pressure sensor, image data (51, 58, 209, 239), or a pencil-beam navigator (Publication **IV**). The use of navigators may provide an advantage over traditional image-data-based methods as navigators allow for freely estimating the motion of any structure, including out-of-plane structures that may better depict the respiratory cycle than available in-plane areas. Separate look-up-tables are needed for inhalation and exhalation as respiratory induced organ motion, diaphragm position, and thorax expansion are not in-phase and may differ between expiration and inspiration (240). Then during intervention, the current respiratory state as detected by the respiratory sensor is used to identify the appropriate reference image from the look-up-table for the currently acquired image. Due to the periodicity of the respiratory motion, it can be assumed that the phase images in the look-up-table represent the possible respiratory states and corresponding local magnetic environments that can be encountered during intervention. If the look-up-table covers the respiratory cycle sufficiently well, an appropriate reference phase will thus always be found during

intervention. However, since the look-up-table cannot be infinitely dense, an exact match to the respiratory state obtained during intervention is seldom found. The nearest neighbor is then typically chosen (58), even though this causes discretization errors in the reference phase correction. An alternative is to apply a model based voxel-by-voxel correction on the look-up-table data (218), where the model may for example be linear interpolation. An example of the respiratory induced apparent temperature variations and the corrected temperatures obtained using the look-up-table-based multi-baseline approach is given in Figure 3.5. Changes in the magnetic field due to breathing induce clearly visible fluctuations in the apparent temperature, although the magnitude images remain stable during the respiratory cycle. These fluctuations are removed by the look-up-table-based correction. The further improvement provided by the model correction mainly reduces the spatial temperature variation in the fat appearing dark in the upper right part of the breast images. The relatively small improvement is mostly a result of the rather long training phase of 60 dynamic images. The mean temperature standard deviation in the non-fatty tissue, appearing bright in Figure 3.5, was 1.14 ºC with only look-up-table correction and 0.93 ºC when also applying model-based correction.

In Publication **IV**, a look-up-table-based multi-baseline approach was used for correcting respiration-induced MR thermometry artifacts in the breast of five healthy female volunteers under free breathing (of which the data from one patient is shown in Figure 3.5). Informed consent was obtained prior to the experiments. The indexing and retrieval from the look-up-table was performed using a pencil-beam navigator placed directly across the diaphragm for accurate estimation of the breathing cycle. The use of a look-up-table was seen to substantially reduce the artifactual temperature fluctuations. The additional use of a model-based correction further improved thermometry accuracy, particularly for sparsely populated look-up-tables where the influence of discretization is greater. The model-based correction used a linear voxel-by-voxel interpolation of the look-up-table data for displacements between the entries in the look-up-table. Publication **IV** gives more details on the possible sources of respiratory induced temperature artifacts and their correction with a look-up-table-based model-corrected multi-baseline approach.

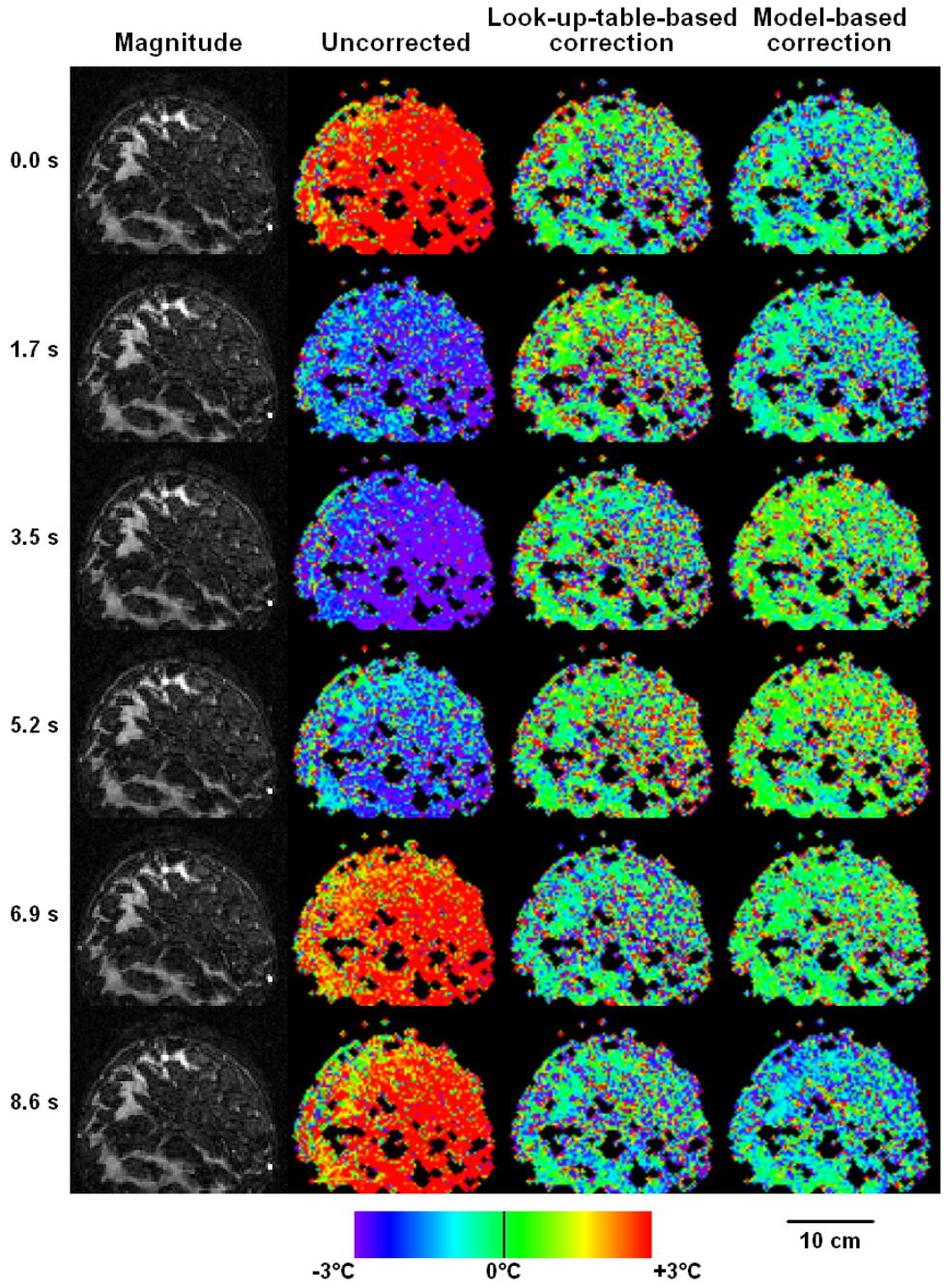

Figure 3.5: Coronal magnitude images (first column) and temperature images of a human breast with no heat applied at different stages of the respiratory cycle. Uncorrected temperature images (second column), basic look-up-table multi-baseline corrected temperature images (third column) and model-corrected look-up-table multi-baseline corrected temperature images (fourth column) are shown. The duration of the respiratory cycle was approximately 8.6 s. All temperature images were corrected for baseline drift. 60 dynamic images were used for the learning phase. The fat was suppressed from the images using a 121-binomial water-selective excitation. The data is the same as for Figure 1, volunteer 1 in Publication **IV**.

3.2.7 Compensation of 3D motion for proton resonance frequency shift thermometry (V)

MR thermometry in the abdominal region is challenging under free breathing due to the continuous and complex 3D motion of the abdominal organs and the subsequent variation of the MR image phase (51, 56). These non-temperature dependent variations must be corrected in real-time to enable accurate monitoring of the HIFU therapy. This requires compensation of the 3D motion to reduce artifacts due to interscan motion in addition to the use of a correct reference phase. Furthermore, respiration also causes motion of the target relative to the transducer, which if not corrected or accounted for will cause unintended heating of healthy tissue surrounding the target.

One approach is to align the imaging plane to the principal axes of organ motion, and thus reduce the problem of 3D motion compensation to 2D (241). The remaining 2D motion can then be compensated using the image registration methods discussed in previous sections. However, some residual through-plane motion will be present and the outlined strategy would moreover restrict the free placement of the imaging plane to that of the organ motion, even though a different imaging plane might be preferable for diagnostic or therapeutic purposes. For example in MR-HIFU, the imaging planes used for thermometry are typically placed along or perpendicularly to the beam axis of the transducer as the temperature elevation will be symmetric around the beam axis in homogeneous tissue.

An alternative is to use image registration, although it is very difficult to compensate for 3D motion using only classical image registration techniques. This is mainly because image registration based motion compensation requires relatively high and near isotropic spatial resolution to provide accurate motion estimation. One method would be to use two intersecting imaging planes centered on the region of interest, but this approach would lead to partial saturation and slightly reduced temperature accuracy exactly at the target. The position of the imaging planes would also have to be updated in real-time to follow the motion of the target. Another approach is to cover the entire 3D volume of interest with either 3D imaging or parallel 2D slices. The acquisition of

such an isotropic high-resolution 3D volume has to be split over several respiratory cycles due to technical limitations and the poor SNR of fast imaging methods. The obtained image volume can then be used for 3D motion compensation using only image registration (242). However, as much as 10 respiratory cycles (~50 s) might be required to acquire the images covering the entire volume of interest. Although this method can successfully compensate for through-plane rigid and in-plane non-rigid motion, it is incompatible with real-time motion compensated thermometry due to the very poor temporal resolution.

Image registration techniques based on image intensity do, however, provide excellent compensation of complex and non-rigid in-plane interscan motion (51, 217, 218). Compensation of 3D interscan motion would therefore only require some additional means for accurate compensation of through-plane motion. Respiratory gating can be used to this end, but the abdominal organ position does not fully correlate with the respiratory cycle as estimated with this technique (58). Furthermore, both the temporal resolution as well as HIFU duty cycle would be poor.

A far more accurate and efficient approach is to use pencil-beam navigators to assess through-plane motion and dynamically adapt the slice position accordingly. The through-plane displacement obtained by the pencil-beam navigator can be used to update the imaging position of the MR imaging sequence (55), thereby providing continuous thermometry of the moving organ rather than only during mid-to-end exhalation as for respiratory gating. However, it is desirable to track the motion of the target tissue directly in order to obtain an as accurate as possible compensation of the through-plane motion. To this aim it is preferable to use a fat-selective navigator as described in Section 3.2.5. The navigator, whether fat-selective or not, is nevertheless only capable of assessing the rigid motion along the pencil-beam axis. However, this disadvantage is mostly negligible as the fat-selective navigator can be placed directly on or in the immediate vicinity of the intended HIFU focus position without disturbing thermometry. Ultrasound motion estimation in a point at a distance from the heated location could alternatively be used to correct for through-plane motion, although the

motion has to be assumed rigid throughout the region of interest as well as where the monitored point is placed (224).

In Publication **V**, real-time compensation of 3D interscan motion was achieved by combining image registration for in-plane motion compensation with a fat-selective pencil-beam navigator for through-plane motion compensation. In-plane motion was compensated using 2D optical-flow based estimation of local non-rigid motion (218). Local magnetic field variations due to respiratory motion were in turn corrected using a look-up-table-based multi-baseline approach (56). The appropriate reference phase image was retrieved based on the displacement of the pencil-beam navigator profile. The feasibility and precision of the suggested method for real-time 3D motion compensation was shown with a phantom RF-heating experiment and by imaging the kidney of a volunteer during free breathing. The update frequency of the water-selective MR images was 10 images per second and image processing induced a latency of only 55 ms (post echo-time), fully compatible with real-time motion compensation requirements. Large artifactual phase- and temperature-variations due to motion were proven to be completely removed by the proposed correction and the accuracy of the motion compensated thermometry was within the limits imposed by the SNR. Figure 3.6 shows the reduction in temperature variation within the kidney of a volunteer as a result of applying the outlined correction strategy. Informed consent was obtained from the volunteer prior to the experiment.

A completely different approach to remove motion artifacts from the temperature images is to use referenceless thermometry (205, 206). This approach removes the need for a separately acquired reference image by estimating the phase of the heated region had it not been heated, and uses this estimated background phase instead of a reference phase image. There is therefore no need for correction of interscan motion or associated phase-variations if referenceless thermometry is used. However, the heated region needs to be confined to a small well-defined area surrounded by voxels of high SNR in order for a robust approximation of the background phase to be possible. Moreover, the

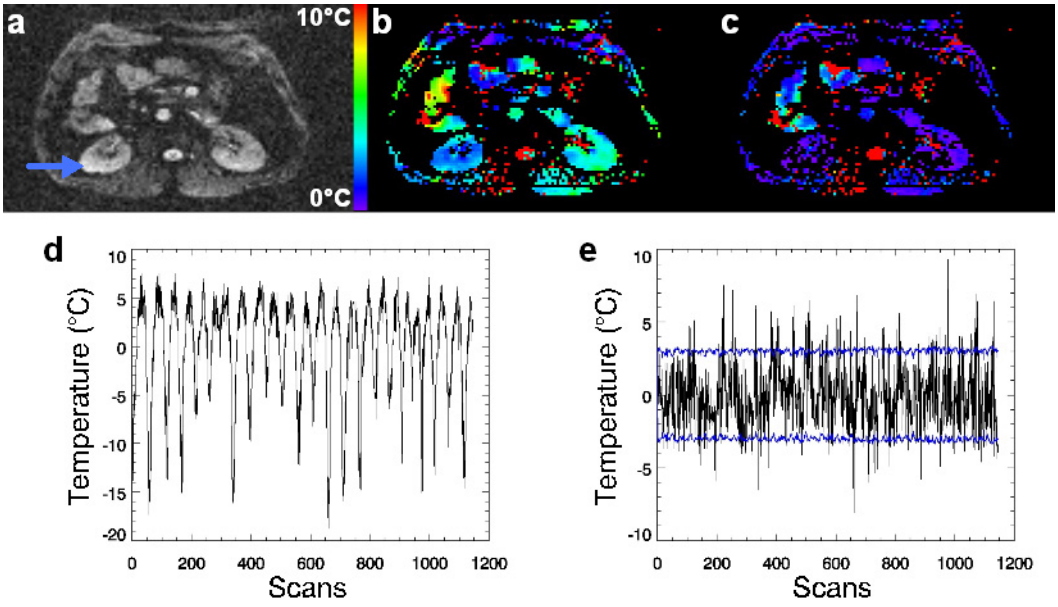

Figure 3.6: Transversal magnitude image (a), and uncorrected (b) and corrected (c) temperature standard deviation maps obtained in the abdomen during free breathing. The navigator was positioned on the left kidney as shown by the blue arrow. The large temperature fluctuations seen in the time curve of a voxel when no corrections are performed (d) are removed when utilizing the outlined corrections (e). The remaining temperature variation is within the limits imposed by the SNR (blue lines).

magnetic field of the region has to be uniform and spatial phase wraps have to be removed to allow for an accurate interpolation of the phase.

However, accurate estimation of the target region 3D motion is not only necessary for removing temperature image artifacts in conventional PRF thermometry, but also for adjusting the MR-HIFU therapy in order to avoid undesired tissue damage. The motion information can be used to apply heat only during mid-to-end expiration where there is little motion and thereby only ablate the desired region, although this would result in an inefficient heating due to the poor duty cycle. A preferable approach is to feed the obtained target region displacement into the transducer controlling software and continuously update the focal point location according to the estimated motion (51). We recently showed that the focal point can be electronically steered to follow the organ motion by adjusting the phase of the transducer elements in real-time according to the

observed 3D motion of the target region, without any assumptions on the organ motion (243). The HIFU focal point update latency was only 62 ms (post echo-time), which only caused a slight broadening of the point heating in a phantom experiment with motion amplitude and speed representative of human organ motion during free breathing.

In Publication **III**, a similar approach was employed for updating the position of the focal spot but using the fat-selective navigator instead of the conventional navigator to further improve the accuracy of the through-plane motion estimation and the 3D motion compensated thermometry. The obtained 3D motion estimate was used to electronically steer the focal spot according to the target organ motion. The feasibility of this approach for providing a full 3D motion compensated MR-HIFU ablation was demonstrated on *in vivo* porcine kidney. More details on this experiment and the results thereof can be found in Publication **III**.

3.2.8 Volumetric thermometry (I)

MR thermometry of HIFU therapy has traditionally been performed with one slice centered on the focus and placed either perpendicularly or parallel to the beam path (14, 49, 74, 115, 205). A stack of several parallel slices has also been used in some studies (32, 98, 159). These slice orientations are typically chosen for thermometry of HIFU induced hyperthermia as the heating is symmetrical around the beam axis within homogeneous tissue. Slices placed perpendicularly to the beam axis should thus generally show a relatively symmetrical heating. Slices placed parallel to the beam axis on the other hand visualize the temperature rise in both the near and far field of the beam path that is caused by attenuation, absorption and scattering of the ultrasound waves propagating towards and away from the focus.

The monitoring slices are typically centered on the location of the intended focal spot, since the focus normally receives most of the deposited thermal energy in homogenous tissue. However, diffraction, reflection, and refraction of the ultrasound can shift the location of the focus away from the intended focal spot (86). It is therefore often

desirable to use a stack of several adjacent imaging slices perpendicularly to the beam axis in order to ensure that the region of maximum heating is indeed monitored. Furthermore, targeted tissue is seldom perfectly homogeneous and the beam path commonly crosses several tissue interfaces, which leads to an inhomogeneous ultrasound absorption and thus also an inhomogeneous temperature rise. All tissue within the beam path will in fact be heated as all biological tissue absorbs ultrasound energy. The amount of heating does not only depend on the absorption coefficient but also on the local intensity that is typically low outside of the focus. However, if the tissue in the near or far field has higher absorption than expected, or acoustic boundaries are present that create local intensity maxima, then inadvertently high temperatures can occur outside of the target region. In order to avoid related adverse events during the HIFU exposure, it would therefore be beneficial to acquire temperature maps of the entire 3D volume of tissue within and around the beam path with an adequate spatial and temporal resolution. However, this is not feasible due to technical limitations.

Recent development has allowed for rapid acquisition and MR thermometry of multiple imaging planes. Even though the monitoring of the temperature rise near the focal spot is of most interest in order to visualize the maximum temperature and expected thermal damage, additional imaging planes may be used to improve the coverage the temperature monitoring and thus the safety of the MR-HIFU therapy. Imaging planes can for example be placed at tissue interfaces where air bubbles may be present that might act as acoustic boundaries by reflecting incident ultrasound. The reflected beam contributes to increasing the local absorption of ultrasound, subsequently increasing the local temperature rise to potentially dangerous levels (244, 245).

To the authors' knowledge, Publication **I** is the first article that uses multiplane real-time thermometry to improve the coverage and safety of MR-HIFU therapy by simultaneously monitoring the temperature rise both perpendicularly and parallel to the beam path. In this article, the temperature rise was simultaneously monitored in the target region, along the beam path, and at sensitive near-field tissue interfaces. Three coronal target region slices and one sagittal slice were automatically positioned

perpendicularly and parallel to the beam axis, respectively, and centered on the planned ablation. Two additional coronal slices were positioned in the near field: one at the skin and one at the interface between the muscle and subcutaneous fat. The slice positions of the volumetric thermometry outlined in Publication **I** are shown in Figure 3.7. The three coronal target region slices improved the target region coverage and reduced the risk of the maximum heating occurring outside of the monitored target region. These slices were also used to determine the width of the induced thermal lesion. The sagittal slice was used to monitor for any unexpected thermal behavior along the beam path and to assess the length of the thermal lesion. The excellent correlation found in Publication **I** between the thermal lesion size as identified on the postsonication images and that estimated by the thermal dose thresholds, both for the diameter and length, was taken to confirm the efficacy of the perpendicular target region slices. The additional near-field slices were used to monitor for potential excessive near-field heating. The slice positioned on the skin monitored for any unexpected temperature rise that could occur if air bubbles remain within the beam path between the skin and the gel pad (used to improve the acoustic coupling). The second additional slice positioned on the interface between the subcutaneous fat and the muscle reduced the probability of unmonitored tissue damage being induced in the subcutaneous fat layer due to excessive diffusion of heat from the target region. The importance of accurate and reliable monitoring of near-field heating is increased for volumetric ablations due to the larger energies deposited in each sonication event and the resulting higher near-field temperatures (48, 61). Subsequent studies following Publication **I** show that the two near-field slices of the outlined volumetric thermometry approach do indeed allow for an accurate monitoring of the near-field temperature rise and prediction of related adverse events (156, 157).

Intersecting imaging planes do cause a small partial saturation, consequently reducing the temperature accuracy at the cross-section. However, by choosing the slice acquisition order appropriately this reduction in temperature uncertainty can be minimized. In Publication **I**, the temperature standard deviation at the overlap of the orthogonal slices was increased by a maximum of only 8%. By using RF spoiling, stimulated echoes were also avoided at the cross-section.

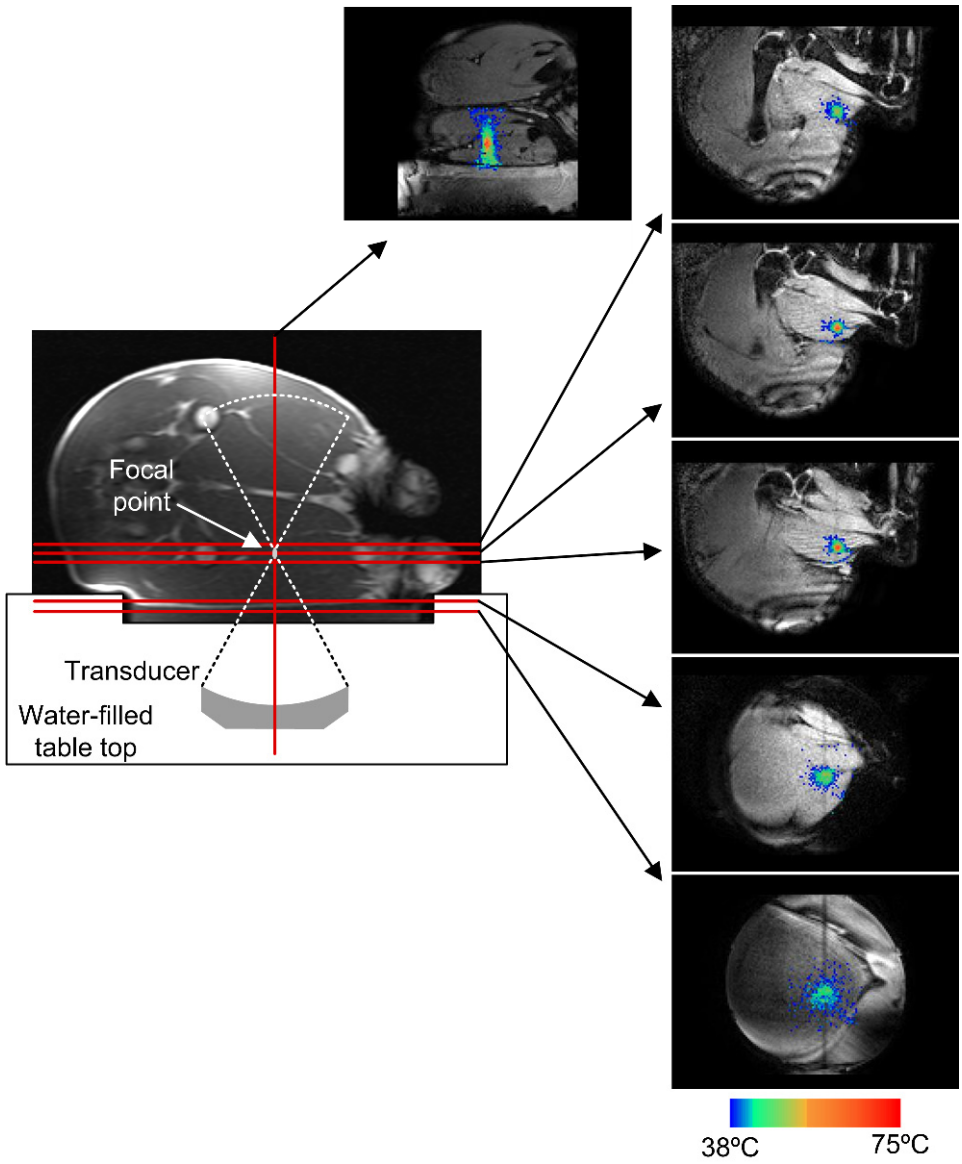

Figure 3.7: Temperature images acquired with the volumetric thermometry approach outlined in Publication **I**. The slice positions are shown as red overlays on the transverse planning image. The temperature maps are acquired at end of sonication of a 12 mm concentric circle volume ablation as described in Section 2.3. Artifactual temperatures outside of the region of interest are masked out. The sequence used for thermometry was a multi-shot RF-spoiled FFE-EPI with 11 k-space lines acquired per excitation, TR = 37 ms, TE = 20 ms, in-plane resolution 2.5 × 2.5 mm^2, slice thickness 7 mm, and a 121-binomial water-selective excitation pulse. The acquisition time for the 6 slices was 2.9 s. Part of image reproduced from Publication **I** with permission from AAPM.

3.3 Verification of treatment outcome

Thermal necrosis as induced by HIFU ablation introduces a range of tissue changes. Thermal damage may present itself as ruptured cell membranes, denaturized proteins, oedema, coagulated veins, increased vasoconstriction, deactivated enzymes, pycnotic nuclei, and disruption of fiber structure (13, 115, 131, 137). This causes such MR tissue parameters as T_1 and T_2 as well as the magnetization transfer constant to change (13, 73, 135, 175, 246, 247). The alteration of tissue perfusion, water diffusion, and stiffness induced by thermal damage may also be assessed using MRI (12, 13, 19, 131, 175, 247-249). However, the changes in the aforementioned tissue parameters are highly dependent on the tissue type, and adipose tissue as well as blood behave very differently from most non-fluid aqueous tissues (13).

T_2-weighted and contrast-enhanced post-treatment imaging are discussed in some detail below as these methods are used in Publication **I** to determine the volume of partial tissue damage and full coagulative necrosis, respectively. In Publication **I**, the thermal lesion volumes obtained in the T_2-weighted and contrast-enhanced images are correlated to the thermal dose contours corresponding to partial and full necrosis. This volume comparison was performed both parallel and perpendicularly to the beam axis in order to assess the predictive value of the thermal dose obtained online during sonication using multiplane volumetric thermometry. T_2-weighted and contrast-enhanced imaging are also the two most commonly used imaging methods to evaluate hyperthermia induced tissue damage. Other imaging methods for post-treatment treatment verification are also briefly described.

3.3.1 T_2-weighted imaging

The T_2 relaxation constant is known to be altered as a result of hyperthermia induced tissue damage (13, 246). Consequently one can use post-treatment T_2-weighted imaging to locate the area of HIFU induced thermal damage in soft tissues such as muscle (73, 75), breast (22), and brain (30, 250). In the T_2-weighted images, the thermal lesions

induced by HIFU typically have a hypointense core surrounded by a hyperintense ring (73, 75, 115, 130, 131), as can also be seen in Figure 3.8. Alternatively, the lesions may appear evenly hyperintense. The hypointense core has been shown to correspond to the volume of generalized thermal coagulation (130, 131). The hyperintense tissue has in turn been attributed to oedema and inflammation that both contribute to an increase in the T_2 relaxation constant (130, 131).

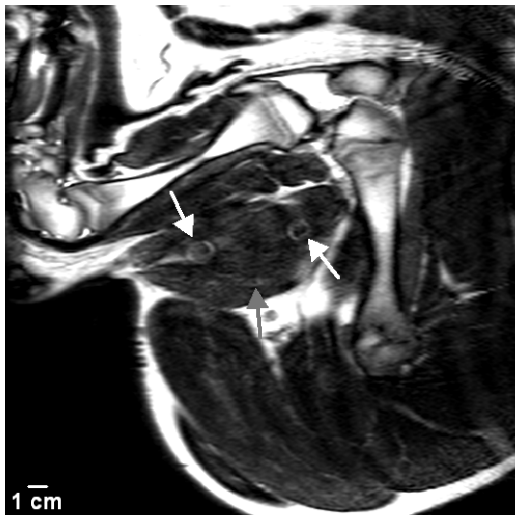

Figure 3.8: T_2-weighted post-treatment image in the coronal plane perpendicular to the HIFU beam axis following three differently sized volumetric ablations in a pig thigh. The arrows indicate the location of the ablations. The thermal lesion cross-sections appear circular with a hyperintense ring and hypointense core. The circular shape is in good correlation with the used volumetric sonication strategy explained in Section 2.3.

Several studies have reported a correlation of the size and shape of the thermal lesions as identified in histology to that seen on T_2-weighted post-treatment images (100, 130, 131, 251). A problem of using T_2-weighted images to asses tissue damage is that oedematous tissue contained within the bright ring may be only moderately damaged (131). It is therefore unclear whether or not tissue within this hyperintense rim will eventually recover from the inflicted thermal damage or become necrotic (130, 131).

In Publication **I**, an excellent correlation was found between the size of the induced thermal lesion as determined from T_2-weighted images and the thermal dose volume above 30 EM (diameter $R = 0.91$, length $R = 0.94$). The very good correlation was attributed to the sharp thermal lesion boundaries associated with the volumetric sonication strategy used in this publication. Similar comparisons between the size of the thermal dose volume and the T_2-weighted thermal lesion have also been performed previously although using different thermal dose thresholds (100, 115). The threshold of 30 EM was chosen in Publication **I** as this thermal dose threshold has previously been reported to be representative for onset of moderate thermal damage (74, 125). However, the appropriate thermal dose threshold for partial tissue damage may be different for other tissues due to differences in tissue composition.

3.3.2 Contrast-enhanced imaging

Blood vessels have been shown to be necrotic within thermally coagulated tissue (131, 137, 249, 252). The thermal lesions induced by HIFU consequently appear as hypointense regions in contrast-enhanced T_1-weighted images because there is no delivery of contrast agent to these non-perfused regions (12, 100, 131, 138, 249). The hypointense region is sometimes surrounded by a hyperintense ring corresponding to an accumulation of contrast agent at the edge of the non-perfused region. An example of thermal lesions induced in porcine thigh muscle can be seen in Figure 3.9, where both the hypointense center and the hyperintense border can be identified. Excellent correlation has been shown between the HIFU induced region of generalized thermal coagulation as determined via histology to the non-perfused region as seen in contrast-enhanced images (32, 100, 115, 131, 253). Consequently, contrast-enhanced imaging is currently considered the gold-standard method for determining thermally induced tissue necrosis with post-treatment MR imaging and has been widely used in numerous MR-HIFU applications. Contrast-enhanced imaging has proven accurate in determining post-treatment HIFU induced necrosis in for example muscle (12, 100, 115, 131), uterine fibroids (16, 19, 154, 254), breast (22, 23, 255), brain (30, 250), and prostate (32, 256). The main disadvantage of contrast-enhanced imaging is that the most commonly used contrast agents are gadolinium-based compounds, which are non-toxic

as compounds but may disintegrate and release the highly toxic gadolinium ion if heated (257). Contrast-enhanced imaging is consequently limited to the end of HIFU therapy. Even if the non-perfused volume obtained from the contrast-enhanced images would not correlate with the desired area of tissue destruction, the HIFU session is generally terminated to ensure patient safety.

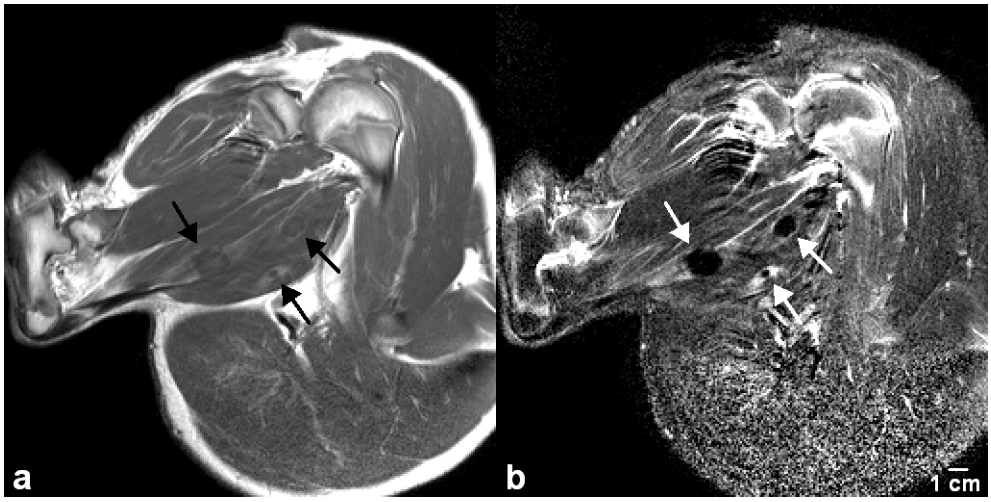

Figure 3.9: Contrast-enhanced post-treatment image (a) and contrast-enhanced difference image (b) of the same three volumetric ablations (indicated by arrows) in a pig thigh as in Figure 3.8. The coronal images perpendicular to the HIFU beam axis were taken from approximately the same position as in Figure 3.8. The contrast-enhanced difference image was obtained by subtracting the image of the same slice acquired before administering the contrast agent from that acquired 10 min after the administration of the contrast agent. The thermal lesion cross-sections appear circular with a hyperintense ring and hypointense core. The lesions can be much more easily identified in the difference image (b), despite both images being similarly windowed.

In Publication **I**, an excellent correlation was found between the size of the non-perfused thermal lesion, as determined from contrast-enhanced images, and the thermal dose volume above 240 EM (diameter R = 0.93, length R = 0.96). Similar comparisons between the size of the thermal dose volume and the non-perfused thermal lesion have previously been performed, although most reported a lower level of correlation (100, 115, 258). The excellent correlation found in Publication **I** was again attributed to the

sharp thermal lesion boundaries created by the employed volumetric sonication strategy and was also taken as a verification of the prediction accuracy of the used volumetric thermometry. The threshold of 240 EM was chosen as it is commonly used as a predictor of full coagulative necrosis (74, 115, 125, 126). While there is a good correlation between the thermal dose estimate and the non-perfused volume for smaller ablated volumes, there have been reports showing that the non-perfused area can sometimes extend beyond the heated region if larger volumes are ablated (258, 259). This mismatch has been attributed to thermal coagulation and subsequent occlusion of vessels that might be more probable with larger ablation volumes and may reduce or remove perfusion of downstream unheated tissue (137, 258, 259). The cells in the non-perfused unheated tissue may eventually become necrotic depending on the level of vascular constriction or occlusion, and whether or not the induced occlusion is permanent (68, 260-262).

3.3.3 Other imaging methods

Diffusion weighted imaging has also been suggested for post-treatment verification of HIFU induced tissue damage (175, 256, 259, 263). Because diffusion weighted imaging is sensitive to changes in the diffusion of water molecules in the intra- and intercellular environments, this imaging method can be used to discern immediate changes in the tissue microstructure following HIFU therapy (259, 263). An apparent diffusion coefficient may moreover be calculated using the obtained diffusion images that can be used as a quantitative indicator of the water movement within the tissue. Diffusion weighted imaging may furthermore be performed during therapy to assess therapy progress. It has also been shown that the region of altered diffusion correlates better with the region of thermal damage than with the non-perfused region directly following the HIFU session (259). This indicates that the imaging technique is sensitive to HIFU induced thermal damage but not to tissue alteration due to secondary effects such as vascular occlusion. Even though the imaging method is very promising for post-treatment damage verification, it does suffer from a high sensitivity to motion as well as potentially long imaging times if high spatial resolution and several slices are required.

Moreover, the obtained apparent diffusion coefficient may increase, decrease, or remain unaltered directly after the HIFU therapy depending on the tissue composition (259).

Another interesting, but so far less used, imaging method for assessing thermal tissue damage is MR elastography (247, 264). This imaging method can be used to calculate the tissue shear modulus by applying stiffness probing shear-waves appropriately timed to the MR imaging sequence. It has been shown that the elasticity of soft tissue is reduced as a consequence of the thermal coagulation and protein denaturation induced by HIFU ablation, and that the resulting reduction in elasticity can be determined using MR elastography (247, 264). Moreover, PRF thermometry may be performed using the same data as acquired for MR elastography allowing for simultaneous mapping of temperature and tissue stiffness (248). The fact that application of HIFU itself induces shear-waves that can be imaged with MR elastography opens for an interesting prospect of simultaneously inducing and assessing the thermal damage with HIFU ablation and MR elastography, respectively, while also simultaneously estimating the resulting temperature rise with PRF thermometry (71, 248, 265).

4 Conclusions

A volumetric ablation method based on the sonication along outward-moving concentric circles was developed and evaluated in Publication **I**. This design, inspired by the inside-to-out spirals of Salomir *et al.* (98), utilizes heat administered during the inner circles to reduce the required energy deposition at the outer circles. The proposed sonication strategy was evaluated *in vivo* and the energy efficiency was shown to improve with increasing trajectory size. These experiments also showed that the resulting thermal lesions were uniformly necrosed and that the transition zone between necrosed and healthy tissue, *i.e.* the region of unknown tissue outcome, was very narrow and independent of trajectory size, which is imperative for accurate ablation of malignant cancerous tissue. The presented sonication strategy is probably the most energy efficient existing method of HIFU ablation.

The increased energy deposition associated with the proposed volumetric ablation method does, however, increase the near-field heating and subsequently the risk of related adverse events (47, 61). In order to reduce these risks to an acceptable level, a rapid volumetric multiplane MR thermometry method was also developed and evaluated in Publication **I**. The accuracy and prediction value of the presented thermometry approach was evaluated *in vivo* and the correlation between the thermal lesion size as identified on the postsonication images and that estimated by the thermal dose thresholds was found to be excellent. Temperature and thermal dose images obtained with volumetric thermometry can thus provide an accurate and rapid online estimate of the temperature rise within the entire heated region as well as a clinical end point for the MR-HIFU therapy. The volumetric monitoring and online visualization presented in Publication **I** is, to the authors' knowledge, the first publication on true multiplane thermometry with nonparallel slices. The presented approach also uses novel dedicated near-field slices to reduce the risk of inducing skin burns and unintended damage to the subcutaneous fat.

A common problem of any HIFU therapy is that sonication outcome depends on largely unknown tissue parameters. This makes feedback control of the HIFU ablation based on the actual observed thermal response highly desirable to better obtain the intended therapy outcome. A binary feedback approach specifically designed for the volumetric ablation strategy of Publication **I** was to this aim developed in Publication **II**. The simple and robust feedback algorithm was evaluated *in vivo* and proved to significantly reduce variability in the ablation outcome as compared to the non-feedback approach that uses a predetermined sonication duration and power. Moreover, the induced thermal lesion correlated much better with the planned lesion size when binary feedback was utilized. Energy efficiency was also improved as compared to non-feedback ablations due to the more accurate energy deposition.

Another problem of MR-HIFU is that several abdominal organs, which would be prime candidates for MR-HIFU, are subject to motion during the respiratory cycle. This motion causes artifacts in PRF-based MR thermometry due to misregistrations between the current acquired image and the reference image as well as due to fluctuations of the local magnetic field experienced by the moving organ. Methods have previously been described for removing in-plane misregistrations (56, 218), but no feasible MR imaging methods have been presented for accurate real-time correction of through-plane motion. The spectral selective pencil-beam navigator described in Publication **III** provides a solution to this problem by using a fat-selective pencil-beam navigator for adaptive slice tracking. Rigorous simulations showed the feasibility, but also the complex spectral-spatial behavior, of the suggested approach. An *in vivo* tracking experiment with the pencil-beam navigator placed directly on the kidney of a volunteer under free breathing demonstrated the improved signal contrast and subsequent improved tracking provided by the fat-selective navigator as compared to the conventional non-selective navigator.

A multi-baseline method for the correction of respiratory-induced magnetic field variations and temperature artifacts was in turn presented in Publication **IV**. The suggested correction method used a learning stage to populate an indexed look-up-table from which the appropriate reference image was then retrieved during therapy. The

pencil-beam navigators, albeit in their non-selective form, were used to retrieve the appropriate reference image. The approach suggested in Publication **IV** furthermore used a model to calculate a more appropriate reference phase in the event that the displacement obtained during intervention falls in between those used as indices in the look-up-table. The suggested approach was evaluated for MR thermometry of the breast in five female volunteers under free breathing with no heat applied. The proposed correction was found to substantially reduce the fluctuations in the apparent temperature induced by breathing.

In-plane and through-plane motion correction as well as multi-baseline correction of the reference phase were combined in Publication **V** to provide real-time 3D motion compensation for MR thermometry of abdominal organs. The through-plane correction utilized the spectral selective navigator of Publication **III**, whereas in-plane correction was obtained by a 2D optical-flow algorithm. Respiratory induced phase-fluctuations were corrected using the approach of Publication **IV** with a densely populated look-up-table. The suggested approach was shown to remove the temperature fluctuations induced by respiratory motion in an MR thermometry experiment on the kidney of a volunteer under free breathing with no heat applied. The residual temperature variations were within the bounds imposed by the SNR of the imaging sequence.

Finally, the methods used in Publication **V** for 3D motion estimation were also used in Publication **III** to demonstrate the feasibility of fully 3D motion compensated MR-HIFU ablation on *in vivo* porcine kidney including motion compensation of both thermometry and focal point position. The obtained target location displacement was fed back to the transducer-controlling software that within a few tens of milliseconds from the acquisition of the image updated the focal spot position according to the organ motion by applying an updated phase for each channel of the phased-array transducer.

The technology of MR-HIFU has developed immensely in the last 17 years since Cline *et al.* (11) first suggested MR for monitoring of HIFU therapy. Most of the research has been proof-of-principle rather than directed towards creating robust and reliable

methods for clinical MR-HIFU therapy. The bulk of the research for this thesis was therefore aimed at developing an efficient, safe, and robust method of MR-HIFU ablation for the clinical Philips MR-HIFU system that is currently used in a pilot study for uterine fibroid ablation. The research presented in the latter part of the thesis is a step towards clinical MR-HIFU therapy of mobile organs, although obtaining the reliability required for clinical MR-HIFU therapy of abdominal organs remains a challenge. The vision of a fully automated clinical MR-HIFU therapy of mobile organs may not be impossible in the future. However, a lot of work remains to be done especially with regards to improving the reliability and robustness of the motion correction and feedback algorithms, but also with regards to reducing treatment time by using more efficient sonication strategies and feedback algorithms better suited for rapid energy efficient ablation.

	Fulfillment of the aims	**Publication**
1.	The combination of the developed volumetric sonication strategy and multiplane MR thermometry was shown to provide an energy efficient yet safe MR-HIFU therapy in a large animal model.	**I**
2.	The automatic control of the volumetric sonication provided by the developed binary feedback algorithm was shown to significantly improve the reliability of the sonication outcome in a large animal model.	**II**
3.	The developed fat-selective navigator was found to enable accurate real-time 3D motion compensation of both MR thermometry and focal point position.	**III, IV, V**

5 Summary of the publications

Publication **I**: 32 *in vivo* volumetric ablations of different trajectory sizes were performed in porcine thigh muscle with simultaneous monitoring by multiplane MR thermometry. The energy efficiency of the ablation improved with trajectory size and was 0.03, 0.24, and 0.52 cm^3/kJ for the 4, 12, and 16 mm diameter trajectories, respectively. The induced thermal lesions were well-defined with narrow transition zones between healthy and necrosed tissue, and a thermal dose uniformly above 240 EM within the trajectory borders. These results were verified by histology. Moreover, the correlation of the 30 EM and 240 EM thermal dose volume size obtained with multiplane thermometry to that of the thermal lesions as identified on the postsonication images was excellent (R = 0.91 – 0.96).

Publication **II**: 90 *in vivo* volumetric ablations of different trajectory sizes were performed in porcine thigh muscle. 60 of these ablations were controlled by the developed binary feedback algorithm and 30 were without feedback control for comparison. The diameter and length of the thermal lesions induced by the feedback controlled ablations had a significantly reduced variance as compared to those of the non-feedback controlled ablations. Furthermore, the diameters of the feedback controlled ablations were very close to those predicted by simulations, indicating that variability due to tissue inhomogeneity was mostly removed. Energy efficiency was also improved as compared to non-feedback ablations due to the more accurate energy deposition.

Publication **III**: Simulations were performed to analyze the spectral-spatial response of the developed spectral-selective navigator pulse. These simulations showed that the spectral-spatial response of the proposed binomial 2D RF pulse train was in fact identical to the spectral-response of the binomial weighting modulated by the spectral-spatial response of the conventional spiral-encoded 2D RF pulse. A tracking experiment on a human kidney under free breathing showed the improved direct slice tracking performance provided by the fat-selective navigator. A 3D motion compensated MR-HIFU ablation on *in vivo* porcine kidney was also performed with real-time 3D motion compensation of MR thermometry and beam steering of the focal spot according to the

observed organ motion. The success of this experiment demonstrated the feasibility of the fat-selective navigator for providing the accurate through-plane motion estimation necessary for 3D motion compensated MR-HIFU therapy of mobile organs.

Publication **IV**: A multi-baseline approach was used to correct for the local magnetic field and phase fluctuations induced by breathing in the breast of five female volunteers without applying heat. The temperature variance was reduced from an average of 5.4 to 1.6 °C when a multi-baseline approach was utilized. Applying an additional model-based correction further reduced the average standard deviation to 1.4 °C, when the theoretical limit imposed by the SNR was on average 1 °C.

Publication **V**: Three dimensional motion compensation of MR thermometry was performed by combining multi-baseline compensation with image registration and the spectral-selective navigator of Publication **III**. This approach was evaluated for motion compensation of thermometry in the kidney of a volunteer under free breathing. The compensation strategy proved to reduce the fluctuations in the temperature to the theoretical level imposed by the SNR. Three-dimensional motion compensation of thermometry was also evaluated for an RF-heating experiment in a mobile phantom.

References

1. Wood RW, Loomis A. The physical and biological effects of high frequency sound-waves of great intensity. Phil Mag 1927;4:7-14.

2. Szent-Györgi A. Chemical and biological effects of ultrasonic radiation. Nature 1933;131(278).

3. Lynn JG, Zwemer RL, Chick AJ, Miller AE. A new method for the generation and use of focused ultrasound in experimental biology. J Gen Physiol 1942;26:179-193.

4. Ballantine HT, Jr., Bell E, Manlapaz J. Progress and problems in the neurological applications of focused ultrasound. J Neurosurg 1960;17:858-876.

5. Fry FJ, Johnson LK. Tumor irradiation with intense ultrasound. Ultrasound Med Biol 1978;4(4):337-341.

6. Fry WJ, Mosberg WH, Jr., Barnard JW, Fry FJ. Production of focal destructive lesions in the central nervous system with ultrasound. J Neurosurg 1954;11(5):471-478.

7. Fry WJ, Barnard JW, Fry FJ, Brennan JF. Ultrasonically produced localized selective lesions in the central nervous system. Am J Phys Med 1955;34(3):413-423.

8. Lele PP. A simple method for production of trackless focal lesions with focused ultrasound: physical factors. J Physiol 1962;160:494-512.

9. Lele PP. Production of deep focal lesions by focused ultrasound--current status. Ultrasonics 1967;5:105-112.

10. Pond JB. The role of heat in the production of ultrasonic focal lesions. J Acoust Soc Am 1970;47(6):1607-1611.

11. Cline HE, Schenck JF, Hynynen K, Watkins RD, Souza SP, Jolesz FA. MR-guided focused ultrasound surgery. J Comput Assist Tomogr 1992;16(6):956-965.

12. Hynynen K, Darkazanli A, Damianou CA, Unger E, Schenck JF. The usefulness of a contrast agent and gradient-recalled acquisition in a steady-state imaging sequence for magnetic resonance imaging-guided noninvasive ultrasound surgery. Invest Radiol 1994;29(10):897-903.

13. Graham SJ, Stanisz GJ, Kecojevic A, Bronskill MJ, Henkelman RM. Analysis of changes in MR properties of tissues after heat treatment. Magn Reson Med 1999;42(6):1061-1071.

14. Cline HE, Hynynen K, Hardy CJ, Watkins RD, Schenck JF, Jolesz FA. MR temperature mapping of focused ultrasound surgery. Magn Reson Med 1994;31(6):628-636.

15. Ishihara Y, Calderon A, Watanabe H, Okamoto K, Suzuki Y, Kuroda K, Suzuki Y. A precise and fast temperature mapping using water proton chemical shift. Magn Reson Med 1995;34(6):814-823.

16. Stewart EA, Gedroyc WM, Tempany CM, Quade BJ, Inbar Y, Ehrenstein T, Shushan A, Hindley JT, Goldin RD, David M, Sklair M, Rabinovici J. Focused ultrasound treatment of uterine fibroid tumors: safety and feasibility of a noninvasive thermoablative technique. Am J Obstet Gynecol 2003;189(1):48-54.

17. Stewart EA, Rabinovici J, Tempany CM, Inbar Y, Regan L, Gostout B, Hesley G, Kim HS, Hengst S, Gedroyc WM. Clinical outcomes of focused ultrasound surgery for the treatment of uterine fibroids. Fertil Steril 2006;85(1):22-29.

18. Stewart EA, Gostout B, Rabinovici J, Kim HS, Regan L, Tempany CM. Sustained relief of leiomyoma symptoms by using focused ultrasound surgery. Obstet Gynecol 2007;110(2 Pt 1):279-287.

19. Tempany CM, Stewart EA, McDannold N, Quade BJ, Jolesz FA, Hynynen K. MR imaging-guided focused ultrasound surgery of uterine leiomyomas: a feasibility study. Radiology 2003;226(3):897-905.

20. Stewart EA. Uterine fibroids. Lancet 2001;357(9252):293-298.

21. Hesley GK, Gorny KR, Henrichsen TL, Woodrum DA, Brown DL. A clinical review of focused ultrasound ablation with magnetic resonance guidance: an option for treating uterine fibroids. Ultrasound Q 2008;24(2):131-139.

22. Hynynen K, Pomeroy O, Smith DN, Huber PE, McDannold NJ, Kettenbach J, Baum J, Singer S, Jolesz FA. MR imaging-guided focused ultrasound surgery of fibroadenomas in the breast: a feasibility study. Radiology 2001;219(1):176-185.

23. Furusawa H, Namba K, Thomsen S, Akiyama F, Bendet A, Tanaka C, Yasuda Y, Nakahara H. Magnetic resonance-guided focused ultrasound surgery of breast cancer: reliability and effectiveness. J Am Coll Surg 2006;203(1):54-63.

24. Gianfelice D, Khiat A, Amara M, Belblidia A, Boulanger Y. MR imaging-guided focused US ablation of breast cancer: histopathologic assessment of effectiveness-- initial experience. Radiology 2003;227(3):849-855.

25. Huber PE, Jenne JW, Rastert R, Simiantonakis I, Sinn HP, Strittmatter HJ, von FD, Wannenmacher MF, Debus J. A new noninvasive approach in breast cancer therapy using magnetic resonance imaging-guided focused ultrasound surgery. Cancer Res 2001;61(23):8441-8447.

26. Zippel DB, Papa MZ. The use of MR imaging guided focused ultrasound in breast cancer patients; a preliminary phase one study and review. Breast Cancer 2005;12(1):32-38.

27. Catane R, Beck A, Inbar Y, Rabin T, Shabshin N, Hengst S, Pfeffer RM, Hanannel A, Dogadkin O, Liberman B, Kopelman D. MR-guided focused ultrasound surgery (MRgFUS) for the palliation of pain in patients with bone metastases--preliminary clinical experience. Ann Oncol 2007;18(1):163-167.

28. Gianfelice D, Gupta C, Kucharczyk W, Bret P, Havill D, Clemons M. Palliative treatment of painful bone metastases with MR imaging--guided focused ultrasound. Radiology 2008;249(1):355-363.

29. Liberman B, Gianfelice D, Inbar Y, Beck A, Rabin T, Shabshin N, Chander G, Hengst S, Pfeffer R, Chechick A, Hanannel A, Dogadkin O, Catane R. Pain palliation in patients with bone metastases using MR-guided focused ultrasound surgery: a multicenter study. Ann Surg Oncol 2009;16(1):140-146.

30. Ram Z, Cohen ZR, Harnof S, Tal S, Faibel M, Nass D, Maier SE, Hadani M, Mardor Y. Magnetic resonance imaging-guided, high-intensity focused ultrasound for brain tumor therapy. Neurosurgery 2006;59(5):949-955.

31. Diederich CJ, Stafford RJ, Nau WH, Burdette EC, Price RE, Hazle JD. Transurethral ultrasound applicators with directional heating patterns for prostate thermal therapy: *in vivo* evaluation using magnetic resonance thermometry. Med Phys 2004;31(2):405-413.

32. Hazle JD, Diederich CJ, Kangasniemi M, Price RE, Olsson LE, Stafford RJ. MRI-guided thermal therapy of transplanted tumors in the canine prostate using a directional transurethral ultrasound applicator. J Magn Reson Imaging 2002;15(4):409-417.

33. Ross AB, Diederich CJ, Nau WH, Rieke V, Butts RK, Sommer G, Gill H, Bouley DM. Curvilinear transurethral ultrasound applicator for selective prostate thermal therapy. Med Phys 2005;32(6):1555-1565.

34. Kirkham AP, Emberton M, Hoh IM, Illing RO, Freeman AA, Allen C. MR imaging of prostate after treatment with high-intensity focused ultrasound. Radiology 2008;246(3):833-844.

35. Sanghvi NT, Foster RS, Bihrle R, Casey R, Uchida T, Phillips MH, Syrus J, Zaitsev AV, Marich KW, Fry FJ. Noninvasive surgery of prostate tissue by high intensity focused ultrasound: an updated report. Eur J Ultrasound 1999;9(1):19-29.

36. de Zwart JA, Salomir R, Vimeux F, Klaveness J, Moonen CTW. On the feasibility of local drug delivery using thermo-sensitive liposomes and MR-guided focused ultrasound. ISMRM, 8th Annual Meeting 2000;43.

37. Deckers R, Rome C, Moonen CT. The role of ultrasound and magnetic resonance in local drug delivery. J Magn Reson Imaging 2008;27(2):400-409.

38. Dromi S, Frenkel V, Luk A, Traughber B, Angstadt M, Bur M, Poff J, Xie J, Libutti SK, Li KC, Wood BJ. Pulsed-high intensity focused ultrasound and low temperature-sensitive liposomes for enhanced targeted drug delivery and antitumor effect. Clin Cancer Res 2007;13(9):2722-2727.

39. Weinstein JN, Magin RL, Yatvin MB, Zaharko DS. Liposomes and local hyperthermia: selective delivery of methotrexate to heated tumors. Science 1979;204(4389):188-191.

40. Hynynen K, McDannold N, Vykhodtseva N, Jolesz FA. Noninvasive MR imaging-guided focal opening of the blood-brain barrier in rabbits. Radiology 2001;220(3):640-646.

41. Treat LH, McDannold N, Vykhodtseva N, Zhang Y, Tam K, Hynynen K. Targeted delivery of doxorubicin to the rat brain at therapeutic levels using MRI-guided focused ultrasound. Int J Cancer 2007;121(4):901-907.

42. Guilhon E, Quesson B, Moraud-Gaudry F, de Verneuil H, Canioni P, Salomir R, Voisin P, Moonen CT. Image-guided control of transgene expression based on local hyperthermia. Mol Imaging 2003;2(1):11-17.

43. Madio DP, van GP, DesPres D, Olson AW, de Zwart JA, Fawcett TW, Holbrook NJ, Mandel M, Moonen CT. On the feasibility of MRI-guided focused ultrasound for local induction of gene expression. J Magn Reson Imaging 1998;8(1):101-104.

44. Cline HE, Hynynen K, Watkins RD, Adams WJ, Schenck JF, Ettinger RH, Freund WR, Vetro JP, Jolesz FA. Focused US system for MR imaging-guided tumor ablation. Radiology 1995;194(3):731-737.

45. Ebbini ES, Cain CA. Multiple-focus ultrasound phased-array pattern synthesis: optimal driving-signal distributions for hyperthermia. IEEE Trans Ultrason Ferroelectr Freq Control 1989;36(5):540-548.

46. Gavrilov LR, Hand JW. A theoretical assessment of the relative performance of spherical phased arrays for ultrasound surgery. IEEE Trans Ultrason Ferroelectr Freq Control 2000;47(1):125-139.

47. Damianou C, Hynynen K. Focal spacing and near-field heating during pulsed high temperature ultrasound therapy. Ultrasound Med Biol 1993;19(9):777-787.

48. Fan X, Hynynen K. Ultrasound surgery using multiple sonications--treatment time considerations. Ultrasound Med Biol 1996;22(4):471-482.

49. Salomir R, Vimeux FC, de Zwart JA, Grenier N, Moonen CT. Hyperthermia by MR-guided focused ultrasound: accurate temperature control based on fast MRI and a physical model of local energy deposition and heat conduction. Magn Reson Med 2000;43(3):342-347.

50. Vimeux FC, de Zwart JA, Palussiere J, Fawaz R, Delalande C, Canioni P, Grenier N, Moonen CT. Real-time control of focused ultrasound heating based on rapid MR thermometry. Invest Radiol 1999;34(3):190-193.

51. Denis de Senneville B, Mougenot C, Moonen CT. Real-time adaptive methods for treatment of mobile organs by MRI-controlled high-intensity focused ultrasound. Magn Reson Med 2007;57(2):319-330.

52. Friston KJ, Ashburner J, Frith CD, Poline JB, Heather JD, Frackowiak RSJ. Spatial registration and normalization of images. Hum Brain Mapp 1995;2:165-189.

53. Horn BKP, Schunck BG. Determining optical flow. Artif Intel 1981;17:185-203.

54. Maintz JB, Viergever MA. A survey of medical image registration. Med Image Anal 1998;2(1):1-36.

55. McConnell MV, Khasgiwala VC, Savord BJ, Chen MH, Chuang ML, Edelman RR, Manning WJ. Prospective adaptive navigator correction for breath-hold MR coronary angiography. Magn Reson Med 1997;37(1):148-152.

56. Denis de Senneville B, Quesson B, Desbarats P, Salomir R, Palussiere J, Moonen CTW. Atlas-based motion correction for on-line MR temperature mapping. IEEE International Conference on Image Processing (ICIP) 2004;3:2571-2574.

57. Young IR, Hajnal JV, Roberts IG, Ling JX, Hill-Cottingham RJ, Oatridge A, Wilson JA. An evaluation of the effects of susceptibility changes on the water chemical shift method of temperature measurement in human peripheral muscle. Magn Reson Med 1996;36(3):366-374.

58. Vigen KK, Daniel BL, Pauly JM, Butts K. Triggered, navigated, multi-baseline method for proton resonance frequency temperature mapping with respiratory motion. Magn Reson Med 2003;50(5):1003-1010.

59. Hill CR, Bamber JC, ter Haar GR. Physical principles of medical ultrasonics. 2nd ed. John Wiley & Sons Ltd.; 2004.

60. Cathignol D, Sapozhnikov OA, Theillere Y. Comparison of acoustic fields radiated from piezoceramic and piezocomposite focused radiators. J Acoust Soc Am 1999;105(5):2612-2617.

61. Daum DR, Hynynen K. A 256-element ultrasonic phased array system for the treatment of large volumes of deep seated tissue. IEEE Trans Ultrason Ferroelectr Freq Control 1999;46(5):1254-1268.

62. Ebbini ES, Cain CA. A spherical-section ultrasound phased array applicator for deep localized hyperthermia. IEEE Trans Biomed Eng 1991;38(7):634-643.

63. Goss SA, Frizzell LA, Kouzmanoff JT, Barich JM, Yang JM. Sparse random ultrasound phased array for focal surgery. IEEE Trans Ultrason Ferroelectr Freq Control 1996;43(6):1111-1121.

64. Pernot M, Aubry JF, Tanter M, Thomas JL, Fink M. High power transcranial beam steering for ultrasonic brain therapy. Phys Med Biol 2003;48(16):2577-2589.

65. Rivens IH, Clarke RL, Ter Haar GR. Design of focused ultrasound surgery transducers. IEEE Trans Ultrason Ferroelectr Freq Control 1996;43(6):1023-1031.

66. Umemura S, Cain CA. The sector-vortex phased array: acoustic field synthesis for hyperthermia. IEEE Trans Ultrason Ferroelectr Freq Control 1989;36(2):249-257.

67. Hynynen K. The threshold for thermally significant cavitation in dog's thigh muscle *in vivo*. Ultrasound Med Biol 1991;17(2):157-169.

68. Hynynen K, Chung AH, Colucci V, Jolesz FA. Potential adverse effects of high-intensity focused ultrasound exposure on blood vessels *in vivo*. Ultrasound Med Biol 1996;22(2):193-201.

69. Hwang JH, Wang YN, Warren C, Upton MP, Starr F, Zhou Y, Mitchell SB. Preclinical *in vivo* evaluation of an extracorporeal HIFU device for ablation of pancreatic tumors. Ultrasound Med Biol 2009;35(6):967-975.

70. O'Brien WD, Jr. Ultrasound-biophysics mechanisms. Prog Biophys Mol Biol 2007;93(1-3):212-255.

71. Souchon R, Salomir R, Beuf O, Milot L, Grenier D, Lyonnet D, Chapelon JY, Rouviere O. Transient MR elastography (t-MRE) using ultrasound radiation force: theory, safety, and initial experiments *in vitro*. Magn Reson Med 2008;60(4):871-881.

72. ter Haar G. Ultrasound focal beam surgery. Ultrasound Med Biol 1995;21(9):1089-1100.

73. Hynynen K, Darkazanli A, Unger E, Schenck JF. MRI-guided noninvasive ultrasound surgery. Med Phys 1993;20(1):107-115.

74. McDannold NJ, King RL, Jolesz FA, Hynynen KH. Usefulness of MR imaging-derived thermometry and dosimetry in determining the threshold for tissue damage induced by thermal surgery in rabbits. Radiology 2000;216(2):517-523.

75. Hynynen K, Freund WR, Cline HE, Chung AH, Watkins RD, Vetro JP, Jolesz FA. A clinical, noninvasive, MR imaging-monitored ultrasound surgery method. Radiographics 1996;16(1):185-195.

76. Goss SA, Johnston RL, Dunn F. Comprehensive compilation of empirical ultrasonic properties of mammalian tissues. J Acoust Soc Am 1978;64(2):423-457.

77. Ludwig GD. The velocity of sound through tissues and the acoustic impedance of tissues. J Acoust Soc Am 1950;22(6):862-866.

78. Hill CR. Optimum acoustic frequency for focused ultrasound surgery. Ultrasound Med Biol 1994;20(3):271-277.

79. ter Haar G, Coussios C. High intensity focused ultrasound: physical principles and devices. Int J Hyperthermia 2007;23(2):89-104.

80. Wharton IP, Rivens IH, Ter Haar GR, Gilderdale DJ, Collins DJ, Hand JW, Abel PD, deSouza NM. Design and development of a prototype endocavitary probe for high-intensity focused ultrasound delivery with integrated magnetic resonance imaging. J Magn Reson Imaging 2007;25(3):548-556.

81. Chapelon JY, Cathignol D, Cain C, Ebbini E, Kluiwstra JU, Sapozhnikov OA, Fleury G, Berriet R, Chupin L, Guey JL. New piezoelectric transducers for therapeutic ultrasound. Ultrasound Med Biol 2000;26(1):153-159.

82. Daum DR, Buchanan MT, Fjield T, Hynynen K. Design and evaluation of a feedback based phased array system for ultrasound surgery. IEEE Trans Ultrason Ferroelectr Freq Control 1998;45(2):431-438.

83. Ebbini ES, Umemura SI, Ibbini M, Cain CA. A cylindrical-section ultrasound phased-array applicator for hyperthermia cancer therapy. IEEE Trans Ultrason Ferroelectr Freq Control 1988;35(5):561-572.

84. Fan X, Hynynen K. Control of the necrosed tissue volume during noninvasive ultrasound surgery using a 16-element phased array. Med Phys 1995;22(3):297-306.

85. Liu HL, McDannold N, Hynynen K. Focal beam distortion and treatment planning in abdominal focused ultrasound surgery. Med Phys 2005;32(5):1270-1280.

86. Fan X, Hynynen K. The effect of wave reflection and refraction at soft tissue interfaces during ultrasound hyperthermia treatments. J Acoust Soc Am 1992;91(3):1727-1736.

87. Fan X, Hynynen K. The effects of curved tissue layers on the power deposition patterns of therapeutic ultrasound beams. Med Phys 1994;21(1):25-34.

88. Liu HL, Chang H, Chen WS, Shih TC, Hsiao JK, Lin WL. Feasibility of transrib focused ultrasound thermal ablation for liver tumors using a spherically curved 2D array: a numerical study. Med Phys 2007;34(9):3436-3448.

89. Mougenot C. L'asservissement par IRM d'un réseau matriciel ultrasonore et ses applications thérapeutiques [dissertation]. L'Université Bordeaux 1; 2005.

90. Cain CA, Umemura SA. Concentric-ring and sector vortex phased array applicators for ultrasound hyperthermia therapy. IEEE Trans Microwave Theory Tech 1986;34(5):542-551.

91. Dupenloup F, Chapelon JY, Cathignol D, Sapozhnikov OA. Reduction of the grating lobes of annular arrays used in focused ultrasound surgery. IEEE Trans Ultrason Ferroelectr Freq Control 1996;43(6):991-998.

92. Ibbini MS, Cain CA. The concentric-ring array for ultrasound hyperthermia: combined mechanical and electrical scanning. Int J Hyperthermia 1990;6(2):401-419.

93. Umemura S, Cain CA. Acoustical evaluation of a prototype sector-vortex phased-array applicator. IEEE Trans Ultrason Ferroelectr Freq Control 1992;39(1):32-38.

94. Zhang L, Chen WZ, Liu YJ, Hu X, Zhou K, Chen L, Peng S, Zhu H, Zou HL, Bai J, Wang ZB. Feasibility of magnetic resonance imaging-guided high intensity focused ultrasound therapy for ablating uterine fibroids in patients with bowel lies anterior to uterus. Eur J Radiol 2008.

95. Hesley GK, Felmlee JP, Gebhart JB, Dunagan KT, Gorny KR, Kesler JB, Brandt KR, Glantz JN, Gostout BS. Noninvasive treatment of uterine fibroids: early Mayo Clinic experience with magnetic resonance imaging-guided focused ultrasound. Mayo Clin Proc 2006;81(7):936-942.

96. Diederich CJ, Nau WH, Ross AB, Tyreus PD, Butts K, Rieke V, Sommer G. Catheter-based ultrasound applicators for selective thermal ablation: progress towards MRI-guided applications in prostate. Int J Hyperthermia 2004;20(7):739-756.

97. Hutchinson EB, Hynynen K. Intracavitary ultrasound phased arrays for prostate thermal therapies: MRI compatibility and *in vivo* testing. Med Phys 1998;25(12):2392-2399.

98. Salomir R, Palussiere J, Vimeux FC, de Zwart JA, Quesson B, Gauchet M, Lelong P, Pergrale J, Grenier N, Moonen CT. Local hyperthermia with MR-guided focused ultrasound: spiral trajectory of the focal point optimized for temperature uniformity in the target region. J Magn Reson Imaging 2000;12(4):571-583.

99. Chopra R, Curiel L, Staruch R, Morrison L, Hynynen K. An MRI-compatible system for focused ultrasound experiments in small animal models. Med Phys 2009;36(5):1867-1874.

100. Hazle JD, Stafford RJ, Price RE. Magnetic resonance imaging-guided focused ultrasound thermal therapy in experimental animal models: correlation of ablation volumes with pathology in rabbit muscle and VX2 tumors. J Magn Reson Imaging 2002;15(2):185-194.

101. Damianou C, Pavlou M, Velev O, Kyriakou K, Trimikliniotis M. High intensity focused ultrasound ablation of kidney guided by MRI. Ultrasound Med Biol 2004;30(3):397-404.

102. Kopelman D, Inbar Y, Hanannel A, Pfeffer RM, Dogadkin O, Freundlich D, Liberman B, Catane R. Magnetic resonance guided focused ultrasound surgery. Ablation of soft tissue at bone-muscle interface in a porcine model. Eur J Clin Invest 2008;38(4):268-275.

103. Hynynen K. Biophysics and technology of ultrasound hyperthermia. In: Gautherie M, editor. Methods of External Hyperthermic Heating. New York: Springer-Verlag; 1990. 61-115.

104. Aubry JF, Tanter M, Pernot M, Thomas JL, Fink M. Experimental demonstration of noninvasive transskull adaptive focusing based on prior computed tomography scans. J Acoust Soc Am 2003;113(1):84-93.

105. Clement GT, Hynynen K. A non-invasive method for focusing ultrasound through the human skull. Phys Med Biol 2002;47(8):1219-1236.

106. Pennes HH. Analysis of tissue and arterial blood temperatures in the resting human forearm. J Appl Physiol 1948;1(2):93-122.

107. Lang J, Erdmann B, Seebass M. Impact of nonlinear heat transfer on temperature control in regional hyperthermia. IEEE Trans Biomed Eng 1999;46(9):1129-1138.

108. Chen L, ter HG, Hill CR, Dworkin M, Carnochan P, Young H, Bensted JP. Effect of blood perfusion on the ablation of liver parenchyma with high-intensity focused ultrasound. Phys Med Biol 1993;38(11):1661-1673.

109. Dragonu I, Lourenço de Oliveira P, Laurent C, Mougenot C, Grenier N, Moonen CT, Quesson B. Non-invasive determination of tissue thermal parameters from high intensity focused ultrasound treatment monitored by volumetric MRI thermometry. NMR Biomed 2009;22(8):843-851.

110. Hynynen K. The role of nonlinear ultrasound propagation during hyperthermia treatments. Med Phys 1991;18(6):1156-1163.

111. Goss SA, Fry FJ. Nonlinear acoustic behavior in focused ultrasonic fields: Observations of intensity dependent absorption in biological tissue. IEEE Trans Son Ultrason 1981;28(1):21-26.

112. Swindell W. A theoretical study of nonlinear effects with focused ultrasound in tissues: an "acoustic bragg peak". Ultrasound Med Biol 1985;11(1):121-130.

113. Damianou C. *In vitro* and *in vivo* ablation of porcine renal tissues using high-intensity focused ultrasound. Ultrasound Med Biol 2003;29(9):1321-1330.

114. Flynn HG. Physics of acoustic cavitation in liquids. In: Mason WP, editor. Physical acoustics. New York: Academic Press; 1964. 57-172.

115. Chung AH, Jolesz FA, Hynynen K. Thermal dosimetry of a focused ultrasound beam *in vivo* by magnetic resonance imaging. Med Phys 1999;26(9):2017-2026.

116. Malcolm AL, Ter Haar GR. Ablation of tissue volumes using high intensity focused ultrasound. Ultrasound Med Biol 1996;22(5):659-669.

117. Sokka SD, King R, Hynynen K. MRI-guided gas bubble enhanced ultrasound heating in *in vivo* rabbit thigh. Phys Med Biol 2003;48(2):223-241.

118. Sapareto SA, Dewey WC. Thermal dose determination in cancer therapy. Int J Radiat Oncol Biol Phys 1984;10(6):787-800.

119. Borrelli MJ, Thompson LL, Cain CA, Dewey WC. Time-temperature analysis of cell killing of BHK cells heated at temperatures in the range of 43.5 degrees C to 57.0 degrees C. Int J Radiat Oncol Biol Phys 1990;19(2):389-399.

120. Dewey WC. Arrhenius relationships from the molecule and cell to the clinic. Int J Hyperthermia 1994;10(4):457-483.

121. Dewhirst MW, Viglianti BL, Lora-Michiels M, Hanson M, Hoopes PJ. Basic principles of thermal dosimetry and thermal thresholds for tissue damage from hyperthermia. Int J Hyperthermia 2003;19(3):267-294.

122. Jung H. A generalized concept for cell killing by heat. Radiat Res 1986;106(1):56-72.

123. Lyng H, Monge OR, Bohler PJ, Rofstad EK. Relationships between thermal dose and heat-induced tissue and vascular damage after thermoradiotherapy of locally advanced breast carcinoma. Int J Hyperthermia 1991;7(3):403-415.

124. Lyons BE, Obana WG, Borcich JK, Kleinman R, Singh D, Britt RH. Chronic histological effects of ultrasonic hyperthermia on normal feline brain tissue. Radiat Res 1986;106(2):234-251.

125. Meshorer A, Prionas SD, Fajardo LF, Meyer JL, Hahn GM, Martinez AA. The effects of hyperthermia on normal mesenchymal tissues. Application of a histologic grading system. Arch Pathol Lab Med 1983;107(6):328-334.

126. Damianou C, Hynynen K. The effect of various physical parameters on the size and shape of necrosed tissue volume during ultrasound surgery. J Acoust Soc Am 1994;95(3):1641-1649.

127. McDannold N, Hynynen K, Wolf D, Wolf G, Jolesz F. MRI evaluation of thermal ablation of tumors with focused ultrasound. J Magn Reson Imaging 1998;8(1):91-100.

128. de Zwart JA. Fast magnetic resonance temperature imaging for control of localized hyperthermia in medicine [dissertation]. Universiteit Utrecht, The Netherlands; 2000.

129. Weidensteiner C, Quesson B, Caire-Gana B, Kerioui N, Rullier A, Trillaud H, Moonen CT. Real-time MR temperature mapping of rabbit liver *in vivo* during thermal ablation. Magn Reson Med 2003;50(2):322-330.

130. Chen L, Bouley D, Yuh E, D'Arceuil H, Butts K. Study of focused ultrasound tissue damage using MRI and histology. J Magn Reson Imaging 1999;10(2):146-153.

131. Cheng HL, Purcell CM, Bilbao JM, Plewes DB. Prediction of subtle thermal histopathological change using a novel analysis of Gd-DTPA kinetics. J Magn Reson Imaging 2003;18(5):585-598.

132. Farahani K, Mischel PS, Black KL, De Salles AA, Anzai Y, Lufkin RB. Hyperacute thermal lesions: MR imaging evaluation of development in the brain. Radiology 1995;196(2):517-520.

133. Graham SJ, Chen L, Leitch M, Peters RD, Bronskill MJ, Foster FS, Henkelman RM, Plewes DB. Quantifying tissue damage due to focused ultrasound heating observed by MRI. Magn Reson Med 1999;41(2):321-328.

134. Hill CR, Rivens I, Vaughan MG, Ter Haar GR. Lesion development in focused ultrasound surgery: a general model. Ultrasound Med Biol 1994;20(3):259-269.

135. Moriarty JA, Chen JC, Purcell CM, Ang LC, Hinks RS, Peters RD, Henkelman RM, Plewes DB, Bronskill MJ, Kucharczyk W. MRI monitoring of interstitial microwave-induced heating and thermal lesions in rabbit brain *in vivo*. J Magn Reson Imaging 1998;8(1):128-135.

136. Vykhodtseva N, Sorrentino V, Jolesz FA, Bronson RT, Hynynen K. MRI detection of the thermal effects of focused ultrasound on the brain. Ultrasound Med Biol 2000;26(5):871-880.

137. Chen L, ter HG, Robertson D, Bensted JP, Hill CR. Histological study of normal and tumor-bearing liver treated with focused ultrasound. Ultrasound Med Biol 1999;25(5):847-856.

138. Chung YC, Duerk JL. Signal formation in echo-shifted sequences. Magn Reson Med 1999;42(5):864-875.

139. Arefiev A, Prat F, Chapelon JY, Tavakkoli J, Cathignol D. Ultrasound-induced tissue ablation: studies on isolated, perfused porcine liver. Ultrasound Med Biol 1998;24(7):1033-1043.

140. McDannold NJ, Jolesz FA, Hynynen KH. Determination of the optimal delay between sonications during focused ultrasound surgery in rabbits by using MR imaging to monitor thermal buildup *in vivo*. Radiology 1999;211(2):419-426.

141. Hand JW, Vernon CC, Prior MV. Early experience of a commercial scanned focused ultrasound hyperthermia system. Int J Hyperthermia 1992;8(5):587-607.

142. Lele PP, Parker KJ. Temperature distributions in tissues during local hyperthermia by stationary or steered beams of unfocused or focused ultrasound. Br J Cancer Suppl 1982;5:108-121.

143. Moros EG, Roemer RB, Hynynen K. Simulations of scanned focused ultrasound hyperthermia. the effects of scanning speed and pattern on the temperature fluctuations at the focal depth. IEEE Trans Ultrason Ferroelectr Freq Control 1988;35(5):552-560.

144. Salomir R, Denis de Senneville B, Mougenot C, Moonen CTW. On-line high order correction of PRF thermometry for the magnetic perturbation due to the motion of a FUS transducer. MAGMA 2002;15:118.

145. Chauhan S, Lowe MJ, Davies BL. A multiple focused probe approach for high intensity focused ultrasound based surgery. Ultrasonics 2001;39(1):33-44.

146. Fry FJ. Precision high intensity focusing ultrasonic machines for surgery. Am J Phys Med 1958;37(3):152-156.

147. Hynynen K, Roemer R, Anhalt D, Johnson C, Xu ZX, Swindell W, Cetas T. A scanned, focused, multiple transducer ultrasonic system for localized hyperthermia treatments. Int J Hyperthermia 1987;3(1):21-35.

148. Häcker A, Chauhan S, Peters K, Hildenbrand R, Marlinghaus E, Alken P, Michel MS. Multiple high-intensity focused ultrasound probes for kidney-tissue ablation. J Endourol 2005;19(8):1036-1040.

149. Lin WL, Chen YY, Lin SY, Yen JY, Shieh MJ, Kuo TS. Optimal configuration of multiple-focused ultrasound transducers for external hyperthermia. Med Phys 1999;26(9):2007-2016.

150. Wan H, VanBaren P, Ebbini ES, Cain CA. Ultrasound surgery: comparison of strategies using phased array systems. IEEE Trans Ultrason Ferroelectr Freq Control 1996;43(6):1085-1097.

151. Daum DR, Hynynen K. Thermal dose optimization via temporal switching in ultrasound surgery. IEEE Trans Ultrason Ferroelectr Freq Control 1998;45(1):208-215.

152. Daum DR, Smith NB, King R, Hynynen K. *In vivo* demonstration of noninvasive thermal surgery of the liver and kidney using an ultrasonic phased array. Ultrasound Med Biol 1999;25(7):1087-1098.

153. Ebbini ES, Cain CA. Optimization of the intensity gain of multiple-focus phased-array heating patterns. Int J Hyperthermia 1991;7(6):953-973.

154. Hindley J, Gedroyc WM, Regan L, Stewart E, Tempany C, Hynyen K, McDannold N, Inbar Y, Itzchak Y, Rabinovici J, Kim HS, Geschwind JF, Hesley G, Gostout B, Ehrenstein T, Hengst S, Sklair-Levy M, Shushan A, Jolesz F. MRI guidance of focused ultrasound therapy of uterine fibroids: early results. AJR Am J Roentgenol 2004;183(6):1713-1719.

155. Hynynen K, Chung A, Fjield T, Buchanan M, Daum D, Colucci V, Lopath P, Jolesz F. Feasibility of using ultrasound phased arrays for MRI monitored noninvasive surgery. IEEE Trans Ultrason Ferroelectr Freq Control 1996;43(6):1043-1053.

156. Mougenot C, Köhler MO, Enholm J, Quesson B, Partanen A, Moonen C, Ehnholm G. MR monitoring of the near field HIFU heating. Proc ISTU 2008.

157. Mougenot C, Köhler MO, Quesson B, Partanen A, Enholm J, Moonen C, Vaara T, Ehnholm G. MRI thermometry of near field cumulative heating after successive volumetric HIFU Ablation. ISMRM, 17th Annual Meeting 2009;2515.

158. Mattingly M, Roemer RB, Devasia S. Exact temperature tracking for hyperthermia: A model-based approach. IEEE Trans Control Syst Technol 2000;8(6):979-992.

159. Quesson B, Vimeux F, Salomir R, de Zwart JA, Moonen CT. Automatic control of hyperthermic therapy based on real-time Fourier analysis of MR temperature maps. Magn Reson Med 2002;47(6):1065-1072.

160. Smith NB, Merrilees NK, Dahleh M, Hynynen K. Control system for an MRI compatible intracavitary ultrasound array for thermal treatment of prostate disease. Int J Hyperthermia 2001;17(3):271-282.

161. VanBaren P, Ebbini ES. Multipoint temperature control during hyperthermia treatments: theory and simulation. IEEE Trans Biomed Eng 1995;42(8):818-827.

162. Vanne A, Hynynen K. MRI feedback temperature control for focused ultrasound surgery. Phys Med Biol 2003;48(1):31-43.

163. Mougenot C, Salomir R, Palussiere J, Grenier N, Moonen CT. Automatic spatial and temporal temperature control for MR-guided focused ultrasound using fast 3D MR thermometry and multispiral trajectory of the focal point. Magn Reson Med 2004;52(5):1005-1015.

164. Mougenot C, Quesson B, Denis de Senneville B, Lourenço de Oliveira P, Sprinkhuizen S, Palussiere J, Grenier N, Moonen CT. Three-dimensional spatial and temporal temperature control with MR thermometry-guided focused ultrasound (MRgHIFU). Magn Reson Med 2009;61(3):603-614.

165. Malinen M, Huttunen T, Kaipio JP. An optimal control approach for ultrasound induced heating. Int J Control 2003;76:1323-1336.

166. Chopra R, Burtnyk M, Haider MA, Bronskill MJ. Method for MRI-guided conformal thermal therapy of prostate with planar transurethral ultrasound heating applicators. Phys Med Biol 2005;50(21):4957-4975.

167. Moonen CT. Spatio-temporal control of gene expression and cancer treatment using magnetic resonance imaging-guided focused ultrasound. Clin Cancer Res 2007;13(12):3482-3489.

168. Rahim A, Taylor SL, Bush NL, Ter Haar GR, Bamber JC, Porter CD. Physical parameters affecting ultrasound/microbubble-mediated gene delivery efficiency *in vitro*. Ultrasound Med Biol 2006;32(8):1269-1279.

169. Arora D, Cooley D, Perry T, Skliar M, Roemer RB. Direct thermal dose control of constrained focused ultrasound treatments: phantom and *in vivo* evaluation. Phys Med Biol 2005;50(8):1919-1935.

170. Arora D, Skliar M, Roemer RB. Minimum-time thermal dose control of thermal therapies. IEEE Trans Biomed Eng 2005;52(2):191-200.

171. Arora D, Minor MA, Skliar M, Roemer RB. Control of thermal therapies with moving power deposition field. Phys Med Biol 2006;51(5):1201-1219.

172. Malinen M, Huttunen T, Kaipio JP. Thermal dose optimization method for ultrasound surgery. Phys Med Biol 2003;48(6):745-762.

173. Malinen M, Huttunen T, Hynynen K, Kaipio JP. Simulation study for thermal dose optimization in ultrasound surgery of the breast. Med Phys 2004;31(5):1296-1307.

174. Hey S, Denis de Senneville B, Maclair G, Köhler MO, Quesson B, Ries M. Optimization of volumetric MR-guided high-intensity focused ultrasound ablations in moving organs. ISMRM, 17th Annual Meeting 2009;3294.

175. Jacobs MA, Herskovits EH, Kim HS. Uterine fibroids: diffusion-weighted MR imaging for monitoring therapy with focused ultrasound surgery--preliminary study. Radiology 2005;236(1):196-203.

176. Khiat A, Gianfelice D, Amara M, Boulanger Y. Influence of post-treatment delay on the evaluation of the response to focused ultrasound surgery of breast cancer by dynamic contrast enhanced MRI. Br J Radiol 2006;79(940):308-314.

177. Rouviere O, Lyonnet D, Raudrant A, Colin-Pangaud C, Chapelon JY, Bouvier R, Dubernard JM, Gelet A. MRI appearance of prostate following transrectal HIFU ablation of localized cancer. Eur Urol 2001;40(3):265-274.

178. Wansapura JP, Daniel BL, Pauly J, Butts K. Temperature mapping of frozen tissue using eddy current compensated half excitation RF pulses. Magn Reson Med 2001;46(5):985-992.

179. Puls R, Langner S, Rosenberg C, Hegenscheid K, Kuehn JP, Noeckler K, Hosten N. Laser ablation of liver metastases from colorectal cancer with MR thermometry: 5-year survival. J Vasc Interv Radiol 2009;20(2):225-234.

180. Botnar RM, Steiner P, Dubno B, Erhart P, von Schulthess GK, Debatin JF. Temperature quantification using the proton frequency shift technique: *In vitro* and *in vivo* validation in an open 0.5 tesla interventional MR scanner during RF ablation. J Magn Reson Imaging 2001;13(3):437-444.

181. Zhang Q, Chung YC, Lewin JS, Duerk JL. A method for simultaneous RF ablation and MRI. J Magn Reson Imaging 1998;8(1):110-114.

182. Parker DL, Smith V, Sheldon P, Crooks LE, Fussell L. Temperature distribution measurements in two-dimensional NMR imaging. Med Phys 1983;10(3):321-325.

183. Bloembergen N, Purcell EM, Pound RV. Relaxation effects in nuclear magnetic resonance absorption. Phys Rev 1948;73(7):679-712.

184. Hindman JC. Proton resonance shift of water in gas and liquid states. J Chem Phys 1966;44:4582-4592.

185. Simpson JH, Carr HY. Diffusion and nuclear spin relaxation in water. Phys Rev 1958;111(5):1201-1202.

186. Le Bihan D, Delannoy J, Levin RL. Temperature mapping with MR imaging of molecular diffusion: application to hyperthermia. Radiology 1989;171(3):853-857.

187. Quesson B, de Zwart JA, Moonen CT. Magnetic resonance temperature imaging for guidance of thermotherapy. J Magn Reson Imaging 2000;12(4):525-533.

188. Denis de Senneville B, Quesson B, Moonen CT. Magnetic resonance temperature imaging. Int J Hyperthermia 2005;21(6):515-531.

189. Rieke V, Butts Pauly K. MR thermometry. J Magn Reson Imaging 2008;27(2):376-390.

190. Nemethy G, Scheraga HA. Structure of water and hydorphobic bonding in proteins. 1. A model for thermodynamic properties of liquid water. J Chem Phys 1962;36:3382-3392.

191. Schneider WG, Bernstein HJ, Pople JA. Proton magnetic resonance chemical shift of free (gaseous) and associated (liquid) hybride molecules. J Chem Phys 1958;28:601-607.

192. Bloch F, Hansen WW, Packard M. Nuclear induction. Phys Rev 1946;69:127.

193. Purcell EM, Torrey HC, Pound RV. Resonance absorption by nuclear magnetic moments in a solid. Phys Rev 1946;69:37-38.

194. de Zwart JA, Vimeux FC, Delalande C, Canioni P, Moonen CT. Fast lipid-suppressed MR temperature mapping with echo-shifted gradient-echo imaging and spectral-spatial excitation. Magn Reson Med 1999;42(1):53-59.

195. Peters RD, Hinks RS, Henkelman RM. *Ex vivo* tissue-type independence in proton-resonance frequency shift MR thermometry. Magn Reson Med 1998;40(3):454-459.

196. McDannold N. Quantitative MRI-based temperature mapping based on the proton resonant frequency shift: review of validation studies. Int J Hyperthermia 2005;21(6):533-546.

197. De Poorter J. Noninvasive MRI thermometry with the proton resonance frequency method: study of susceptibility effects. Magn Reson Med 1995;34(3):359-367.

198. Delfaut EM, Beltran J, Johnson G, Rousseau J, Marchandise X, Cotten A. Fat suppression in MR imaging: techniques and pitfalls. Radiographics 1999;19(2):373-382.

199. Meyer CH, Pauly JM, Macovski A, Nishimura DG. Simultaneous spatial and spectral selective excitation. Magn Reson Med 1990;15(2):287-304.

200. Schick F, Forster J, Machann J, Huppert P, Claussen CD. Highly selective water and fat imaging applying multislice sequences without sensitivity to B1 field inhomogeneities. Magn Reson Med 1997;38(2):269-274.

201. Peters RD, Hinks RS, Henkelman RM. Heat-source orientation and geometry dependence in proton-resonance frequency shift magnetic resonance thermometry. Magn Reson Med 1999;41(5):909-918.

202. Schenck JF. The role of magnetic susceptibility in magnetic resonance imaging: MRI magnetic compatibility of the first and second kinds. Med Phys 1996;23(6):815-850.

203. De Poorter J, De Wagter C, De Deene Y, Thomsen C, Stahlberg F, Achten E. Noninvasive MRI thermometry with the proton resonance frequency (PRF) method: *in vivo* results in human muscle. Magn Reson Med 1995;33(1):74-81.

204. El-Sharkawy AM, Schar M, Bottomley PA, Atalar E. Monitoring and correcting spatio-temporal variations of the MR scanner's static magnetic field. MAGMA 2006;19(5):223-236.

205. Rieke V, Vigen KK, Sommer G, Daniel BL, Pauly JM, Butts K. Referenceless PRF shift thermometry. Magn Reson Med 2004;51(6):1223-1231.

206. Kuroda K, Kokuryo D, Kumamoto E, Suzuki K, Matsuoka Y, Keserci B. Optimization of self-reference thermometry using complex field estimation. Magn Reson Med 2006;56(4):835-843.

207. Denis de Senneville B, Desbarats P, Quesson B, Moonen CTW. Real-time artefact corrections for quantitative MR temperature mapping. Journal of WSCG 2003;11:87-94.

208. Lepetit-Coiffé M, Quesson B, Seror O, Dumont E, Le Bail B, Moonen CT, Trillaud H. Real-time monitoring of radiofrequency ablation of rabbit liver by respiratory-gated quantitative temperature MRI. J Magn Reson Imaging 2006;24(1):152-159.

209. Shmatukha AV, Bakker CJ. Correction of proton resonance frequency shift temperature maps for magnetic field disturbances caused by breathing. Phys Med Biol 2006;51(18):4689-4705.

210. Stafford RJ, Price RE, Diederich CJ, Kangasniemi M, Olsson LE, Hazle JD. Interleaved echo-planar imaging for fast multiplanar magnetic resonance temperature imaging of ultrasound thermal ablation therapy. J Magn Reson Imaging 2004;20(4):706-714.

211. Pruessmann KP, Weiger M, Scheidegger MB, Boesiger P. SENSE: sensitivity encoding for fast MRI. Magn Reson Med 1999;42(5):952-962.

212. Weidensteiner C, Kerioui N, Quesson B, Denis de Senneville B, Trillaud H, Moonen CT. Stability of real-time MR temperature mapping in healthy and diseased human liver. J Magn Reson Imaging 2004;19(4):438-446.

213. Kellman P, Epstein FH, McVeigh ER. Adaptive sensitivity encoding incorporating temporal filtering (TSENSE). Magn Reson Med 2001;45(5):846-852.

214. Roujol S, Denis de Senneville B, Vahala E, Sørensen TS, Moonen C, Ries M. Online real-time reconstruction of adaptive TSENSE with commodity CPU / GPU hardware. ISMRM, 17th Annual Meeting 2009;2839.

215. Zeng H, Constable RT. Image distortion correction in EPI: comparison of field mapping with point spread function mapping. Magn Reson Med 2002;48(1):137-146.

216. Dragonu I, Denis de Senneville B, Quesson B, Moonen C, Ries M. Real-time geometric distortion correction for interventional imaging with echo-planar imaging (EPI). Magn Reson Med 2009;61(4):994-1000.

217. Denis de Senneville B, Quesson B, Desbarats P, Mougenot C, Moonen C. Image processing for on-line reduction of thermometry artifacts. ISMRM, 14th Annual Meeting 2006;1425.

218. Maclair G, Denis de Senneville B, Ries M, Quesson B, Desbarats P, Benois-Pineau J, Moonen CT. PCA-based magnetic field modeling: application for on-line MR temperature monitoring. Med Image Comput Comput Assist Interv Int Conf Med Image Comput Comput Assist Interv 2007;10(Pt 2):411-419.

219. Barron JL, Fleet DJ, Beauchemin SS. Performance of optical flow techniques. Int J Comput Vis 1994;12(1):43-77.

220. Cornelius N, Kanade T. Adapting optical-flow to measure object motion in reflectance and x-ray image sequences. ACM SIGGRAPH/SIGART Interdisciplinary Workshop on motion: representation and perception 1983;50-58.

221. Runge VM, Clanton JA, Partain CL, James AE, Jr. Respiratory gating in magnetic resonance imaging at 0.5 Tesla. Radiology 1984;151(2):521-523.

222. Morikawa S, Inubushi T, Kurumi Y, Naka S, Sato K, Demura K, Tani T, Haque HA. Feasibility of respiratory triggering for MR-guided microwave ablation of liver tumors under general anesthesia. Cardiovasc Intervent Radiol 2004;27(4):370-373.

223. Seror O, Lepetit-Coiffé M, Le Bail B, Denis de Senneville B, Trillaud H, Moonen C, Quesson B. Real time monitoring of radiofrequency ablation based on MR thermometry and thermal dose in the pig liver *in vivo*. Eur Radiol 2008;18(2):408-416.

224. Pernot M, Tanter M, Fink M. 3-D real-time motion correction in high-intensity focused ultrasound therapy. Ultrasound Med Biol 2004;30(9):1239-1249.

225. Ehman RL, Felmlee JP. Adaptive technique for high-definition MR imaging of moving structures. Radiology 1989;173(1):255-263.

226. de Zwart JA, Vimeux FC, Palussiere J, Salomir R, Quesson B, Delalande C, Moonen CT. On-line correction and visualization of motion during MRI-controlled hyperthermia. Magn Reson Med 2001;45(1):128-137.

227. Felmlee JP, Ehman RL, Riederer SJ, Korin HW. Adaptive motion compensation in MR imaging without use of navigator echoes. Radiology 1991;179(1):139-142.

228. Wang Y, Grimm RC, Felmlee JP, Riederer SJ, Ehman RL. Algorithms for extracting motion information from navigator echoes. Magn Reson Med 1996;36(1):117-123.

229. Hinks RS. Monitored echo gating (MEGA) for the reduction of data errors and images artifacts. SMR, 7th Annual Meeting 1988;2:744.

230. Pauly J, Nishimura DG, Macovski A. A k-space analysis of small-tip-angle excitation. J Magn Reson 1989;81:43-56.

231. Pauly J., Nishimura D, Macovski A. A linear class of large tip-angle selective excitation pulses. J Magn Reson 1989;82:571-587.

232. Hardy CJ, Pearlman JD, Moore JR, Roemer PB, Cline HE. Rapid NMR cardiography with a half-echo M-mode method. J Comput Assist Tomogr 1991;15(5):868-874.

233. Nehrke K, Börnert P, Groen J, Smink J, Böck JC. On the performance and accuracy of 2D navigator pulses. Magn Reson Imaging 1999;17(8):1173-1181.

234. Hore PJ. Solvent suppression in Fourier transform nuclear magnetic resonance. J Magn Reson 1983;55(2):283-301.

235. Spincemaille P, Nguyen TD, Prince MR, Wang Y. Kalman filtering for real-time navigator processing. Magn Reson Med 2008;60(1):158-168.

236. Bolan PJ, Henry PG, Baker EH, Meisamy S, Garwood M. Measurement and correction of respiration-induced B_0 variations in breast 1H MRS at 4 Tesla. Magn Reson Med 2004;52(6):1239-1245.

237. Peters NH, Bartels LW, Sprinkhuizen SM, Vincken KL, Bakker CJ. Do respiration and cardiac motion induce magnetic field fluctuations in the breast and are there implications for MR thermometry? J Magn Reson Imaging 2009;29(3):731-735.

238. Salomir R, Denis de Senneville B, Moonen CTW. A fast calculation method for magnetic field inhomogeneity due to an arbitrary distribution of bulk susceptibility. Concepts in Magnetic Resonance Part B (Magnetic Resonance Engineering) 2003;19B(1):26-34.

239. Sprinkhuizen SM, Peters NH, Vinken KL, Bakker CJ, Bartels LW. Quantification and correction of motion-induced field disturbances for accurate PRFS-based MR thermometry. 6th interv MRI symp 2006;113-116.

240. Seppenwoolde Y, Shirato H, Kitamura K, Shimizu S, van HM, Lebesque JV, Miyasaka K. Precise and real-time measurement of 3D tumor motion in lung due to breathing and heartbeat, measured during radiotherapy. Int J Radiat Oncol Biol Phys 2002;53(4):822-834.

241. Cartaret T, Merle M, Maclair G, Denis de Senneville B, Moonen C, Quesson B. A rapid and robust method for reducing out-of-plane motion in dynamic imaging. Application to MRI thermometry on abdominal organs. ISMRM, 17th Annual Meeting 2009;2536.

242. Denis de Senneville B, Desbarats P, Quesson B, Moonen CTW. 3D motion estimation for on-line MR temperature mapping. IEEE International Conference on Image Processing (ICIP) 2005;3:101-104.

243. Ries M, Denis de Senneville B, Maclair G, Köhler MO, Quesson B, Moonen C. Three dimensional motion compensation for real-time MRI guided focused ultrasound treatment of abdominal organs. ISMRM, 17th Annual Meeting 2009;442.

244. Damianou C. MRI monitoring of the effect of tissue interfaces in the penetration of high intensity focused ultrasound in kidney *in vivo*. Ultrasound Med Biol 2004;30(9):1209-1215.

245. Hynynen K. Hot spots created at skin-air interfaces during ultrasound hyperthermia. Int J Hyperthermia 1990;6(6):1005-1012.

246. Graham SJ, Bronskill MJ, Henkelman RM. Time and temperature dependence of MR parameters during thermal coagulation of *ex vivo* rabbit muscle. Magn Reson Med 1998;39(2):198-203.

247. Wu T, Felmlee JP, Greenleaf JF, Riederer SJ, Ehman RL. Assessment of thermal tissue ablation with MR elastography. Magn Reson Med 2001;45(1):80-87.

248. Le Y, Glaser K, Rouviere O, Ehman R, Felmlee JP. Feasibility of simultaneous temperature and tissue stiffness detection by MRE. Magn Reson Med 2006;55(3):700-705.

249. Rowland IJ, Rivens I, Chen L, Lebozer CH, Collins DJ, Ter Haar GR, Leach MO. MRI study of hepatic tumours following high intensity focused ultrasound surgery. Br J Radiol 1997;70:144-153.

250. McDannold N, Moss M, Killiany R, Rosene DL, King RL, Jolesz FA, Hynynen K. MRI-guided focused ultrasound surgery in the brain: tests in a primate model. Magn Reson Med 2003;49(6):1188-1191.

251. Chen L, Bouley DM, Harris BT, Butts K. MRI study of immediate cell viability in focused ultrasound lesions in the rabbit brain. J Magn Reson Imaging 2001;13(1):23-30.

252. Noterdaeme O, Leslie TA, Kennedy JE, Phillips RR, Brady M. The use of time to maximum enhancement to indicate areas of ablation following the treatment of liver tumours with high-intensity focused ultrasound. Br J Radiol 2009;82(977):412-420.

253. Bremer C, Bankert J, Filler T, Ebert W, Tombach B, Reimer P. High-dose Gd-DTPA vs. Bis-Gd-mesoporphyrin for monitoring laser-induced tissue necrosis. J Magn Reson Imaging 2005;21(6):801-808.

254. Fennessy FM, Tempany CM. MRI-guided focused ultrasound surgery of uterine leiomyomas. Acad Radiol 2005;12(9):1158-1166.

255. Gianfelice D, Khiat A, Amara M, Belblidia A, Boulanger Y. MR imaging-guided focused ultrasound surgery of breast cancer: correlation of dynamic contrast-enhanced MRI with histopathologic findings. Breast Cancer Res Treat 2003;82(2):93-101.

256. Chen J, Daniel BL, Diederich CJ, Bouley DM, van den Bosch MA, Kinsey AM, Sommer G, Pauly KB. Monitoring prostate thermal therapy with diffusion-weighted MRI. Magn Reson Med 2008;59(6):1365-1372.

257. Cacheris WP, Quay SC, Rocklage SM. The relationship between thermodynamics and the toxicity of gadolinium complexes. Magn Reson Imaging 1990;8(4):467-481.

258. McDannold N, Tempany CM, Fennessy FM, So MJ, Rybicki FJ, Stewart EA, Jolesz FA, Hynynen K. Uterine leiomyomas: MR imaging-based thermometry and thermal dosimetry during focused ultrasound thermal ablation. Radiology 2006;240(1):263-272.

259. Pilatou MC, Stewart EA, Maier SE, Fennessy FM, Hynynen K, Tempany CM, McDannold N. MRI-based thermal dosimetry and diffusion-weighted imaging of MRI-guided focused ultrasound thermal ablation of uterine fibroids. J Magn Reson Imaging 2009;29(2):404-411.

260. Delon-Martin C, Vogt C, Chignier E, Guers C, Chapelon JY, Cathignol D. Venous thrombosis generation by means of high-intensity focused ultrasound. Ultrasound Med Biol 1995;21(1):113-119.

261. Hynynen K, Colucci V, Chung A, Jolesz F. Noninvasive arterial occlusion using MRI-guided focused ultrasound. Ultrasound Med Biol 1996;22(8):1071-1077.

262. Ichihara M, Sasaki K, Umemura S, Kushima M, Okai T. Blood flow occlusion via ultrasound image-guided high-intensity focused ultrasound and its effect on tissue perfusion. Ultrasound Med Biol 2007;33(3):452-459.

263. Jacobs MA, Ouwerkerk R, Kamel I, Bottomley PA, Bluemke DA, Kim HS. Proton, diffusion-weighted imaging, and sodium (23Na) MRI of uterine leiomyomata after MR-guided high-intensity focused ultrasound: a preliminary study. J Magn Reson Imaging 2009;29(3):649-656.

264. Souchon R, Rouviere O, Gelet A, Detti V, Srinivasan S, Ophir J, Chapelon JY. Visualisation of HIFU lesions using elastography of the human prostate *in vivo*: preliminary results. Ultrasound Med Biol 2003;29(7):1007-1015.

265. Wu T, Felmlee JP, Greenleaf JF, Riederer SJ, Ehman RL. MR imaging of shear waves generated by focused ultrasound. Magn Reson Med 2000;43(1):111-115.

ISBN 978-952-248-198-6
ISBN 978-952-248-199-3 (PDF)
ISSN 1795-2239
ISSN 1795-4584 (PDF)